From Semiconductor Lasers to Fiber Bragg Grating Lasers in Optical Communications

Thesis by

Dan R. Provenzano

In Partial Fulfillment of the Requirements

For the Degree of

Doctor of Philosophy

California Institute of Technology

Pasadena, California

2001

(Defended December 18, 2000)

For my parents

Acknowledgments

I would first like to thank Professor Amnon Yariv for accepting me as a member of his research group. Through his influence and expertise, I have learned so much in the way of professional scientific research and gained a more physical intuition of light. The academic and research environment he creates through his leadership and experience has made my years here challenging and rewarding.

I owe many thanks to Professor Yaakov Shevy, whom I have been fortunate to work closely with for the past year. He has been a great help in guiding the direction of my research, as well as a source of motivation and inspiration. I thank the many members of the research group whom I have had the pleasure to interact with and learn from. These people have become my good friends: Dr. Boaz Salik, Dr. Roger G. M. P. Koumans, Dr. Matt McAdams, Dr. Reginald Lee, Dr. John Kitching, Dr. Bill Marshall, Dr. Doruk Engin, Kartik Srinivasen, and George Paloczi. I thank the many other group members whom I have enjoyed working with, namely, Dr. Kiril Scheglov, Dr. John Iannelli, Dr. Eva Peral, Dr. David Geraghty, Ashish Bhardwaj, Yi Li, Dr. Avishay Eyal, William Green, and John Choi.

Professor Vahala has been a great help in guiding me through the early stages of the fiber Bragg grating project and has been an excellent teacher of difficult topics. The Caltech staff members, Ali Ghaffari, Jana Mercado, Connie Rodriguez, and Larry Begay, have provided immeasurable support.

I thank my collaborators at Ortel Corporation, namely T.R. Chen, who has provided lasers for study and use. Financial support for this research was provided by the National Science Foundation, the Defense Advanced Research Projects Agency, the Office of Naval Research, and the Air Force Office of Scientific Research. The opportunity for advancing the knowledge base and technology of mankind is greatly appreciated and not taken for granted.

Finally, and most importantly, I thank my family. Mom, Dad, and Pro, and all four of my grandparents, the lessons about life that you have taught me form my most cherished wisdom. Your love and support in all situations have made this possible. To my sweetheart, Traci, thank you for your acceptance of all my eccentricities and for keeping my spirits high. I want you always by my side.

Abstract

This thesis describes the semiconductor laser signal and noise propagation effects in single mode fiber and fiber Bragg gratings. The capability to fabricate custom fiber Bragg gratings was developed, which enabled the design and fabrication of gratings for a number of applications. Finally, gratings were developed and specialized for use in a single mode fiber ring laser.

A quantum mechanical description of laser noise is presented in order to discuss pump-noise suppressed semiconductor lasers capable of sub-shot noise, also known as "squeezing." Experimental results for an 850 nm Fabry-Perot semiconductor laser are presented showing squeezing at room temperature of 29% below the shot noise limit measured using a balanced homodyne detector, corresponding to 41% below the standard quantum limit at the output facet of the laser. The side mode suppression ratio was varied with slight temperature tunings and correlated with the laser noise. It was found that the higher the sidemode suppression ratio, the lower the noise.

Noise analysis was continued with 1540 nm distributed feedback semiconductor lasers. Laser parameters such as noise, chirp, and resonance frequency were characterized by propagation in dispersive fiber and fitting the parameters to a model for the fiber. Again, a correlation was found between side mode suppression and laser noise, especially after several kilometers of propagation in fiber. The principles of signal and noise propagation were applied to fiber Bragg gratings. Theory and experiment indicated direct

laser modulation enhancement by a uniform fiber Bragg grating by 7 dB at modulation frequencies of up to 25 GHz, and also noise reduction of 2 dB at frequencies up to 15 GHz.

Facilities were established to write and produce customized fiber Bragg gratings of various strengths in various fiber types as well as in ion-exchanged waveguides in bulk glasses. Analyses of writing times and strengths were performed and optimized for various applications. Uses for these gratings include dispersion compensation, noise reduction, beam or pulse shaping, and spectral filtering for dense wavelength division multiplexed (DWDM) optical networks. Amplitude and phase masks were developed and shown to produce arbitrarily apodized and chirped gratings.

Fiber gratings were next refined for use as key elements in a new type of single mode fiber ring laser. Some of the beneficial characteristics of this fiber laser include long cavity size (80 cm), 80 dB signal-to-noise ratio, high side mode suppression ratio, and white noise linewidth as narrow as 2 kHz. The laser noise was also nearly shot noise limited. This combination of low amplitude and low phase noise allowed the observation of extremely low noise enhancement after 50 km of standard, dispersive fiber up to 20 GHz frequency. A comparison was made between our fiber ring laser and a standard high grade distributed feedback semiconductor laser in transmitting 10 Gbits/sec data. Over a 50 km fiber, the fiber ring laser achieved the same signal to noise ratio with half the power as the semiconductor laser.

Table of Contents

List of Figures

Chapter 1 - Introduction to the Thesis

1.1. Introduction

This thesis describes research done for the degree of Doctor of Philosophy in Applied Physics at the California Institute of Technology. Work for this thesis was performed in the field of optical communications, which is the transmission of data via light in optical fiber. This work centers on the analysis and characterization of semiconductor laser sources for fiber optic communication, and culminating in the invention of a new type of fiber ring laser. It is shown that the properties of this ring laser have great potential as optical fiber communication sources for Dense Wavelength Division Multiplexing (DWDM) networks. The fabrication and testing of these lasers involved writing our own custom Fiber Bragg Gratings (FBG) in various fiber types. Furthermore, with the capability of fabricating custom gratings, new types of FBG based devices for certain applications were modeled, and fabricated, and tested.

This thesis was motivated by the technological demands to better understand the propagation of optical signals in fiber, the lasers which generate the light, and then to locate and make innovations to improve the speed and efficiency at which data can be

sent over fiber. The uses of fiber systems have now spread into nearly all areas of city-to-city data transfer, such as telephone, cable television, and internet data.

1.2. Optical Communication Systems

Data rates of 10 Gbits/sec are now common in fiber systems. Direct modulation of semiconductor lasers has reached a limit due to the limits in response times of the laser to modulation as well as physical limits of coupling high frequency signals to the laser chip. The common, although expensive, method for 10 Gbit/sec data networks is external modulation of the laser light by electro-optic modulators. Figure 1.1 shows a typical fiber link.

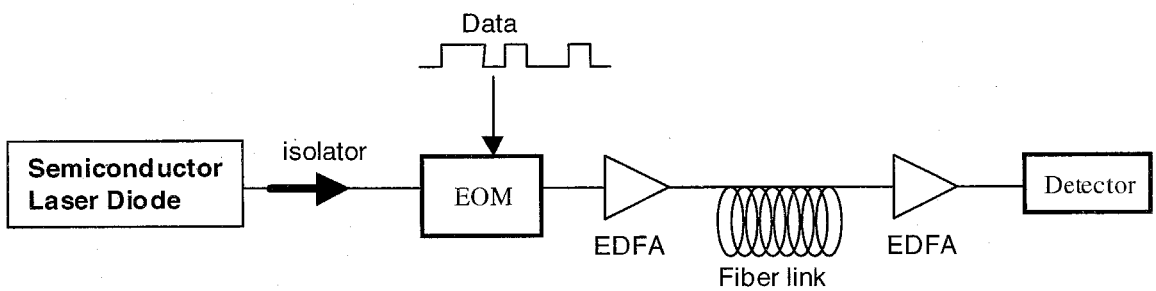

Figure 1.1. Schematic of fiber optic communication system.

Data is added to the optical signal by an electro-optic modulator (EOM), a crystal device which has an index of refraction modulated by the data signal. This index modulation is converted from a phase modulation to amplitude modulation in a Mach-Zehnder

interferometer geometry. Erbium doped fiber amplifiers (EDFA) amplify the light before and after long fiber sections.

Single-mode fiber is the most advanced medium for a linked communication system. The vast majority of the fiber in use today was originally designed for 1310 nm window, but the advent of EDFA's shifted the bandwidth of choice to the 1540 nm low-loss window of silica. At this wavelength there is 17 ps/(nm·km) of dispersion and causes distortion of both the signal and noise, known as FM-to-AM conversion. Characterizing and understanding signal and noise propagation in fibers is crucial to designing optimized network components and laser sources.

1.3. Outline of this Thesis

This thesis consists of the work done in several projects relating to the analysis of signals and noise and in the field of optical communications. In Chapter 2, the theory of quantum noise of a semiconductor laser is reviewed. Experimental measurements with a Fabry-Perot semiconductor laser from SDL Inc. shows the quantum noise is actually below the shot noise limit at 28 MHz for certain temperature tunings. Very good sidemode suppression is shown to contribute to this reduction.

Chapter 3 moves the semiconductor analysis to the distributed feedback (DFB) laser structures operating at 1540 nm. We develop the theory of the dynamics of

semiconductor lasers. Laser parameters such as relaxation constants and the linewidth enhancement factor are obtained from fiber propagation experiments.

Chapter 4 begins with the theory of fiber Bragg grating (FBG) technology and fabrication techniques used for the remainder of the thesis is discussed. Numerical simulations quite accurately predict the types of structures fabricated in the lab and account well for prescribed apodization, chirp, and absorption.

Chapter 5 discusses several applications of fiber Bragg gratings which were analyzed and constructed for this thesis. They include signal modulation enhancement, noise reduction, mode conversion in 3-mode fiber, and fiber FBG Fabry-Perot cavity, both with and without gain.

Chapter 6 is the climax of the FBG fabrication project. We have constructed a single mode fiber ring laser which is based on fiber Bragg gratings. The advantages of a ring configuration as compared to linear laser geometry are outlined. Characteristics of output power, sidemode power, noise, and linewidth are modeled, measured, and compared to these characteristics of a communications grade DFB semiconductor laser. Bit error rate measurements were also performed with various lengths of fiber and compared to the DFB semiconductor laser. Finally, the role of this fiber ring laser in digital networks is discussed and analyzed by bit error rate measurements.

Chapter 2 - Amplitude Squeezing in Semiconductor Lasers

2.1. Introduction

Squeezed states of the electromagnetic field are beginning to create new possibilities for precision measurements near the standard quantum limit. Amplitude squeezed states generated from pump-suppressed semiconductor lasers offer a number of desirable features such as large squeezing bandwidths, ease of implementation, and the fact that the squeezing is superimposed on a large coherent optical field. While measurements of amplitude squeezing performed on lasers cooled to cryogenic temperatures have resulted in substantial amounts of squeezing, the generation of amplitude squeezed light from room temperature devices has been considerably less successful. Several experiments on both room temperature and cryogenically cooled devices [2–1],[2–2],[2–3] have observed excess noise which tends to obscure the squeezing. The difficulty in producing and maintaining large degrees of (both amplitude and quadrature) squeezing has been a major stumbling block in the implementation of these sources in precision measurement systems.

2.2. Theory of Amplitude Squeezing

To properly analyze the low frequency noise spectrum for a semiconductor laser, it is necessary to invoke a quantum mechanical optical field. Low frequencies in this case refer to frequencies well below the cavity relaxation resonance, typically around 1 GHz for a semiconductor laser. In this regime, the gain clamping mechanism is very strong and the noise is very close to the shot noise level (SNL) or even below.

The quantum theory of laser noise used here is based on the quantum Langevin analysis of Yamamoto [2–4]. Figure 2.1 shows a schematic for a laser diode system. A partially reflecting end facet introduces vacuum field fluctuations effects, which much be considered as part of the system.

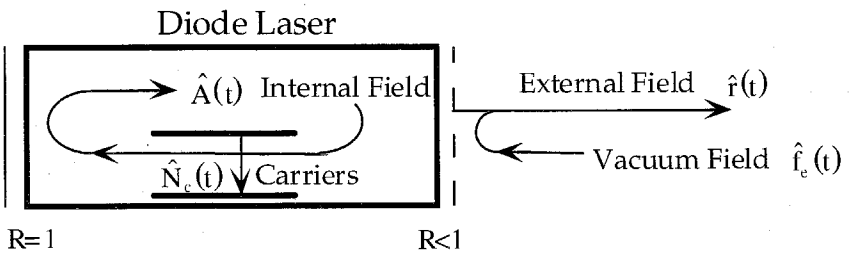

Figure 2.1. Model of laser for quantum mechanical noise model.

An adiabatic elimination of the dipole moment is justified by the fast relaxation time of the dipole, τ_d, relative to the photon lifetime, τ_p, in the cold cavity. The elimination is performed by integrating the rate equations over a time

$$\tau_d << t << \tau_p \tag{2.1}$$

assuming the electric field doesn't change much in time. The resulting equations for the operators for inversion, $\hat{N}(t)$, field annihilation, $\hat{A}(t)$, and external field, $\hat{r}(t)$, are [2–4]

$$\frac{d}{dt}\hat{N}(t) = P - (1-\beta)\frac{\hat{N}(t)}{\tau_{sp}} - \frac{\omega}{\mu^2}\hat{\chi}_i\hat{A}^+\hat{A} - \left\langle \frac{\omega}{\mu^2}\chi_i \right\rangle + \hat{\Gamma}_p(t) + \hat{\Gamma}_{sp}(t) + \hat{\Gamma}(t)$$

$$\frac{d}{dt}\hat{A}(t) = -\frac{1}{2}\left[\frac{1}{\tau_{p0}} + \frac{1}{\tau_{pe}} + 2i(\omega_L - \omega_0) - \frac{\omega}{\mu^2}(\hat{\chi}_i - i\hat{\chi}_r)\right]\hat{A}(t) + \hat{G}(t) + \hat{g}(t) + \sqrt{\frac{1}{\tau_{pe}}}\hat{f}_e(t)$$

$$\hat{r}(t) = -\hat{f}_e(t) + \frac{\hat{A}(t)}{\sqrt{\tau_{pe}}} \tag{2.2}$$

where P is the pump rate, β is the fraction of spontaneous emission emitted into the lasing mode, τ_{sp} is the spontaneous emission lifetime, μ is the nonresonant refractive index, $\hat{X}(N)$ is the resonant optical susceptibility, τ_{p0} and τ_{pe} are cavity photon lifetimes for internal and external mirror losses, respectively, ω is the lasing frequency, and ω_0 is the cold cavity resonance frequency. $\hat{\Gamma}(t)$ and $\hat{G}(t)$ are the Langevin noise sources due to the dipole moment and the others represent noise due to pumping and spontaneous emission. The correlation functions for the Langevin noise sources are covered fully in several places [2–4],[2–5],[2–6]. Solutions to (2.2) are found by assuming small signal variations around a mean:

$$\begin{aligned}
\hat{N}(t) &= N_0 + \Delta\hat{N}(t) \\
\hat{a}(t) &= \left[A_0 + \Delta\hat{A}(t)\right]e^{i\Delta\hat{\phi}(t)} \\
\hat{r}(t) &= \left[r_0 + \Delta\hat{r}(t)\right]e^{i\Delta\hat{\Psi}(t)}
\end{aligned} \tag{2.3}$$

The use of phase operators here is not perfectly rigorous but serves as a correspondence in the situation of a large field and relatively small fluctuations [2–7]. Substituting in these approximations, taking the Fourier transform and solving for $\Delta\hat{r}(\Omega)$ leads to the power spectral density. The result is quite simple in the limit of low frequency, useful for most applications $\frac{\Omega}{2\pi} << \frac{1}{\tau_p} \approx$ few GHz. At exactly $\Omega = 0$, the noise power spectral density, normalized to the shot noise level, is

$$P_{\Delta\hat{A}}(0) = (1-\eta) + \eta\left[\left(1+\frac{1}{R}\right) + \frac{1}{R} + \frac{2}{n_{sp}R^2}\right] \tag{2.4}$$

where η is the differential quantum efficiency, and R is the pumping level above threshold. By pumping with a current source, $R = i/i_{th} - 1$, where i_{th} as the threshold current. The terms on the right are as follows. The first term in parentheses is due to optical losses inside the laser cavity, the other term in parentheses accounts for pump noise, 1/R comes from spontaneous emission into nonlasing modes, and the final term is the contribution from dipole moment fluctuations.

With a constant current source it is possible to have quite near perfect pumping with no introduced noise (pump suppression). This leaves the largest impediment to amplitude squeezing the quantum efficiency η. The next section shows the measurements obtained with free running semiconductor laser.

2.3. Measurements of Amplitude Squeezing

The experimental setup for measuring quantum laser noise is shown in Figure 2.2 [2–8]. The semiconductor laser we used (SDL-5402-H1) was a quantum-well index-guided structure with a threshold current of 10.2 mA and a maximum rated operating current of 63 mA resulting in 51 mW of output power. The external differential quantum efficiency was 68% at room temperature. The device was mounted by the manufacturer inside a TO-3 package which contained a thermistor, thermoelectric (TE) cooler and monitor photodiode. The laser temperature was actively stabilized using a home built temperature controller, and a precision current source provided the injection current which passed through an inductor before going to the laser. While careful control of the laser temperature and injection current was found to be an important factor in producing the squeezing, no other modifications to the device appeared to be necessary.

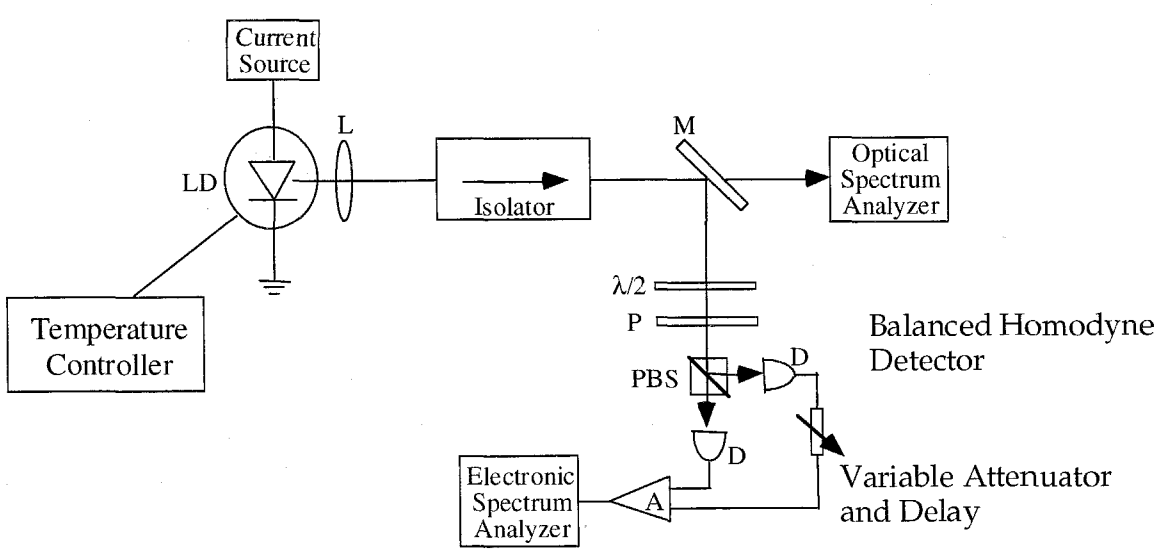

Figure 2.2. Free space setup for measuring laser noise.

LD: laser diode, L: lens, M: mirror, P: polarizer, PBS: polarizing beam splitter, D: detector, A: differential amplifier.

The output light from the laser was collimated using an anti-reflection coated collimating lens before being sent through an optical isolator (providing >60 dB of isolation) to the detection system. The amplitude noise was measured using the balanced receiver. The beams incident on the photodiodes were expanded to fill the entire detector area and the resulting AC photocurrents were amplified and sent to a differential amplifier which could either add or subtract the two signals. The output from the differential amplifier was then sent to an electronic spectrum analyzer for measurement of the noise. One electronic arm of the balanced receiver included an attenuator and a delay unit. Common mode rejection of over 45 dB was obtained at a frequency of 28 MHz.

The balanced homodyne detector works as follows. Consider the laser field as

$$\text{Field: } \dot{E}_f = A + \Delta a$$

$$\text{Vacuum: } E_{vac} = \Delta b \tag{2.5}$$

The input field incident on the beam splitter was adjusted by the polarizer and l/4 plate so that the field incident on each detector is

$$E_{1,2} = \pm\frac{1}{\sqrt{2}}(A + \Delta a - \Delta b) \tag{2.6}$$

The currents, i_1 and i_2, have fluctuations, Δi_1 and Δi_2, neglecting second orders in the Δ's, equal to:

$$\Delta i_{1,2} = \Re A(\Delta a \mp \Delta b) \tag{2.7}$$

where $\Re$ is the detector responsivity.

With the balanced detector system, it is possible to toggle between laser noise and the shot noise value by either adding or subtracting (inverting then adding) the photocurrent signals from the detectors. The detectors are balanced at a certain frequency by adjusting a delay such that the received power is

$$P_{\Delta i_+} = 4A\left\langle (\Delta a)^2 \right\rangle \text{ Laser noise}$$

$$P_{\Delta i_-} = 4A\left\langle (\Delta b)^2 \right\rangle \text{ Shot noise} \tag{2.8}$$

Figure 2.3 shows the measured photocurrent noise power spectrum (trace A) when the photocurrents at 28 MHz were balanced. The electronic delay present in one arm of the receiver causes a frequency-dependent phase shift between the two signals entering the differential amplifier. This results in the output photocurrent noise power varying, as a function of frequency, between the actual laser noise level and the Standard Quantum Limit (SQL) [2–9].

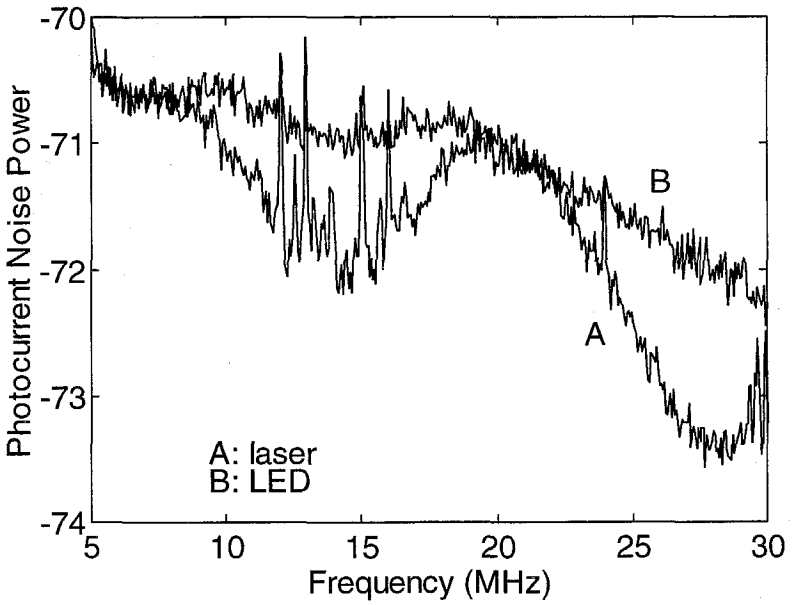

Figure 2.3. Noise power vs. frequency.

The level of the SQL was checked by shining the light from high-power LED's onto the detectors to produce the same photocurrent as the laser. The photocurrent noise power spectrum obtained from the LED's is shown in trace B. It can be seen that at 28 MHz, the laser photocurrent noise power is 1.4 dB below the SQL (determined by the LED) indicating that the laser amplitude fluctuations were squeezed by this amount. For this measurement, the laser injection current was 66 mA, resulting in a photocurrent of 13.4 mA/detector (current-to-current differential efficiency of 48%) and the laser was cooled to about 5°C with the TE cooler. The resolution bandwidth for this measurement was 100 kHz and the background amplifier noise level was subtracted from all measured signals.

As an additional check on the level of squeezing, the amplitude noise was then measured as a function of the optical attenuation, shown in Figure 2.4. For the shot noise limited LED's, the noise exactly followed the measured shot noise (subtracted photocurrents for either the LED or laser), and the laser noise is shown to grow sublinear with respect to DC photocurrent. Normalized to the SQL, the laser noise was found to increase in a linear fashion towards unity as the attenuation was made stronger.

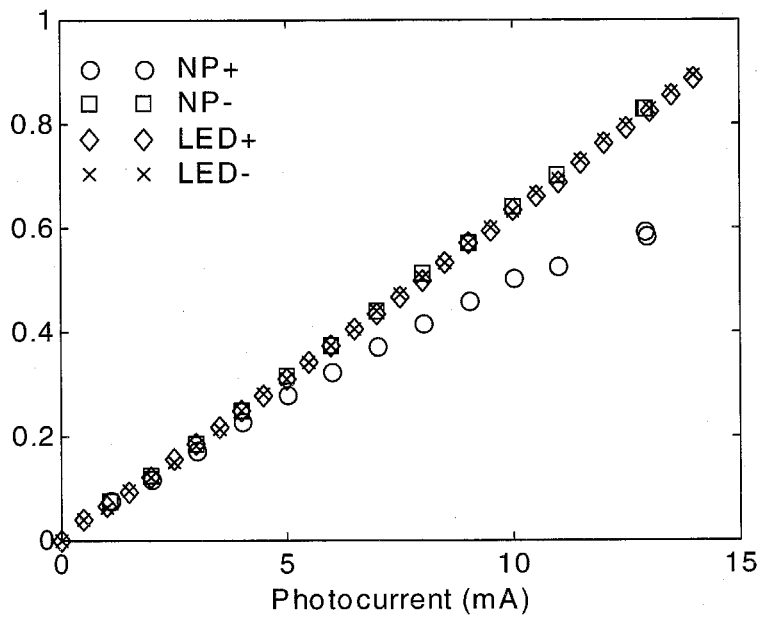

Figure 2.4. Noise power vs. photocurrent.

The squeezing could only be obtained in a narrow range of laser temperatures and injection currents. At most combinations of these two parameters, the laser operated multi-mode and the amplitude noise was far above the SQL. It appeared that particularly good side mode suppression was required in order generate squeezed light from the laser.

The longitudinal mode spectrum was therefore measured simultaneously with the amplitude noise and a typical spectrum, obtained when the amplitude noise was 1.4 dB below the SQL, is shown in Figure 2.5. The resolution of the trace is limited by the bandwidth of the optical spectrum analyzer which "smears" the features of the spectrum; however, the sidemodes are still resolved.

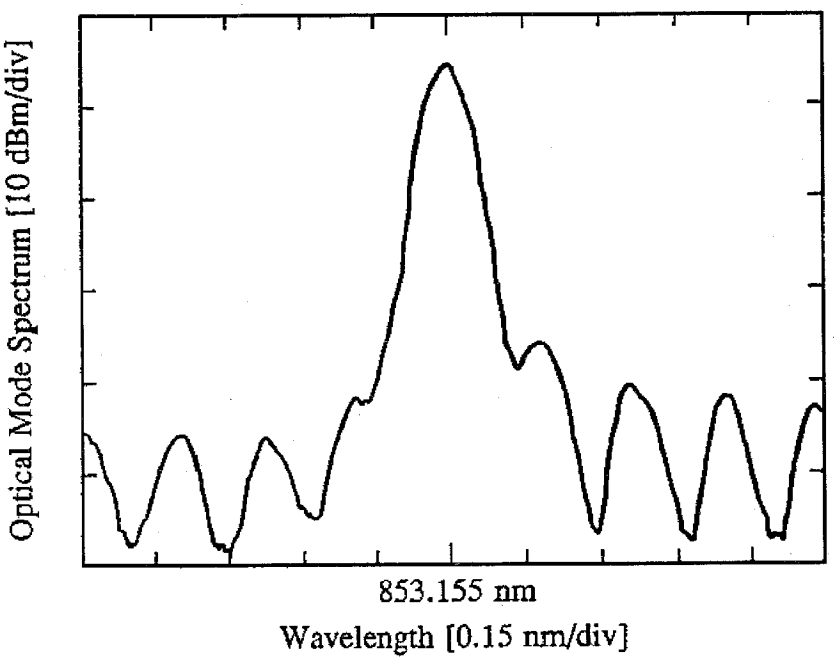

Figure 2.5. Optical spectrum.

The power in the largest side mode was about 30 dB smaller than the main mode power and the power in most of the other side modes was somewhat smaller still. It seems likely that the excellent side mode suppression observed in this laser was the reason the large squeezing measured while other, similar, lasers would not produce significant amplitude squeezing [2–3],[2–10] under comparable operating conditions.

The photocurrent noise at 28 MHz was then measured as a function of the laser injection current. The results, normalized to the SQL, are plotted against the pump rate $R=i/i_{th}-1$ in Figure 2.6.

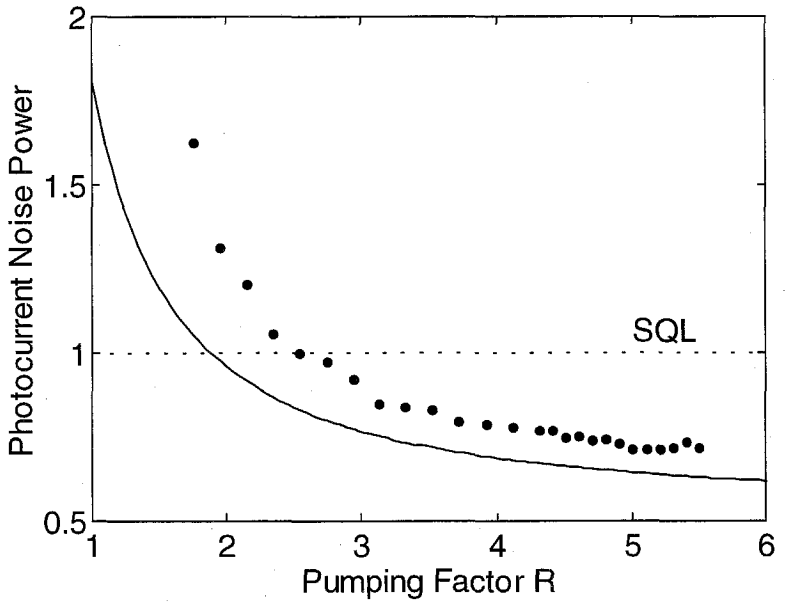

Figure 2.6. NP vs. Pumping.

It can be seen that, starting well above threshold, the noise level increases as the laser approaches threshold, crossing over the SQL at an injection current of about R=2.5. Also shown in the figure is the prediction of the single-mode theory of [2–4] in the low frequency limit with $n_{sp}=1.2$ and with the pump noise assumed to be completely suppressed. Although the general features of the data seem to be in approximate agreement with the theory, there is still a roughly 10-20% discrepancy over the entire

range of injection currents at which the measurements were made. The minimum noise obtained with this laser was 1.5 dB or 29% below the SQL.

If the laser temperature was altered slightly, both the mode spectrum and the amplitude noise were found to change in a correlated way. By far the largest change in the side mode power occurred for the two longitudinal side modes closest to the lasing mode in wavelength. The amplitude noise, normalized to the SQL, is plotted against the fraction of total optical power in these two modes in Figure 2.7.

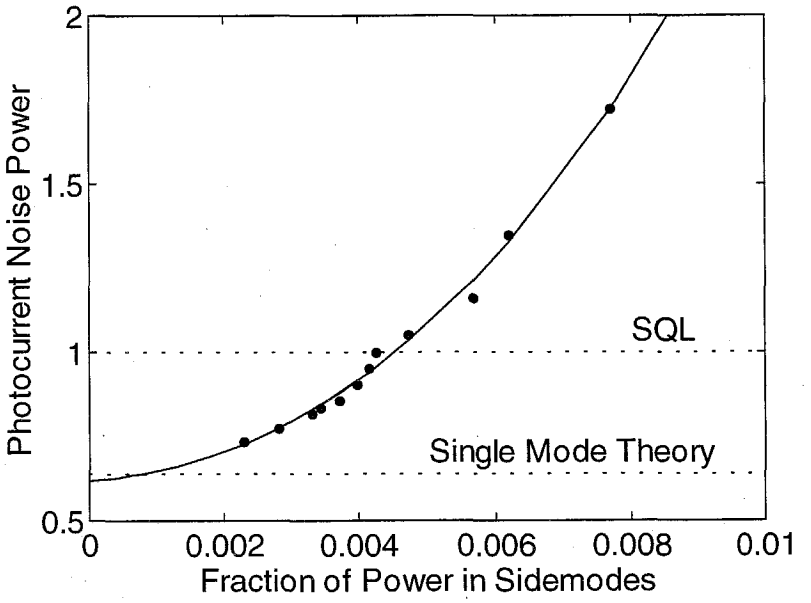

Figure 2.7. NP vs. side mode suppression.

A clear correlation between the side mode power and excess amplitude noise can be seen and the laser noise was found to increase to ten times the SQL when 5% of the optical power was present in the two measured side modes. The data also indicate that,

for this laser, the power in the side modes needed to be less than about 0.5% of the total output power in order for the excess noise to be small enough so that the amplitude squeezing is seen. A third-order polynomial fit to the measured data is also shown (solid line). An extrapolation of this curve to zero side mode power gives excellent agreement with the prediction of the single mode theory (indicated by the dash-dotted line). This suggests that if the excess noise due to the side modes were eliminated, the laser noise would approach the fundamental limit determined, primarily, by the device and detection efficiencies. However, the theory of Yamamoto [2–4] applies only to a laser for which both facet reflectivities are close to unity. This was not the case for the laser used in this experiment which had one facet anti-reflection coated. Recent numerical calculations using traveling-wave models [2–11] have shown that dramatic changes in the theoretically predicted amplitude noise power can occur when the "good-cavity" assumption is relaxed.

The mechanism by which the side modes generate the excess noise is still unclear. However, the second order term in the fit dominates over the range of side mode powers shown indicating that the excess noise is proportional to the square of the side mode power in this range. Attempts to fit the multimode theory described in [2–3] to the data were not particularly successful. At side mode powers above 1% of the total power, the fit in Figure 2.7 no longer agreed well with the measured data. Some recent work with two-mode quantum Langevin equations [2–12] indicate that for the right conditions, the extremely good correlation of mode noise which produce the effect of squeezing can be spoiled by nonlinear gain saturation differences between modes and spectral hole burning.

It is also known that extremely small amounts of optical feedback can significantly effect the amplitude noise of the laser [2–3]. Several checks were therefore performed under conditions of maximum squeezing in order to determine if spurious optical feedback was present and, if so, was influencing the laser noise. First, the laser temperature and injection current were varied by an amount not large enough to cause a significant change in the side mode suppression but large enough to vary the laser frequency by a few GHz. The idea here was that if optical feedback were present with an intensity large enough to change the amplitude noise, then changing the laser frequency would change the phase of the feedback thereby generating oscillations in the amplitude noise. The amplitude noise was found to vary by less than the measurement error of 0.1 dB, however. In addition, the position of the optical isolator was varied over several wavelengths by placing its translation stage on a piezo-electric transducer (PZT), and again no significant change in the amplitude noise was observed. Finally, the position of the collimating lens was also varied over several wavelengths using a PZT and no change in the measured squeezing was observed. The above checks seem to indicate that optical feedback from the tested components was not playing a significant role in reducing the amplitude noise.

In summary, amplitude squeezing 29% below the SQL has been measured from a commercial room-temperature Fabry-Perot semiconductor laser. This corresponds to a noise level 41% below the SQL at the output facet of the laser when correction is made for optical losses present in the detection system. Excess noise, which degrades the squeezing, appears to be associated with the presence of longitudinal side modes. While

the measured amount of squeezing is still 10-20% smaller than predicted by the standard single-mode theory, an extrapolation of the data to zero side-mode power gives agreement with the theory to within ~3%. Careful stabilization of the laser temperature and injection current are important factors in keeping the side mode power to below acceptable levels. However, other than the control of optical feedback from the detection system, no other modifications to the laser appear to be necessary in order to obtain significant amplitude squeezing.

2.4. Discussion

These results demonstrate that substantial squeezing can indeed be obtained from a commercial device operating at room temperature with no external components or modifications other than those used to detect the light. The excess noise which degrades squeezing is also investigated and it appears that the source of most of this noise under a wide range of operating conditions is associated with the presence of weak longitudinal side modes. Our measurements indicate that, under optimal conditions, the amount of squeezing is limited primarily by the device and detection efficiencies, in accordance with the standard single-mode theory of amplitude noise in semiconductor lasers.

Since there appear to be no fundamental reasons why room temperature lasers should exhibit significantly less squeezing than cryogenically cooled devices, there has been some effort recently to determine why the generation of amplitude squeezing at

room temperature has been so difficult. This has been motivated in part by a desire to understand the excess noise sources which occur in semiconductor lasers. Excess noise has made comparisons of experimental data with theory somewhat difficult: It is not altogether clear how the excess noise is generated or what fraction of the total noise it represents. More important, however, is the lure of being able to produce large amounts of squeezing from off-the-shelf commercial devices. Such an accomplishment would be an important step on the road to facilitating precision measurements with sensitivities below the SQL. Several experiments have been performed recently, designed to increase the squeezing from commercial, room temperature lasers using external optical modifications such as injection locking and optical feedback. While these experiments have been, on the whole, successful in reducing the amplitude noise to as much as 50% below the SQL, the added complexity is, in principle, unnecessary.

References for Chapter 2

[2–1] W. H. Richardson and R. M. Shelby, "Nonclassical light from a semiconductor laser operating at 4K," Phys. Rev. Lett. 64 pp. 400-403 (1990).

[2–2] M. J. Freeman, H. Wang, D. G. Steel, R. Craig and D. R. Scifres, "Amplitude squeezed light from quantum-well lasers," Opt. Lett. 18 pp. 379-381 (1993).

[2–3] J. Kitching, A. Yariv, and Y. Shevy, "Room temperature generation of amplitude squeezed light froma semiconductor laser with weak optical feedback." Phys. Rev. Lett. 74, pp. 3372-3375 (1995).

[2–4] Y. Yamamoto, S. Machida, and O. Nilsson, "Amplitude squeezing in a pump-noise-suppressed laser oscillator." Phys. Rev. A. 34 (5) pp. 4025-4042 (1986).

[2–5] M. Sergent III, M. O. Scully, and W. E. Lamb, Jr. *Laser Physics*, Addison-Wesley, Reading, MA (1974).

[2–6] William H. Louisell, *Quantum Statistical Properties of Radiation,* John Wiley and Sons, New York (1973).

[2–7] L. Sussking and J. Glogower, "Quantum mechanical phase and time operator," Physics, 1, pp. 49-61 (1964).

[2–8] J. Kitching, D. Provenzano, and A. Yariv, "Generation of amplitude-squeezed light from a room temperature Fabry-Perot semiconductor laser." Opt. Lett. 20 (24), pp. 2526-2528 (1995).

[2–9] S. Machida and Y. Yamamoto, "Observation of amplitude squeezing from semiconductor laser by balanced detectors with a delay line," Opt. Lett. 14 p. 1045 (1989).

[2–10] M. J. Freeman, D. C. Kilper, D. G. Steel, R. Craig and D. R. Scifres, "Room temperature amplitude-squeezed light from an injection-locked quantum well laser with a time-varying drive current," Opt. Lett. 20 pp. 183-185 (1995).

[2–11] B. Tromborg, H. E. Lassen and H. Olesen, "Travelling wave analysis of semiconductor lasers: modulation responses, mode stability and quantum

mechanical treatment of noise spectra," IEEE J. Quantum Electon. 30 pp. 939-956 (1994).

[2–12] H. Deng and Y. Shevy, "Study of quantum AM noises of semiconductor lasers with optical feedback," unpublished (May 2000).

Chapter 3 - Characterizing Distributed Feedback Semiconductor Lasers

3.1. Introduction

The physics of optical gain in semiconductor lasers in treated in many texts. It is the result of pumping charge carriers to higher energy states to obtain separate quasifermi levels, E_{Fc} and E_{Fv}, for electrons and holes, respectively. Stimulated emission, gain, occurs at frequencies ν such that $h\nu < E_{Fc} - E_{Fv}$.

This chapter explores the properties of the semiconductor lasers used for optical communications for a better understanding and simpler characterization method based on propagation in dispersive fiber. Fiber parameters such as relaxation resonance frequency, damping factor, gain compression, and alpha factor can all be obtained by fitting modulation response and relative intensity noise (RIN) measurements for different lengths of fiber.

First, an expression for the gain is introduced based on a simple compression approximation. Next, the laser rate equations are used to derive the expressions for modulation response and RIN. In the next section, the equations for fiber propagation for

AM and FM signals are developed and used to analyze modulation response and relative intensity noise propagation in fiber.

Finally, a multimode description of the laser provides an explanation for the enhanced low frequency RIN due to fiber propagation. Correlated noise from several modes becomes decorrelated due to group velocity dispersion in the fiber resulting in a larger measured RIN for low frequencies after a few kilometers of propagation.

3.2. Semiconductor Laser Dynamics

3.2.1 Gain

Gain in semiconductors originates from delocalized electrons and holes combining to produce stimulated emission. The expression for gain at optical frequency ω is the result of integrating over the electron-hole density of states $\rho(\omega')$ multiplied by the Fermi population of those states multiplied by the Lorentian lineshape $g(\omega,\omega')$ for each single transition at ω'. The gain can be written generally in the form

$$G(\omega) = Y \int_{\frac{E_{gap}}{\hbar}}^{\infty} \rho(\omega')[f_c(\omega') - f_v(\omega')]g(\omega,\omega')d\omega' \qquad (3.1)$$

where Y includes a transition matrix element and spatial wavefunction for quantum well lasers [3–1]. The width of the Lorenzian lineshape for a particular 2-level electron hole pair is determined by the very fast (~100 femtoseconds) electron dephasing time.

For a DFB laser, the field is spatially distributed and stronger in the center of the cavity, leading to spatial hole burning, refractive index changes, and increased chirp. However, to a good approximation, simply the total number of carriers and photons are used in characterizing the gain above threshold. From a rate equation standpoint, it is also useful to obtain a linearized version of G for small signal characterization and noise measurements. Define small signal variations of the carrier density, N, and photon density, P, about the operating point:

$$\begin{aligned} N &= N_0 + \Delta N \\ P &= P_0 + \Delta P \end{aligned} \tag{3.2}$$

The gain, approximated to first order variations around a steady state compressed value is

$$G(N,P) \cong G(N_0,P_0) + \frac{\partial G}{\partial N}\Delta N + \frac{\partial G}{\partial P}\Delta P \tag{3.3}$$

where the derivatives are evaluated at N_0 and P_0. The differential gain terms are assigned unique symbols. The differential modal gain is defined as

$$A \equiv \frac{\partial G}{\partial N} \tag{3.4}$$

where v_g is the group velocity. The differential gain compression parameter is defined as

$$\varepsilon \equiv -\frac{1}{G_0}\frac{\partial G}{\partial P} \tag{3.5}$$

This leaves the expression for gain written in the form

$$G = G_0 + A\Delta N - \varepsilon G_0 \Delta P \tag{3.6}$$

3.2.2 Rate Equations

The dynamics of most semiconductor laser phenomena are contained in the system of coupled rate equations for carrier density, photon density, and optical frequency. These equations are treated in a number of sources [3–2], [3–3]

$$\begin{aligned}\frac{dN}{dt} &= \frac{I}{eV_a} - \frac{N}{\tau} - v_g G(N,P)P + \frac{F_1}{V_a} \\ \frac{dP}{dt} &= -\frac{P}{\tau_{ph}} + \Gamma v_g G(N,P)\left(P + \frac{n_{sp}K}{V}\right) + \frac{F_2}{V}\end{aligned} \tag{3.7}$$

I is the bias current, V_a is the active region volume, V is the mode volume of the cavity, v_g is the group velocity, and τ is the spontaneous emission lifetime. F_1 and F_2 are Langevin noise terms describing the behavior of spontaneous decay of carriers. The term $\Gamma v_g G\frac{n_{sp}K}{V}$ refers to the spontaneous emission rate into the lasing mode [3–4]. At reasonable operating points above threshold, $\frac{n_{sp}K}{V} << P$ and will be neglected in the experimental characterizations. Also in this limit, from the steady state operation condition, the gain tends to approach

$$G_0 \rightarrow \frac{1}{\Gamma v_g \tau_{ph}}. \tag{3.8}$$

Linearizing the rate equations (3.7) about the operating point N_0 and P_0 using the gain expression in (3.6) results in the small signal rate equations

$$\frac{d}{dt}\Delta N = \frac{\Delta I}{eV_a} - \left(\frac{1}{\tau} + v_g A P_0\right)\Delta N - \frac{(1-\varepsilon P_0)}{\Gamma\tau_{ph}}\Delta P + \frac{F_1}{V_a}$$
$$\frac{d}{dt}\Delta P = \Gamma v_g A P_0 \Delta N - \frac{\varepsilon P_0}{\tau_{ph}}\Delta P + \frac{F_2}{V} \qquad (3.9)$$

The instantaneous lasing frequency for semiconductor lasers is a time dependent function of the carrier and photon density and a linear approximation for the variations is needed to complete the rate equation description of the system. The photon rate equation emerges from the amplitude of the field evolution, and the phase rate equation yields the lasing frequency time dependence. Linearized, it is

$$\Delta\omega = \frac{\partial\omega}{\partial N}\Delta N + \frac{\partial\omega}{\partial P}\Delta P \qquad (3.10a)$$

The partial derivatives can be expanded with the chain rule for their dependence on the real and imaginary susceptibility, χ_r and χ_i

$$\Delta\omega = \frac{\partial\omega}{\partial\chi_r}\frac{\partial\chi_r}{\partial\chi_i}\frac{\partial\chi_i}{\partial G}\frac{\partial G}{\partial N}\Delta N + \frac{\partial\omega}{\partial\chi_r}\frac{\partial\chi_r}{\partial\chi_i}\frac{\partial\chi_i}{\partial G}\frac{\partial G}{\partial P}\Delta P \qquad (3.10b)$$

The first partial derivative is found by noting that the fractional change in lasing frequency is equal to the negative fractional change in the real part of the susceptibility times the confinement factor

$$\frac{\partial\omega}{\omega} = -\Gamma\frac{\partial\chi_r}{\chi_r} \qquad (3.11a)$$

The relationship between gain and imaginary part of the susceptibility is given by the power of e:

$$G = 2\frac{\omega\chi_i}{cn^2} \qquad (3.11b)$$

The factor of 2 is because the gain refers to power, which is the square of electric field.

By defining the α and β parameters

$$\alpha = \frac{\partial \chi_r}{\partial N} \Big/ \frac{\partial \chi_i}{\partial N} \quad \text{and} \quad \beta = \frac{\partial \chi_r^{(3)}}{\partial P} \Big/ \frac{\partial \chi_i^{(3)}}{\partial P} \tag{3.11c}$$

(3.10b) can be written as

$$\Delta\omega = -\left(\Gamma \frac{\omega}{\chi_r}\right)\alpha\left(\frac{cn^2}{2\omega}\right)A\Delta N + \left(\Gamma \frac{\omega}{\chi_r}\right)\beta\left(\frac{cn^2}{2\omega}\right)(-\varepsilon G_0)\Delta P \tag{3.12a}$$

Recognizing that $v_g = \frac{cn^2}{\chi_r}$ and $G_0 = \frac{1}{\Gamma v_g \tau_{ph}}$, Eqn. (3.12a) simplifies to

$$\Delta\omega = -\frac{\alpha}{2}\Gamma A v_g \Delta N + \frac{\beta}{2}\frac{\varepsilon}{\tau_{ph}}\Delta P + F_3 \tag{3.12b}$$

where the Langevin term F_3 accounts for spontaneous emission into the lasing mode, resulting in frequency fluctuations. Note that since the photon number dependence is only in $\chi^{(3)}$, β is usually accepted as 0 in most applications of (3.12b).

3.2.3 Modulation Response

Measuring the modulation response is a simple way of characterizing two of the most important semiconductor laser properties: the resonance frequency and the damping frequency. Other laser parameters such as α-parameter and $\varepsilon P/\tau_{ph}$ are obtained with dispersive propagation. The theoretical response is obtained by first setting the Langevin

forces to 0 and applying an $e^{i\Omega t}$ dependence to ΔI, ΔN, and ΔP, and transforming to the frequency domain. Fourier transforms are defined here according to

$$\Delta P(\Omega) = \int_{-\infty}^{\infty} \Delta P(t) e^{i\Omega t} dt \tag{3.13}$$

Solving the system (3.9) for $\Delta P(\Omega)$ by eliminating $\Delta N(\Omega)$ is straightforward and is found to be

$$\Delta P(\Omega) = \frac{\Delta I}{eV_a} \frac{\Gamma v_g A P_0}{\Omega_0^2 - \Omega^2 - i\gamma_0 \Omega} \tag{3.14}$$

where the relaxation frequency, Ω_0, is defined as

$$\Omega_0^2 = \frac{v_g A P_0}{\tau_{ph}} + \frac{\varepsilon P_0}{\tau \tau_{ph}} \tag{3.15}$$

and the damping factor, γ_0, is

$$\gamma_0 = \frac{1}{\tau} + v_g A P_0 + \frac{\varepsilon P}{\tau_{ph}} \tag{3.16}$$

Both parameters are given in radians/sec but are converted to Hertz by dividing by 2π. The modulation response, $MR(\Omega)$, is defined as the electrical signal response of the system as a function of Ω, normalized by the response at $\Omega=0$. The detected electrical signal is proportional to the intensity of the field, thus

$$MR(\Omega) = \frac{|\Delta P(\Omega)|^2}{|\Delta P(0)|^2} = \frac{\Omega_0^4}{\left(\Omega_0^2 - \Omega^2\right)^2 + \gamma_0^2 \Omega^2} \tag{3.17}$$

The electrical response in the system due to factors such as detector roll-off and RF pickup can be eliminated by dividing the modulation responses (subtraction of

logarithmic data) at two different operating conditions [3–5]. Since MR(Ω) is measured and modeled in dB in this thesis, subtraction of dB values is used for $MR_2(\Omega)/MR_1(\Omega)$. Figure 3.1 shows the subtraction modulation response for a quantum well DFB semiconductor laser from Lucent Technologies (formerly Ortel Corporation) operating at 1539 nm in wavelength. The signal current was modulated by using a microwave probe tip with a transmission strip line where it was combined with the bias current within a few hundred microns from the laser chip.

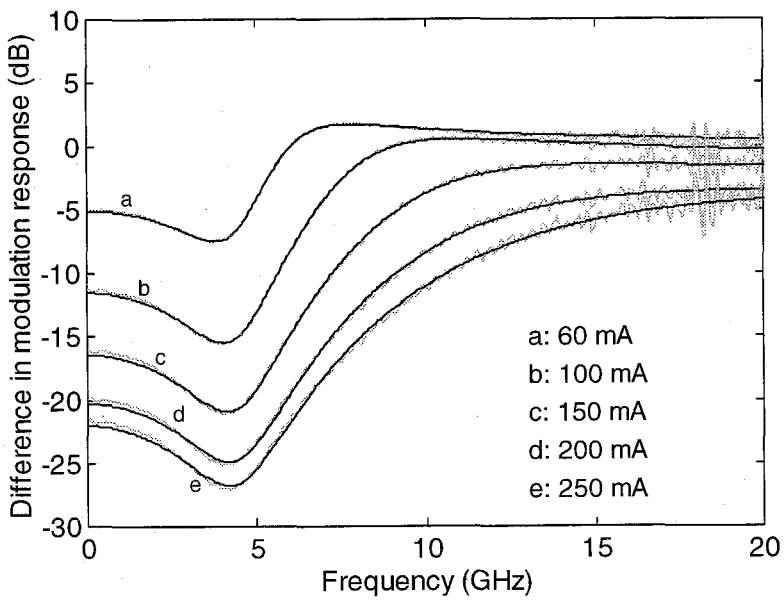

Figure 3.1. Difference in modulation responses.

Shown are the traces for the modulation response at the labeled bias current minus the modulation response at 40 mA bias current. The gray curves are the data and the solid black lines are the fitted curves.

Figure 3.2 shows the extracted parameters fit to a line by their expected linear dependence on output power.

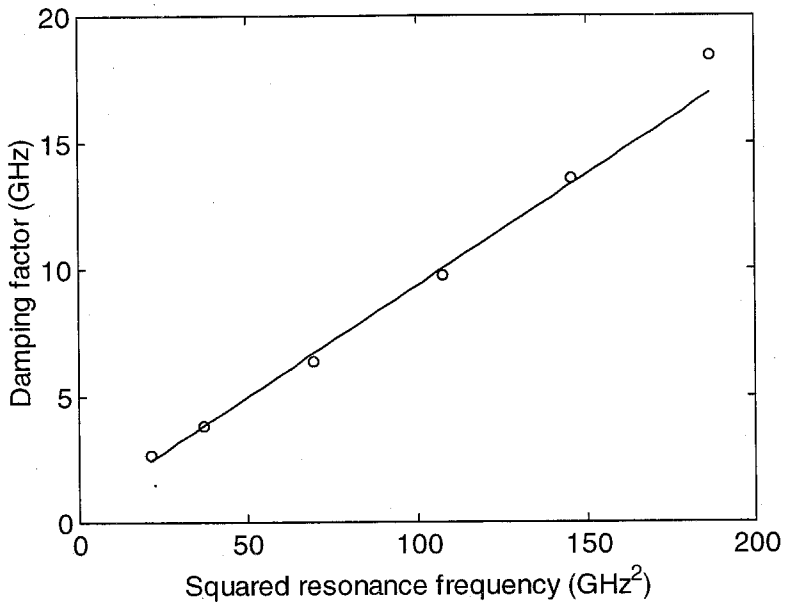

Figure 3.2. Damping factor versus squared resonance frequency.

The pure modulation response has been calculated with these extracted parameters and plotted for an intuitive understanding of the modulation response. At higher power levels, the relaxation resonance is pushed to higher frequencies, and the larger damping factor gives a flatter response, both reinforcing the advantage of high bias levels for direct small signal modulation.

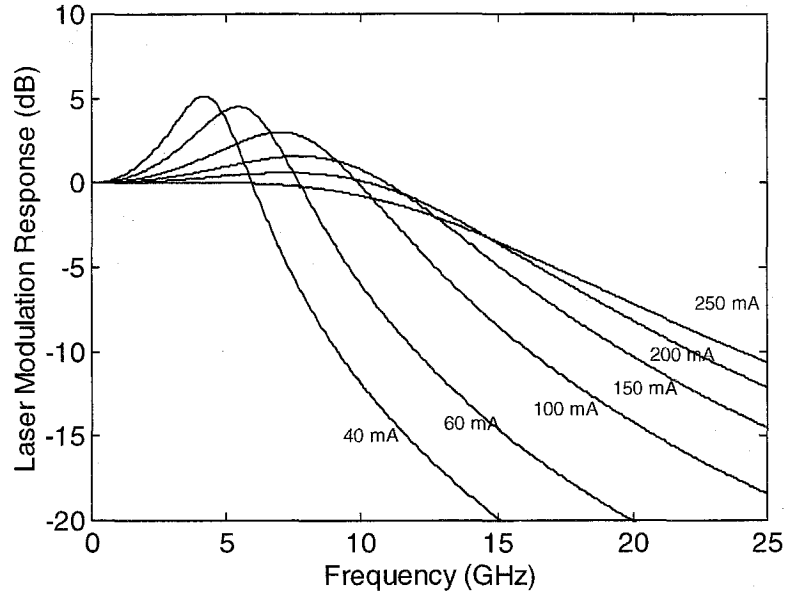

Figure 3.3. Calculated modulation response with the obtained parameters.

Recall that the lasing frequency is time dependent and a modulation of the current will cause a modulation of the frequency, known as chirp. Directly solving the small signal rate equations (3.9) for ΔN and substituting into (3.12b) results in the power dependent chirp equation

$$\Delta\omega(t) = -\frac{\alpha}{2P_0}\left[\frac{d}{dt}\Delta P(t) + \frac{\varepsilon P_0}{\tau_{ph}}\Delta P_0(t)\right] \tag{3.18}$$

The first term produces "transient chirp" and the second term produces "adiabatic chirp." Note the direct proportionality to the α-parameter. Typically the adiabatic chirp is most prominent, but high speed digital signals with fast rise times makes the transient term more important.

3.2.4 Relative Intensity Noise (RIN)

For laser systems that are closely, but not exactly, shot noise limited, a semi-classical description of noise based on the rate equations works well for describing the RIN spectrum and the effects of dispersive propagation in fiber. A Langevin force model for noise driven by spontaneous emission is contained in the works by Henry [3–6], [3–7], [3–8] and will be followed here.

We make use of the Langevin noise terms, F_1, F_2, and F_3 from the rate equations (3.9) and (3.12b). F_1 is associated with the recombination of carriers, F_2 is associated with the spontaneous emission of photons into the lasing mode, and F_3 is associated with the phase fluctuations from the spontaneous emission of photons into the lasing mode. In the spontaneous emission process, the loss of carriers results both in the generation of photons into the lasing mode and all other recombination processes, now termed F_1'. This correlation can be written as

$$F_1 = -F_2 + F_1' \tag{3.19}$$

with F_1', F_2, and F_3 as mutually uncorrelated noise sources. It is assumed that the spontaneous emission process is Markovian, meaning there is "zero memory" of past events, and the noise sources can be considered time-correlated by a delta function. Over the electronic frequencies of interest, it is quite acceptable to consider the Langevin forces as stationary Gaussian white noise processes, i.e., the spectral densities of the fluctuations, $S_{1'}(\Omega)$, $S_2(\Omega)$, $S_3(\Omega)$, are all constants.

The spectral density of the photon fluctuations, ΔP, for these noise sources is given by the Fourier transform of the autocorrelation of ΔP (Wiener-Khintchine theorem):

$$S_P(\Omega) = 2\int_{-\infty}^{\infty} C_P(\tau) e^{i\Omega\tau} d\tau \tag{3.20}$$

where

$$C_P(\tau) = \lim_{T\to\infty} \frac{1}{2T} \int_{-\infty}^{\infty} \Delta P(t)\Delta P(t+\tau) dt \tag{3.21}$$

Also in this approximation, the noise sources introduced are not considered to be time dependent processes, and so the time average of the fluctuations can be equated to the ensemble average with

$$C_P(\tau) = \overline{\Delta P(t)\Delta P(t+\tau)} \tag{3.22}$$

Using the Fourier transform definition of $\Delta P(\Omega)$ with (3.20) and (3.21), the total spectral density for the photon fluctuations, $S_P(\Omega)$ based on the Langevin terms, is found in

$$\overline{\Delta P(\Omega)\Delta P(\Omega')^*} = \pi S_P(\Omega)\delta(\Omega - \Omega') \tag{3.23}$$

The total spectral density of the photon variation is the additive sum from each independent source,

$$S_P(\Omega) = S_P^{(1)}(\Omega) + S_P^{(2)}(\Omega) + S_P^{(3)}(\Omega) \tag{3.24}$$

The relative intensity noise (RIN) of the laser output light is defined as this spectral density divided by the square of photon density, measured in units of dB/Hz

$$RIN(\Omega) = 10 \cdot \log_{10}\left[\frac{S_P(\Omega)}{P_0^2}\right] \tag{3.25}$$

Because measured electrical power is proportional to the square of received optical power, this quantity does not change with optical attenuation, present in fibers and inefficient detection systems.

The response of the photon fluctuations due to noise source F_1' is exactly the same as the response due to current modulation since they enter the rate equations (3.7) in the same manner. The only difference is the proportionality constants, and is found to be

$$S_P^{(1')}(\Omega) = \frac{(\Gamma v_g A P_0)^2}{\left(\Omega_0^2 - \Omega^2\right)^2 + \gamma_0^2 \Omega^2} \frac{S_{1'}(\Omega)}{(P_0 V)^2} \tag{3.26}$$

where the spectral density of the fluctuations alone, $S_{1'}(\Omega)$, is a constant equal to the rate of carriers which decay other than interacting with the lasing mode [3–9]. This contribution to the total RIN is experimentally found to be much smaller than the contribution from the F_2 noise source, which can be derived easily by setting $\Delta I = F_{1'} = 0$ eliminating ΔN in (3.7), and solving for ΔP in the frequency domain and using (3.23).

$$S_P^{(2)}(\Omega) = \frac{\Omega^2 + 1/\tau^2}{\left(\Omega_0^2 - \Omega^2\right)^2 + \gamma_0^2 \Omega^2} \frac{S_2(\Omega)}{(V/\Gamma)^2} \tag{3.27}$$

where $S_2(\Omega)$ is the spectral density of F_2 itself which is white over all frequencies of interest [3–10], [3–6]

$$S_2(\Omega) = \frac{4 n_{sp} K P_0 V}{\Gamma \tau_{ph}} = 8 (P_0 V/\Gamma)^2 K \omega_{ST} \tag{3.28}$$

where K is the Petermann correction factor for the non-uniformity of the photon density in DFB lasers and ω_{ST} is the Schawlow-Townes linewidth.

The F_3 noise contributes only to a constant phase noise and not intensity noise, so it has no contribution the RIN directly, i.e. $S_P^3(\Omega)=0$. However, by propagation in fiber, this FM contribution to the noise is converted to AM and appears in the RIN after propagation. It will be addressed in Section 3.3.3.

Measuring the RIN of a laser involves measuring the total noise of the laser with a high speed detector, amplifier, and an electronic spectrum analyzer. The electronic noise power contains several different components that must be treated separately. The RIN is the coefficient of the component that varies with the square of the photocurrent, the shot noise component varies linearly with the photocurrent, and all the constant noise terms are lumped into one "thermal" noise component [3–11]. The total noise power is

$$NP = GR\Delta\nu\left\langle i_{NP}^2\right\rangle = GR\Delta\nu\left[RIN\cdot i_d^2 + 2ei_d + N_{th}\right] \tag{3.29}$$

where $\left\langle i_{NP}^2\right\rangle$ is the squared current fluctuations, i_d is the DC photocurrent, R is the resistance, G is the amplifier gain, $\Delta\nu$ is the resolution bandwidth, e is the electron charge, and N_{th} is the total thermal noise.

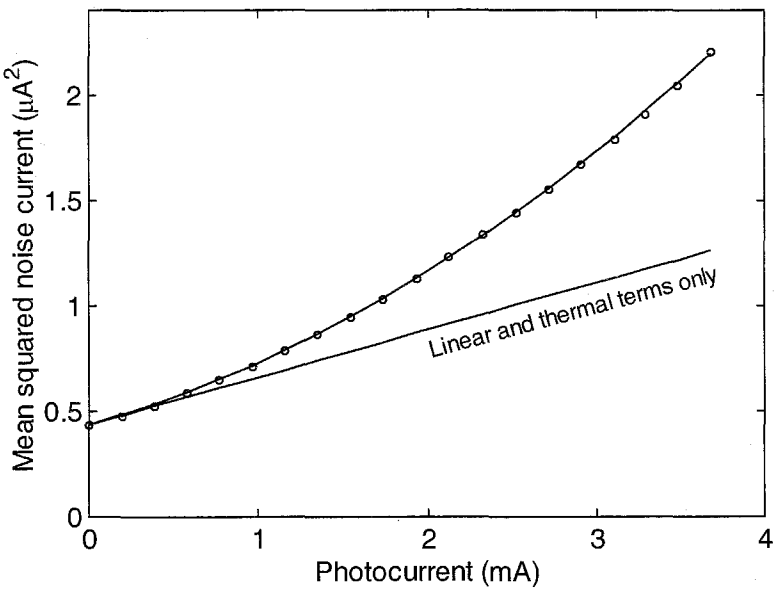

Figure 3.4. Noise power $\left\langle i_{NP}^2 \right\rangle$ versus photocurrent.

Figure 3.4 shows the total measured noise power as a function of optical attenuation (photocurrent) at 8.7 GHz, which is near the relaxation resonance where the RIN is high. The points are fitted to a quadratic polynomial and the RIN is the quadratic coefficient. Shown also is the linear (shot noise) and constant contributions to the noise power. This attenuation process is used to calibrate the shot noise at each electronic frequency for the parameter GRB for the linear coefficient in (3.29). Then the quadratic coefficient can be equated to the RIN directly. Figure 3.5 shows the extracted RIN for a DFB laser following this shot noise calibration.

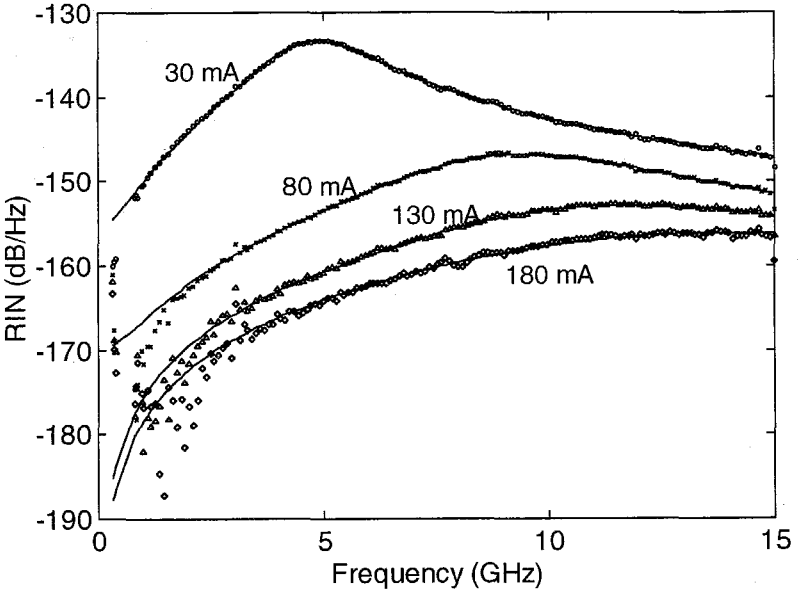

Figure 3.5. RIN vs. frequency for different bias levels.

The points are extracted from experimental noise data and the curves are fits to equation (3.25) with (3.27).

The power dependent resonance frequency and damping factor can be seen as well and as fitting parameters for the curves, they compare closely with those in Figure 3.2. Low frequency data is noisy and hard to fit closely because of the detector turn-on bandwidth limit and the low levels of RIN. There are reports of some low frequency RIN enhancements due to the presence of longitudinal side modes [3–12]. Little evidence of this effect has been observed; however, RIN enhancements after propagation due to mode decorrelation noise is measured and explored in Section 3.4.

3.3. Dispersive Propagation

The physics of wave propagation in fiber is covered in texts such as Agrawal [3–13]. This section considers the effect of dispersive propagation on small signal modulation and noise. Group velocity dispersion (GVD) refers to dependence of the group velocity on the optical frequency, and has a profound effect on wavelengths of 1.54 μm in standard fiber carrying data, known as FM-to-AM conversion. This effect is used to probe and characterize the α-parameter and $\varepsilon P_0/\tau_{ph}$ for a DFB laser. Other propagation effects such as attenuation, third-order dispersion, stimulated Brillouin scattering, and self-phase modulation are other important propagation effects, but can be made negligible for small signal study with fiber lengths less than 50 km and moderate power levels.

3.3.1. Signal Propagation Equations

Consider an electric field propagating in a fiber,

$$E(z,t) = E_0 e^{i(\omega t - \beta z)} \tag{3.30}$$

The propagation constant for the guided mode, Taylor expanded around a carrier, ω_0, is

$$\beta(\omega_0 + \Delta\omega) = \beta_0 + \beta'\Delta\omega + \frac{\beta''}{2}\Delta\omega^2 + \frac{\beta'''}{6}\Delta\omega^3 + \ldots \tag{3.31}$$

For group velocity v_g, the parameter of interest is

$$\beta'' \equiv \left.\frac{\partial^2\beta}{\partial\omega^2}\right|_{\omega_0} = \frac{\partial}{\partial\omega}\left(\frac{1}{v_g}\right) \tag{3.32}$$

Intuitively, $\beta'' \neq 0$ states that the index of refraction is wavelength dependent. The commonly quoted "dispersion parameter" specifies a time delay accrued in picoseconds for two signals spectrally separated by 1 nm after 1 km of propagation, given by

$$D = -\frac{2\pi c}{\lambda^2}\beta'' \tag{3.33}$$

Standard Corning fiber, SMF-28, has D~17 ps/(nm·km) at 1540 nm and is roughly 0 at 1310 nm, the two low-loss regimes of silica fiber used for optical communications. The dispersion parameter is determined mostly by the intrinsic material dispersion, but is also shaped by the geometry of the waveguide. Other examples of fibers with engineered dispersion parameters are double-clad fiber and dispersion-shifted fiber.

In order to derive the expression of the transfer function for dispersive propagation, consider a carrier wave, ω_0, with small signal modulation at frequency Ω. Let c_1 and c_2 be arbitrary complex modulation coefficients.

$$E(z,t) = E_0\left(e^{i(\omega_0 t - \beta_0 z)} + c_1 e^{i\left((\omega_0+\Omega)t - \left(\beta_0 + \frac{\Omega}{v_g} + \frac{\beta''}{2}\Omega^2\right)z\right)} + c_2 e^{i\left((\omega_0-\Omega)t - \left(\beta_0 - \frac{\Omega}{v_g} + \frac{\beta''}{2}\Omega^2\right)z\right)} \right) \tag{3.34}$$

Without loss of generality, we can set $t + \frac{z}{v_g} \rightarrow t$ in order to examine the moving time reference. Define the dispersion angle

$$\theta(\Omega, z) = -\frac{\beta''}{2}\Omega^2 z \tag{3.35}$$

Equation (3.34) becomes

$$E(t) = E_0 e^{i\omega_0 t}\left(1 + c_1 e^{-i\Omega t + i\theta} + c_2 e^{-i\Omega t + i\theta}\right) \tag{3.36}$$

As an aside, the general expression for the propagation of any bandwidth of light centered at ω_0 can be written as

$$E(z,t) = \frac{e^{i(\omega_0 t - \beta_0 z)}}{2\pi}\int_{-\infty}^{\infty} A(\Omega) e^{i\Omega t} e^{-i\frac{\beta''}{2}\Omega^2 z}\, d\Omega \tag{3.37}$$

where $A(\Omega)$ is the initial envelope function.

Now apply the relation (3.36) on an actual small signal of AM intensity modulation index m with phase ϕ_{AM} and FM index b with phase ϕ_{FM}:

$$E(t) = E_0\left[1 + m\cos(\Omega t + \phi_{AM})\right]^{1/2} e^{i[\omega_0 t + b\sin(\Omega t + \phi_{FM})]} \tag{3.38}$$

In the small signal approximation, this can be simplified as a carrier wave and two side bands by using the exponential forms for sine and cosine and using $(1+x)^{1/2} \approx 1 + \frac{1}{2}x$ and $e^x \approx 1 + x$ for $x << 1$. The result is

$$E(t) = E_0 e^{i\omega_0 t}\left[1 + e^{i\Omega t}\left(\frac{M}{4} + \frac{B}{2}\right) + e^{-i\Omega t}\left(\frac{M^*}{4} - \frac{B^*}{2}\right)\right] \tag{3.39}$$

where M and B are the complex modulation parameters $M = e^{i\phi_{AM}}$ and $B = e^{i\phi_{FM}}$.

After propagation, equations (3.36) and (3.39) can be combined and new AM and FM modulation indexes can be found by equating

$$\begin{aligned} \frac{M'}{4} + \frac{B'}{2} &= \left(\frac{M}{4} + \frac{B}{2}\right) e^{i\theta} \\ \frac{M'^*}{4} - \frac{B'^*}{2} &= \left(\frac{M^*}{4} - \frac{B^*}{2}\right) e^{i\theta} \end{aligned} \tag{3.40}$$

Adding and subtracting these equations and solving for the new complex modulation indexes yields

$$M' = M\cos\theta + 2iB\sin\theta$$
$$B' = B\cos\theta + \frac{i}{2}M\sin\theta \tag{3.41}$$

3.3.2. Modulation Response

The experimental goal here is to use the dispersive property of the fiber to obtain information about the semiconductor laser. First, the modulation response for a semiconductor laser is taken alone by applying a current modulation, ΔI, at frequencies 0-20 GHz and recovering the signal with a high speed detector and network analyzer. Next, the same conditions are repeated with the light passing through several kilometers of fiber. The division of the two responses eliminates the electrical parasitic effects and reveals a transfer function dependent solely on the dispersion in the fiber, the α-parameter, and another laser parameter

$$\kappa \equiv \frac{\varepsilon P_0}{\tau_{ph}} \tag{3.42}$$

The AM transfer function equation for the intensity modulation in fiber, $H_{AM}(\Omega)$ at modulation frequency Ω can be written in the form

$$H_{AM}(\Omega, z) = \frac{M'}{M} \tag{3.43}$$

The measured electrical power response is given by $\left|H_{AM}(\Omega, z)\right|^2$.

For a semiconductor laser, an expression is needed for the amount of FM modulation, B, at the output of the laser, which is correlated with the intensity modulation, M. Recall equation (3.18) and substituting in

$$\Delta P = MP_0 e^{i\Omega t} \tag{3.44}$$

results in

$$\Delta\omega = -\frac{\alpha M}{2}(i\Omega + \kappa) \tag{3.45}$$

The instantaneous optical frequency is the derivative of the field phase

$$\omega(t) = \frac{d\phi(t)}{dt} = \omega_0 + B\Omega\cos(\Omega t) \tag{3.46}$$

By substituting the magnitude of the frequency deviation, $\Delta\omega = B\Omega$, the FM index is found to be

$$B = -\frac{\alpha M}{2}\left(i + \frac{\kappa}{\Omega}\right) \tag{3.47}$$

The transfer function for the intensity modulation is now found from (3.41), (3.43), and (3.47) to be

$$H_{AM}(\Omega, z) = \frac{M'}{M} = \cos\theta(\Omega, z) + \alpha\left(1 + i\frac{\kappa}{\Omega}\right)\sin\theta(\Omega, z) \tag{3.48}$$

where $\theta(\Omega, z) = -\frac{\beta''}{2}\Omega^2 z$, as before. The electrical response is

$$\left|H_{AM}(\Omega, z)\right|^2 = (\cos\theta + \alpha\sin\theta)^2 + \alpha^2\left(\frac{\kappa}{\Omega}\right)^2\sin^2\theta \tag{3.49}$$

Figure 3.6 shows the modulation response for a DFB laser after 25 km of fiber at various bias levels. The modulation response of the laser itself is divided out, which eliminates the relaxation and damping frequency information. Each curve is fit to equation (3.49) and the parameters α, κ, and β" are extracted.

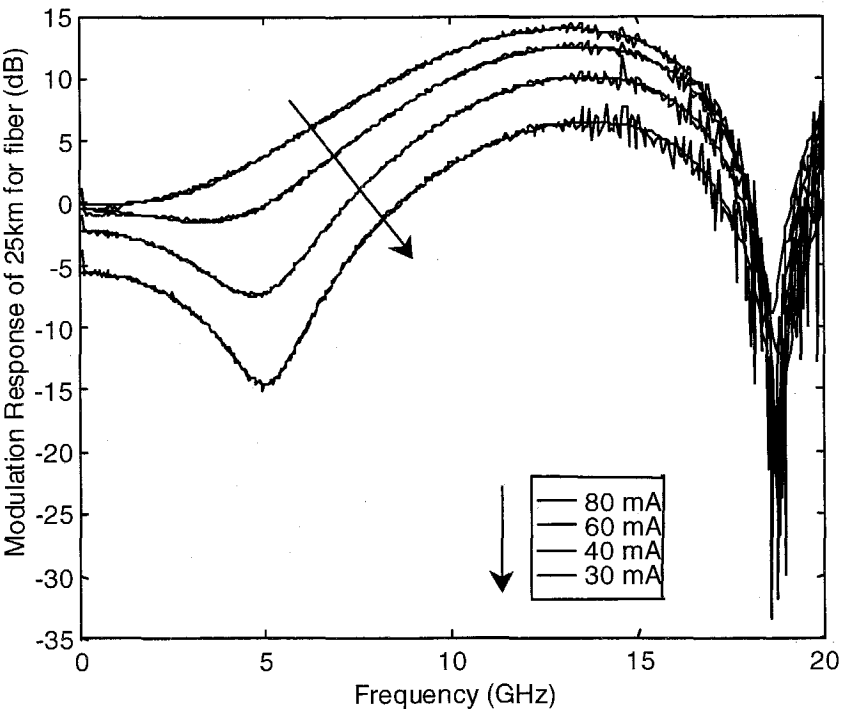

Figure 3.6. Modulation response for 25 km of fiber at various bias levels. Curve fits are overlaid on the data.

The lowest bias level refers to the lowest curve where κ is the smallest. The first dip here is evidence of the cosine and sin terms competing in the first squared term of (3.49). For higher power levels, the κ in the last term (adiabatic chirp) grows and increases H^2 at low frequencies, which reduces that first dip. The increase in the overall

height above 0 dB is due to $|\alpha|^2$ (transient chirp), when all the FM modulation power is coverted to AM in the fiber. Theoretically, all curves should intersect at 0,0, but there was some change in signal accounted for by the small signal modulation index not exactly repeated from trace to trace, and this merely shifts the overall curve up or down.

The α-parameter dependence on power is shown in Figure 3.7. Error bars were obtained with measurements with different fiber lengths and reflect the imperfect knowledge of the fiber length and various extracted dispersion parameters. κ, linearly proportional to P_0, was found to vary linearly from 1.6 GHz to 8 GHz.

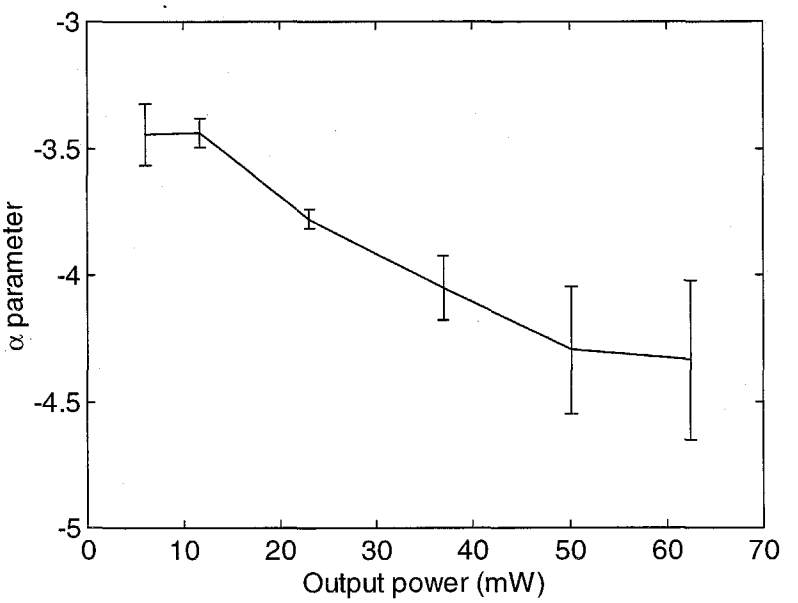

Figure 3.7. α-parameter versus laser output power.

3.3.3. RIN

After propagation in fiber, RIN is altered in the same physical manner. Intensity fluctuations undergo the effect of a transfer function. Since the noise source F_1' has the same response as intensity modulation, the transfer function is the same as well:

$$S_P^{(1')}(\Omega,z)=\left|H_{AM}(\Omega,z)\right|^2 S_P^{(1')}(\Omega) \tag{3.50}$$

However, as before, this term contributes typically negligibly to the RIN. The dominant contribution is due to the spontaneous emission into the lasing mode and is

$$S_P^{(2)}(\Omega,z)=\left|H_2(\Omega,z)\right|^2 S_P^{(2)}(\Omega) \tag{3.51}$$

This noise driven by F_2 contains both an AM and FM index. Section 3.2.4 treated only the AM index and found

$$M_2=\frac{\Delta P}{P_0}=\sqrt{\frac{S_P^{(2)}(\Omega)}{P_0^2}} \tag{3.52}$$

An expression for the frequency variations can be found by setting $\Delta I=F_1'=F_3=0$ in the small signal rate equations (3.9) and (3.12) and eliminating F_2 and ΔN variables:

$$\frac{d}{dt}\Delta\omega+\frac{1}{\tau}\Delta\omega=\frac{\alpha}{2}v_g A\left(\frac{d}{dt}\Delta P+\frac{1}{\tau_{ph}}\Delta P\right) \tag{3.53}$$

Assuming again a time dependence of $e^{i\Omega t}$, and transform this equation into the frequency domain, the solution for $\Delta\omega(\Omega)$ is

$$\Delta\omega(\Omega)=-i\frac{\alpha}{2\Omega}\frac{v_g A}{\tau_{ph}}\frac{1+i\Omega\tau_{ph}}{1-i/\Omega\tau}\Delta P(\Omega) \tag{3.54}$$

Now we substitute $\Omega_0^2=vgAP_0/\tau_{ph}$ from (3.15) and M_2 in (3.52). Then, using $\Delta\omega=B\Omega$ from (3.46), we arrive at the FM modulation index for the noise source driven by F_2:

$$B_2 = -iM_2 \frac{\alpha\Omega_0^2}{2\Omega^2} \frac{1+i\Omega\tau_{ph}}{1-i/\Omega\tau} \tag{3.55}$$

Finally, the transfer function can be written directly using the propagation equation (3.41)

$$H_2(\Omega,z) = \cos(\Omega,z) + \alpha \frac{\Omega_0^2}{\Omega^2}\left[\frac{1+i\Omega\tau_{ph}}{1-i/\Omega\tau}\right]\sin\theta \tag{3.56}$$

Noise driven by F_3 has no AM index, as discussed in Section 3.2.4, but the FM index is

$$B_3 = \frac{\Delta\omega(\Omega)}{\Omega} = \frac{\sqrt{S_3(\Omega)}}{\Omega} \tag{3.57}$$

and so contributes to the RIN by

$$S_P^{(3)}(\Omega) = 4S_3(\Omega)\frac{\sin^2(\Omega,z)}{\Omega^2} \tag{3.58}$$

where [3–9]

$$S_3(\Omega) = \left(\frac{\Gamma}{2P_0V}\right)^2 S_2(\Omega) = 2K\omega_{ST} \tag{3.59}$$

The final expression for RIN after propagation is

$$RIN(\Omega,z) = 10\cdot\log_{10}\left[8K\omega_{ST}\left(|H_2(\Omega,z)|^2 \frac{\Omega^2 + 1/\tau^2}{(\Omega_0^2-\Omega^2)^2+\gamma_0^2\Omega^2} + \frac{\sin^2(\Omega,z)}{\Omega^2}\right)\right] \tag{3.60}$$

Figure 3.8 show the change in RIN after propagation in two separate fibers. ΔRIN is the measured after fiber divided by the measured RIN before fiber. The curves are the fits to equation (3.60).

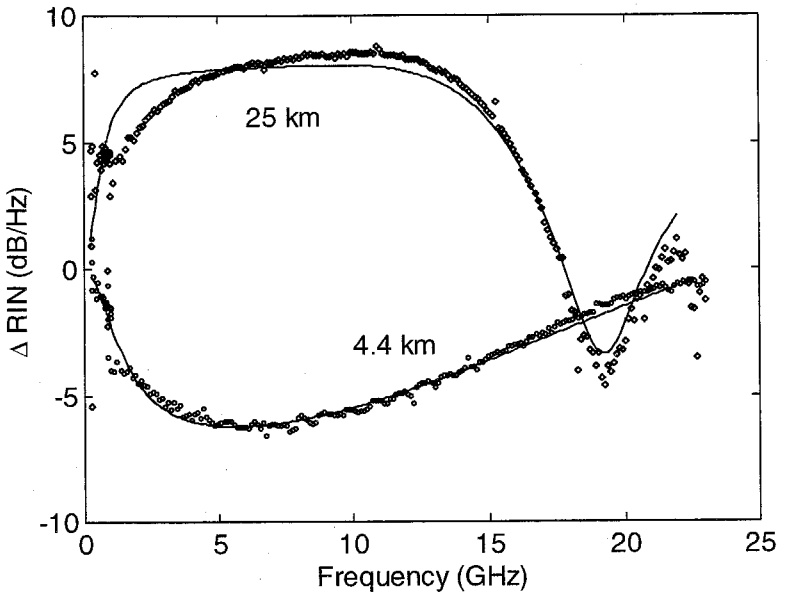

Figure 3.8. Change in RIN for 4.4 km and 25 km for 100 mA laser bias.

The extracted parameters for the laser used at 100 mA bias were τ=.16 ns, τ_{ph}=7.4 ps, α=-4.8±0.3, and $K\omega_{ST}=4.5\times10^{5}\ s^{-1}$. Since $\tau >> \tau_{ph}$, it can be noted that for frequencies in the range of $\frac{1}{\tau} << \Omega << \frac{1}{\tau_{ph}}$ and for small fiber lengths (z < 3km), the RIN can be reduced uniformly. Under these approximations, H_2 can be written as

$$H_2(\Omega, z) \approx 1 - \alpha\Omega_0^2\beta'' z \tag{3.61}$$

Beyond this short length, the interplay of the terms in the full expression takes over giving rise to the structure seen in Figure 3.8. For the 25 km section, the Ω dependence is similar to the modulation response revealing the same Ω^2 dependence in the cosine and sine terms

3.4. Multimode Effects

The performance of optical communication systems is strongly affected by laser RIN, which is a critical factor in determining the signal to noise ratio. Since the spectral gain of semiconductor lasers is very broad, a relatively large number of side modes carry enough noise power to affect the performance of the laser diode, especially at low frequencies. Individual longitudinal modes can exhibit large intensity fluctuations, called mode partition noise (MPN), even though the total intensity remains low due to anticorrelation among pairs of longitudinal modes. This phenomenon is harmless in the absence of fiber dispersion; however, with propagation, different phases acquired by different frequencies destroys the anticorrelation, and causes an increase in measured RIN [3–14].

The side modes in the stop band of the DFB laser are highly suppressed. Outside this band, there are many Fabry-Perot cavity modes that have similar power over a large bandwidth, shown in Figure 3.9. The optical spectrum is used to determine the power in each of the side modes and their separation from the main mode, and around 30 modes are necessary to explain the increase in RIN.

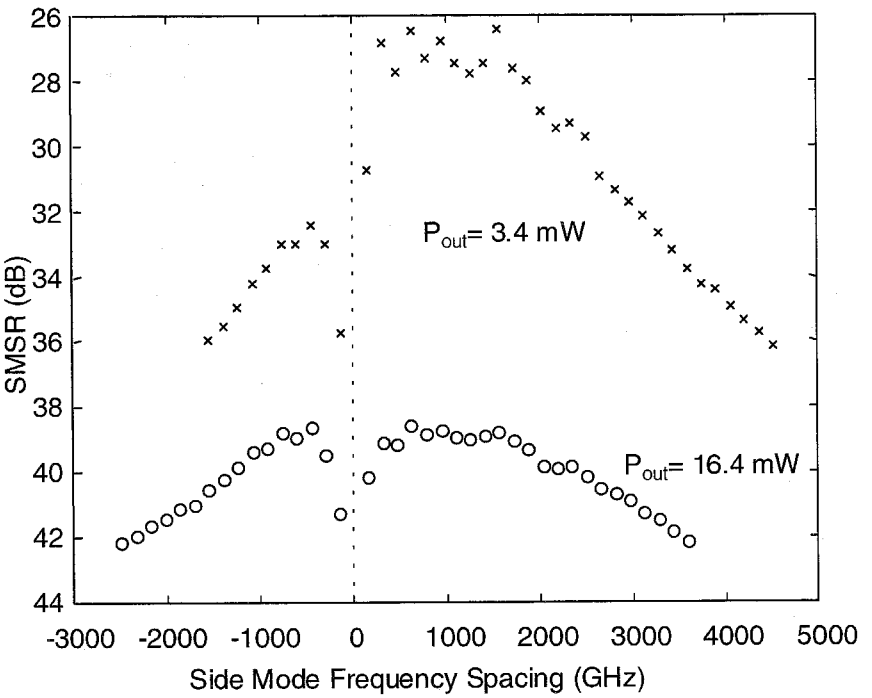

Figure 3.9. Side mode suppression ratio (SMSR).

Pout=3.4 mW (crosses) and Pout=16.4 mW (circles) as a function of the frequency deviation from the main mode.

Theoretical treatment begins with the linearized gain equation (3.6) with a new term $C_{km} = -\frac{\partial G_k}{\partial P_m}$, which is the cross term that accounts for the gain in one mode affected by the optical power in the other modes.

$$G_k = G_{0k} + v_g A_k \Delta N - \varepsilon_k G_{0k} \Delta P_k - \sum_{m \neq k} C_{km} \Delta P_m \tag{3.62}$$

The resulting transformed small signal rate equations are

$$(i\Omega + \Gamma_N)\Delta N = \frac{F_i}{V_a} - \sum_k \overline{G}_{0k} \Delta P_k \tag{3.63}$$

$$(i\Omega + \Gamma_{P_k})\Delta P_k = \frac{F_{2k}}{V} + \Gamma v_g A_k P_k \Delta N - \sum_{m \neq k} \Gamma C_{km} P_k \Delta P_m \tag{3.64}$$

$$i\Omega \Delta\phi_k = -\frac{\alpha_k}{2} \Gamma v_g A_k \Delta N + F_{3k} \tag{3.65}$$

where $\Gamma_N = \frac{1}{\tau} + \sum_k G_{0i} P_k$, $\Gamma_{P_k} = \frac{R_{spk}}{P_k} + \Gamma \varepsilon_k G_{0k} P_k$ and

$\overline{G}_{0k} = G_{0k} - \varepsilon_k G_{0k} P_k - \sum_{m \neq k} \theta_{mk} P_m$. R_{spk} is the spontaneous emission rate per unit volume into the lasing mode k.

The gain margin, $\Delta\overline{G}_{0k}$, which is defined as the difference between the inverse of the photon lifetime and the temporal gain constant of the mode, determines the CW power, P_k, according to $P_k = \frac{R_{spk}}{\Delta\overline{G}_{0k}}$ [3–15]. For side modes below threshold, dynamic variations in the gain are small compared to the gain margin, which is very large and dominates the rate at which the photon density fluctuations are damped. Thus, for a side mode, ΔP_k is essentially independent of fluctuations in the carrier density and the photon density of the other modes, and (3.65) approximates to

$$\Delta P_k = \frac{F_{P_k} / V}{i\Omega + \frac{R_{spk}}{P_k}}, \quad k \neq 0 \tag{3.66}$$

for the side modes. The main mode is denoted by k=0.

Following Section 3.4.2, the Langevin forces F_{2k} of different modes are uncorrelated, and the photon density fluctuations of each of the side modes, ΔP_k, can be considered as independent noise sources, justifying $F_1 = F_1' - \sum_k F_{2k}$. Thus, the photon and carrier density variations in the main mode are given by

$$\Delta P_0 = \Delta P_0^{N'} + \Delta P_0^{P_k} + \sum_{k\neq 0} \Delta P_0^{P_k} \tag{3.67}$$

$$\Delta N = \Delta N^{N'} + \Delta N^{P_0} + \sum_{k\neq 0} \Delta N^{P_0} \tag{3.68}$$

where the superscripts denote which source (carrier or photon density) as well as main mode (0) or side mode (k). Contributions to ΔN and ΔP_0 originating from carrier noise, $\Delta P_0^{N'}$ and $\Delta N^{N'}$, and from spontaneous emission in the main mode, $\Delta P_0^{P_0}$ and ΔN^{P_0}, are approximately the same as those obtained with single mode theory. The additional fluctuations caused by the side modes is given by

$$\Delta P_0^{P_k} = -\left[G_0 P_0 \frac{i\Omega + \Gamma_{P_k} + \Gamma\overline{G}_{0k}}{D(\Omega)} + \Gamma C_{0k} P_0 \frac{i\Omega + \frac{1}{\tau} + G_0 P_0}{D(\Omega)} \right] \Delta P_k \equiv p_{0k} \Delta P_k \tag{3.69}$$

$$\Delta N^{P_k} = \frac{1}{\Gamma G_0 P_0} \left[i\Omega + \Gamma\varepsilon_0 G_0 P_0 + p_{0k}\Gamma C_{0k} P_0 \right] \Delta P_0^{P_k} \tag{3.70}$$

where $D(\Omega) \equiv \Omega_0^2 - \Omega^2 + i\gamma_0\Omega$ is the resonant denominator. Equation (3.69) shows that the additional fluctuations in the main mode are anticorrelated with the noise source ΔP_k that produces them. Two effects are present: first, depletion of carriers due to spontaneous and stimulated emission into the k^{th} side mode, and second, compression of the gain of

the main mode by the power in the side modes. From equations (3.65) and (3.68), the phase fluctuations in mode k due to spontaneous emission in mode m is given by

$$\Delta\phi_k^{P_m} = -\frac{\alpha_k}{2}\frac{G_{N_k}}{i\Omega}\Gamma\Delta N^{P_m} \tag{3.71}$$

Since the different noise sources are uncorrelated, the spectral densities are additive and their effects can be considered separately. The total RIN at the receiver in the case of a nearly single mode laser is given by

$$RIN(\Omega,z) \cong RIN_0(\Omega,z) + \sum_{k\neq 0}\frac{\left\langle \left| H_0^{P_k}\Delta P_0^{P_k} + H_k^{P_k}\Delta P_k^{P_k}\right|^2\right\rangle}{P^2} \tag{3.72}$$

where RIN_0 is the RIN from single mode theory and the summation term is additive for each side mode noise term correlated with itself and the main mode. The phase noise terms from the side modes, F_{ϕ_k}, can be neglected because of the mode power squared term in the denominator which is small for side modes. The transfer function $H_k^{P_k}$ is analogous to the H_2 in the single mode case. In general, the small signal transfer function for variations in mode k due to power in mode m is given by

$$H_k^{P_m} = \left[\cos(\theta) - 2P_k\frac{\Delta\phi_k^{P_m}}{\Delta P_k^{P_m}}\sin(\theta)\right]\exp(i\psi_k) \tag{3.73}$$

where $\theta = -\frac{1}{2}\beta''\Omega^2 z$ and $\psi_k = -\beta''\Delta\omega_k\Omega z$, and $\Delta\omega_k$ is the optical frequency spacing between mode k and the main mode. The factor $\exp(i\psi_k)$ accounts for the group delay of side modes relative to the main mode. Substitution of (3.70) into (3.71) into (3.73) yields

$$H_0^{Pk}\Delta P_0^{Pk} + H_k^{Pk}\Delta P_k^{Pk} =$$
$$= \left[\cos\theta(\exp(i\psi_k) + p_{0k}) + \alpha_0 \sin\theta\left(p_{0k} + \frac{p_{0k}\Gamma\varepsilon_0 G_0 P_0 + \Gamma\theta_{0k}P_0}{i\Omega}\right)\left(1 + \frac{\alpha_k}{\alpha_0}\frac{G_k P_k}{G_0 P_0}\exp(i\psi_k)\right)\right]$$
$$\approx [\cos\theta(\exp(i\psi_k) + p_{0k}) + p_{0k}\alpha_0 \sin\theta]\Delta P_k \qquad (3.74)$$

The approximation in the last line of (3.72) is valid for small angles $\theta<<1$ and neglects the modal dependence of the linewidth enhancement parameter, α_k and the differential gain, G_k, and assumes a large SMSR. Also, it shows why even highly suppressed side modes can contribute significantly to the RIN after propagation in dispersive fiber. As a consequence of the difference in group velocities of the longitudinal modes traveling in dispersive fiber, the fluctuations originating in the side modes no longer cancel out, but cause oscillations in the noise power at the receiver. It can be seen that there is an overall increase in the RIN that rolls off at high frequencies due to the low-pass characteristic of the noise source ΔP_k.

In order for the MPN to have a significant value at a given modulation frequency, ψ_k has to be close to $\pi(1+2m)$ for one or several of the dominant side modes, where m is an integer. The frequency separation between the main mode and the k^{th} mode is given approximately by $\Delta\omega_k \sim |k|\frac{2\pi c}{L}$, where L is the laser length, c is the speed of light, and k is the mode index. Thus, assuming a typical value β'' = -20 ps^2/km at 1.54 μm, the condition becomes $\Omega \approx \frac{(1+2m)L/z}{|k|2c|\beta''|} \approx 0.1\frac{(1+2m)}{|k|}\frac{L(\mu m)}{z(km)}$. If L/|k| is much larger than the propagation distance, z, i.e., for side modes close to the main mode and short lengths

of fiber, the frequencies at which the previous condition is satisfied are so high that an increase in RIN is no longer seen.

The relative intensity noise of a 250 μm length DFB laser at 1.54 μm was measured before and after propagation in various lengths of standard single mode optical fiber, shown in Figure 3.10.

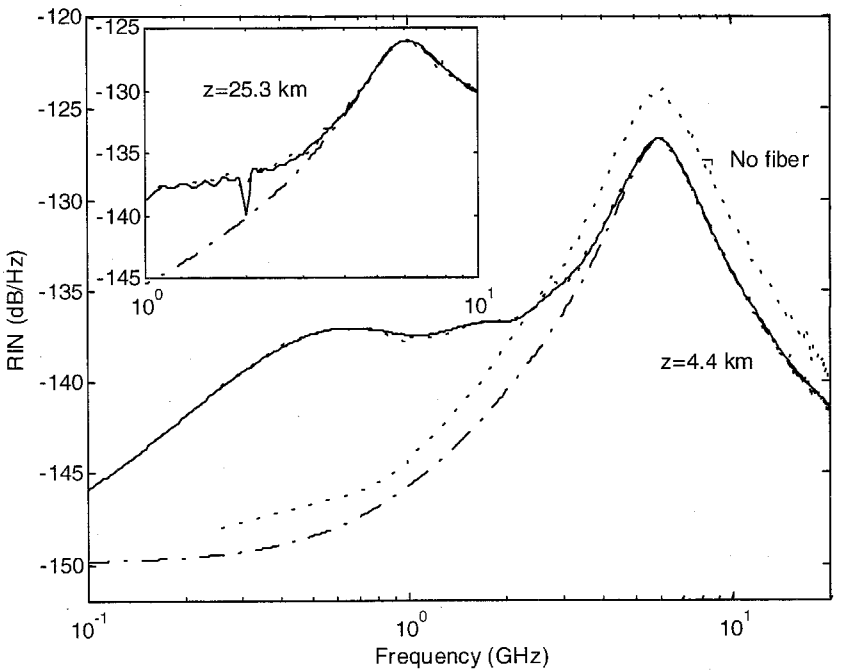

Figure 3.10. RIN measured before and after fiber.

4.4 km and 25.3 km (inset) of fiber at Pout=3.4 mW, Ibias=1.6 I_{th}, SMSR=27 dB. The dotted curve is the experimental data, the solid line is the multimode theory and the dash-dotted line is single mode theory.

A good fit to the standard single mode theory was obtained before adding fiber, from 2 to 20 GHz. The noise without fiber was used to determine R_{sp0}, Ω_0, and γ_0 at

each operating point. The rest of the parameters were estimated from the noise with fiber, yielding α=-4.6, τ=0.27 ns, τ_{ph}= 5.5 ps and β''= - 20 ps^2/km. Equation (3.74) was used in the simulations, and the nonlinear gain coefficients were assumed to have a wavelength dependence as that in [3–12]. The increase in the RIN over the frequency range of 500 MHz to 5 GHz is not well explained by Su et al. [3–12], who introduced an asymmetric nonlinear gain coefficient to explain the increase in low frequency RIN. It is also not well explained with any kind of 1/f noise, nor noise originating from F_1'. In the inset of Figure 3.10, the notch observed both in the simulations and in the experiment corresponds to the condition where all modes arrive in phase. This occurs when $-\beta_2 \Delta\omega\Omega z$ is an integer multiple of π, with $\Delta\omega$ the mean mode spacing.

Figure 3.11 shows the RIN for higher operating bias before and after propagation in 4.4 km of fiber. It is interesting to note in Figure 3.11 that even at very high output powers and SMSR's, the effect of the side modes can be noticeable in the range of frequencies used in optical communication systems.

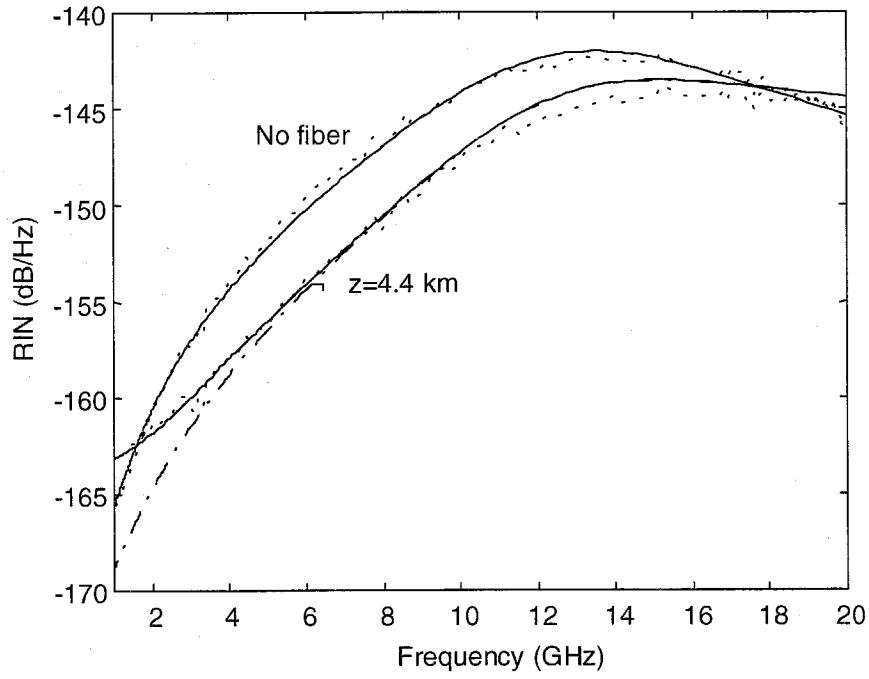

Figure 3.11. RIN measured after 4.4 km of fiber and high bias. Pout=16.4 mW, Ibias=4.1 I_{th}, SMSR=40 dB. The dotted curve is the experimental data, the solid line is the multimode theory and the dash-dotted line is single mode theory.

3.5. Summary

Before propagation in fiber, both the single mode and multimode models yield similar results that agree very well with experiment. However, after fiber the single mode theory underestimates the low frequency RIN. For some fiber lengths the single mode theory predicts a reduction in RIN [3–9], which is not necessarily achieved when the multimode model is used, also seen experimentally.

This study shows that the best performing lasers need to have better SMSR than current DFB semiconductor lasers. New technology in mode selection and wavelength control of fiber Bragg gratings combined with erbium-doped fiber amplifiers make possible more highly single mode lasers at 1.54 μm developed in Chapter 6. Fiber Bragg gratings: theory, fabrication, and applications are the focus of the remainder of this thesis.

References for Chapter 3

[3–1] Y. Arakawa and A. Yariv, "Quantum well lasers -- gain, spectra, dynamics," IEEE J. Quan. Elect, 22, pp. 1887-1899 (1986).

[3–2] Larry A. Coldren and Scott W. Corzine, *Diode Lasers and Photonic Integrated Circuits,* Wiley-Interscience, 1995.

[3–3] M. Sergent III, M. O. Scully, and W. E. Lamb, Jr., *Laser Physics,* Addison-Wesley, Reading, MA, 1974.

[3–4] K. Petermann, "Calculated spontaneous emission factor for double heterostructure injection lasers with gain-induced waveguiding," IEEE J. Quant. Elec. 15, pp. 941-946 (1979).

[3–5] P.A. Morton, T. Tanbun-Ek, R. A. Logan, A. M. Sergent, P.F. Sciortino, Jr., and D. L. Coblentz, "Frequency response subtraction for simple measurement of intrinsic laser dynamic properties," IEEE Phot. Tech. Lett. v, (2), pp. 133-136 (1992).

[3–6] C. H. Henry, "Theory of the linewidth of semiconductor lasers," IEEE Jour. Quan. Elec. 18, pp. 259-264 (1982).

[3–7] C. H. Henry, "Theory of spontaneous emission noise in open resonators and its application to lasers and optical amplifiers," Jour. Light. Tech. 4, pp. 288-297 (1986).

[3–8] C. H. Henry, "Theory of the phase noise and power spectrum of a single-mode injection laser," IEEE Jour. Quan. Elec. 19, pp. 1391-1397 (1983).

[3–9] W. K. Marshall, J. Paslaski, and A. Yariv, "Reduction of relative intensity noise of the output field of semiconductor lasers due to propagation in dispersive optical fiber," Appl. Phys. Lett. 68, p. 2496-2498 (1996).

[3–10] J. Wang, N. Schunk, and K. Petermann, "Linewidth enhancement for DFB lasers due to longitudinal field dependence in the laser cavity," Elec. Lett. 23, pp. 715-717 (1987).

[3–11] A. Yariv, *Optical Electronics in Modern Communications,* Oxford University Press (1997).

[3–12] C. B. Su, "Explanation of low-frequency relative intensity noise in semiconductor lasers," Appl. Phys. Lett. 57, (9), pp. 848-851 (1990).

[3–13] Govind P. Agrawal, *Nonlinear Fiber Optics,* Academic Press (1995).

[3–14] E. Peral, W. K. Marshall, D. Provenzano, and Amnon Yariv, "Effect of many weak side modes on relative intensity noise of distributed feedback semiconductor lasers," Appl. Phys. Lett. 72, (8), p. 888-890 (1998).

[3–15] K. Petermann, *Laser modulation and noise*, Kluwer, (1991).

Page 60 is a blank page.

Chapter 4 - Fiber Bragg Gratings

4.1. Introduction

The speed at which the fiber optics industry has advanced in recent years has created a host of new demands and new opportunities. One area now undergoing vast commercial development is Dense Wavelength Division Multiplexing (DWDM), the process of sending several, independent data streams, each with its unique wavelength, on a single fiber. This requires very fine wavelength selective devices. Fiber Bragg gratings (FBG's) are such devices capable of providing the wavelength sensitivity to meet these imposing demands [4–1]. Millimeters in length, Fiber Bragg gratings can completely reflect a narrow band of light into the backward propagating direction [4–2]. Figure 4.1 shows a schematic of a fiber Bragg grating. The optical mode (A) can be reflected back into the reverse propagation mode (B) when the wavelength of light matches the Bragg wavelength for the grating.

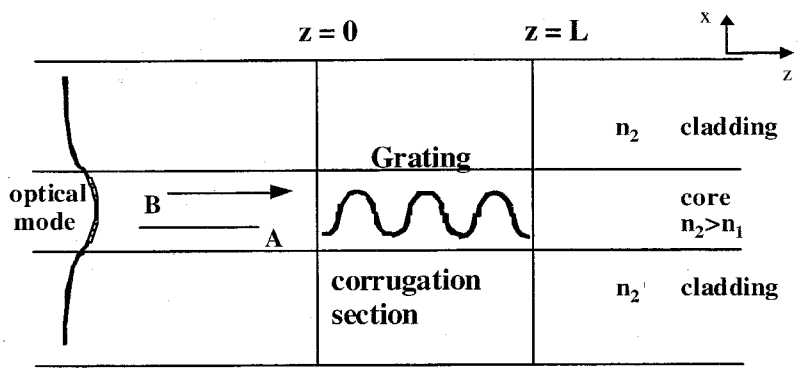

Figure 4.1. Schematic of fiber Bragg grating.

Today's commercial optical communications uses for FBG's include bandwidth filtering, dispersion compensation, add/drop channel control for wavelength division multiplexing, and laser frequency stabilization. These powerful, all-fiber devices can also be used for some new applications proposed here [4–3], [4–4], [4–5], [4–6].

The next section will introduce the theory of these devices, based on the coupled mode approach. The following sections will demonstrate the usefulness of numerical methods, which can calculate the transmission properties of arbitrarily apodized and chirped gratings. Experimental data is then presented showing growth, transmission, and other properties. Fits to the theoretical predictions show that even imperfect gratings can be well modeled.

4.2. Theoretical Solution

The most convenient analysis of 1-D periodic grating structures in fibers is the coupled mode analysis. Gratings are a periodic modulation of the guide index of refraction by a small amount, typically 10^{-4} ~ 10^{-3}. Gratings are formed by exposure to an interference pattern from two coherent UV laser beams. The index is typically raised according to the intensity of radiation. For this analysis of single mode fiber, it suffices quite well to assume each cross section of the fiber has a uniform index for the core and cladding based on the exposure. However, some exposure techniques are implemented to create an index gradient across the core to induce birefringence.

Assume, for a uniform grating, that the index of refraction has the form [4–1]

$$n(z) = n_0(1+\sigma(z)) + \frac{\Delta n}{n_0}\cos[2n_0k_0z + 2\phi(z)] \tag{4.1}$$

where n_0 is the initial index of the fiber, σ is an average background change in index, and ϕ is a random offset phase. The physical grating in the fiber has periodicity

$$\Lambda_g = \frac{2\pi}{2nk_0} \equiv \frac{\lambda_B}{2n} \tag{4.2}$$

where λ_B is the Bragg wavelength, the wavelength about which there will be reflection by the grating. This phase can also be used to describe a chirp in the grating (i.e. $\frac{d\phi}{dz} \neq 0$). We will leave this option in for generality. Deriving the coupled mode equations that describe the grating behavior begin with the wave equation:

$$\nabla^2 E - \frac{1}{v^2}\frac{d^2E}{dt^2} = 0, \text{ with } v = \frac{\omega}{kn(z)} \tag{4.3}$$

where n(z) is the index. Choose the following convention for the electric field evolution: $E(z,t) = B(z)e^{i(\omega t - n_0 k_0 z)} + A(z)e^{i(\omega t + n_0 k_0 z)}$ for travelling waves in the z-direction, where B is the field amplitude for the right (forward) travelling wave and A is the field amplitude of the left travelling wave (backward) as in Figure 4.1. The small perturbation in the index allows for certain approximations which still accurately maintain the principal properties of observed gratings. With these perturbations substituted, the wave equation is approximated as

$$\frac{d^2E(z,t)}{dz^2} = -(k_0 + \Delta k)^2 n_0^2 \left(1 + \sigma + \frac{\Delta n}{n_0}\cos(2k_0 n_0 z + 2\phi)\right)^2 E(z,t) \tag{4.4}$$

Define $\gamma = n_0 k_0 z + \phi$ and use the identity $2\cos\gamma = e^{i\gamma} + e^{-i\gamma}$. Substituting for E, results in the equation

$$\begin{aligned} -2in_0k_0\frac{dB}{dz}e^{-in_0k_0z} + 2in_0k_0\frac{dA}{dz}e^{in_0k_0z} - n_0^2k_0^2Be^{-in_0k_0z} - n_0^2k_0^2Ae^{in_0k_0z} = \\ -n_0^2k_0^2\left[\left(1+\frac{\Delta k}{k_0}\right)\left(1+\sigma+\frac{\Delta n}{2n_0}\left(e^{i\gamma}+e^{-i\gamma}\right)\right)\right]^2\left(Be^{-in_0k_0z} + Ae^{in_0k_0z}\right) \end{aligned} \tag{4.5}$$

We need to make another substitution to remove the ϕ in the exponential:

$$B = ue^{-i\phi} \text{ and } A = ve^{i\phi} \tag{4.6}$$

Also, by Taylor expanding the squared term for small σ and Δn, the approximation equation becomes (neglecting second order terms for the envelope derivatives):

$$-2in_0k_0\frac{du}{dz}e^{-i\frac{\gamma}{2}}-2n_0k_0ue^{-i\frac{\gamma}{2}}\frac{d\phi}{dz}+2in_0k_0\frac{dv}{dz}e^{i\frac{\gamma}{2}}-2n_0k_0ve^{i\frac{\gamma}{2}}\frac{d\phi}{dz}...$$
$$...-n_0^2k_0^2ue^{-i\frac{\gamma}{2}}-n_0^2k_0^2ve^{i\frac{\gamma}{2}}=-n_0^2k_0^2\left[1+2\left(\frac{\Delta k}{k_0}+\sigma\right)+\frac{\Delta n}{n_0}\left(e^{i\gamma}+e^{-i\gamma}\right)\right]\left(ue^{-i\frac{\gamma}{2}}+ve^{i\frac{\gamma}{2}}\right) \quad (4.7)$$

Return to the B, A variables by simply redefining B = u and A = v. Collecting terms of $e^{-i\frac{\gamma}{2}}$ and $e^{i\frac{\gamma}{2}}$ results in two equations, known as the coupled mode equations:

$$\frac{dB}{dz}=-in_0k_0\left(\frac{\Delta k}{k_0}+\sigma-\frac{d\phi}{dz}\right)B+\frac{\Delta n}{n_0}A$$
$$\frac{dA}{dz}=in_0k_0\left(\frac{\Delta k}{k_0}+\sigma-\frac{d\phi}{dz}\right)A+\frac{\Delta n}{n_0}B \quad (4.8)$$

These equations can be solved analytically for the case of uniform, unchirped gratings with a constant background index. Define the following variables that are independent of z:

$$\alpha\equiv\frac{\Delta k}{k_0}+\sigma-\frac{d\phi}{dz}$$
$$\gamma^2\equiv n_0^2k_0^2\left(\left(\frac{\Delta n}{2n_0}\right)^2-\alpha^2\right) \quad (4.9)$$

To solve, take another derivative with respect to z and substitute to eliminate A from the B equation. The coupled mode equations can now be reduced to

$$\frac{d^2B}{dz^2}=\gamma^2B \text{ and } \frac{d^2A}{dz^2}=\gamma^2A \quad (4.10)$$

which have the solution

$$B(z)=a\cosh(\gamma z)+b\sinh(\gamma z) \text{ and } A(z)=c\cosh(\gamma z)+d\sinh(\gamma z). \quad (4.11)$$

Using the boundary conditions

$$\begin{aligned} B(0) &= a \\ B(L) &= a\cosh(\gamma L) + b\sinh(\gamma L) \\ A(0) &= c \\ A(L) &= c\cosh(\gamma L) + d\sinh(\gamma L) = 0 \end{aligned} \tag{4.12}$$

the coefficients are found to be

$$\begin{aligned} a &\equiv 1 \\ b &= -a\frac{ip + \gamma\tanh(\gamma L)}{\gamma + ip\tanh(\gamma L)} \\ c &= -\frac{1}{i\kappa}(ipa + \gamma b) \\ d &= -\frac{c}{\tanh(\gamma L)} \end{aligned}$$

where the following substitutions have been made:

$$\begin{aligned} \kappa &\equiv \frac{k_0 \Delta n}{2} \\ p &\equiv n_0 k_0 \left(\frac{\Delta k}{k_0} + \sigma - \frac{d\phi}{dz} \right) \end{aligned} \tag{4.13}$$

The coefficients of transmission and reflection are

$$\begin{aligned} r &\equiv \frac{A(0)}{B(0)} = \frac{c}{a} \\ t &\equiv \frac{B(L)}{B(0)} = a\cosh(\gamma L) + \frac{b}{a}\sinh(\gamma L) \end{aligned} \tag{4.14}$$

This analysis was done in the absence of loss, and by the conservation of power, the transmission and reflectivity add to 1,

$$R + T = |B|^2 + |A|^2 = 1 \tag{4.15}$$

Uniform gratings are characterized in large part by the term κL, a measure of the strength. However, two gratings with the same κL but different lengths will have the same absolute reflectivity $R_{max} = \mathrm{abs}(r(\Delta k = 0))^2 = \tanh(\gamma L)$, but the longer grating and consequently lower Δn will have a narrower bandwidth. Figure 4.2 shows the grating parameters used for modeling three gratings with κL=1, 3, 5. The Bragg wavelength is designed at 1540 nm, which corresponds to 0 frequency offset. At this wavelength each .1 nm corresponds to 12.64 GHz by the relation

$$\frac{\Delta\lambda}{\lambda} = \frac{\Delta\nu}{\nu} \Rightarrow \Delta\nu = \frac{\lambda^2}{c}\Delta\lambda \tag{4.16}$$

Figure 4.3 is a schematic of the typical index of refraction in the core of the fiber. The grating period has been reduced by a factor of ~630 to exaggerate the effect, and the dark line across the center indicated the average index. The index is raised where the fiber is exposed. Figure 4.4 shows the spectral transmission for the modeled gratings, and Figure 4.5 shows the phase of the transmissions, normalized to the propagation of the field without a grating present.

Length, L	1 cm	
Index of refraction, n_0	1.45	
Index step of grating, Δn	4.0×10^{-5}	$\kappa L = 0.8$
	1.0×10^{-4}	$\kappa L = 2.0$
	2.5×10^{-4}	$\kappa L = 5.1$

Figure 4.2. Table of parameters used for uniform grating simulation.

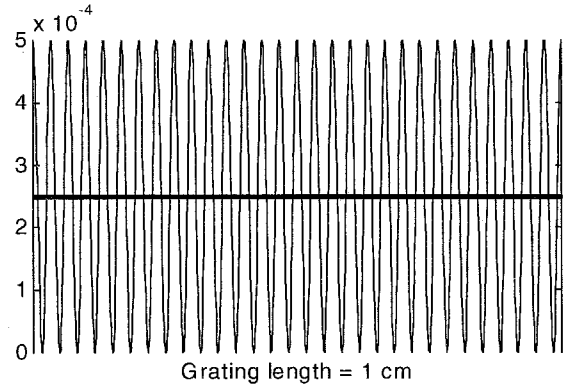

Figure 4.3. Graphical representation of a typical fiber Bragg grating.

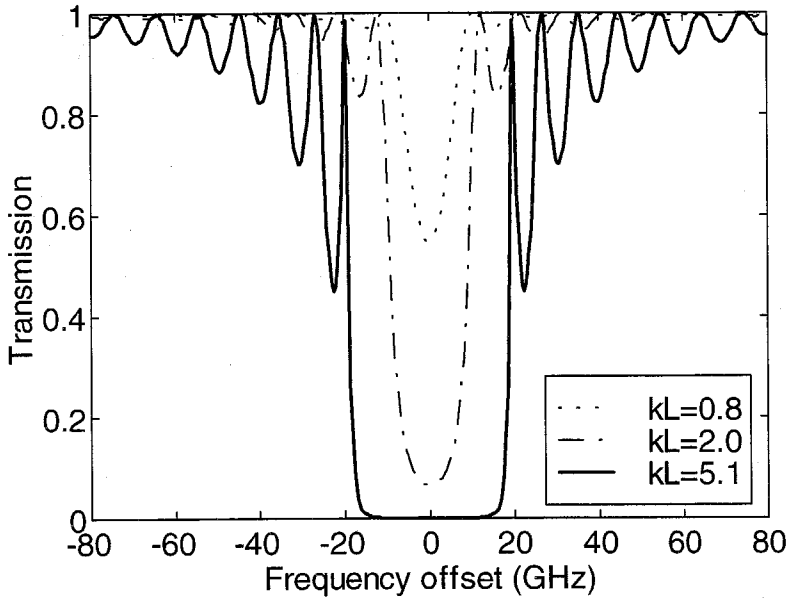

Figure 4.4. Transmission vs. frequency for three uniform gratings.

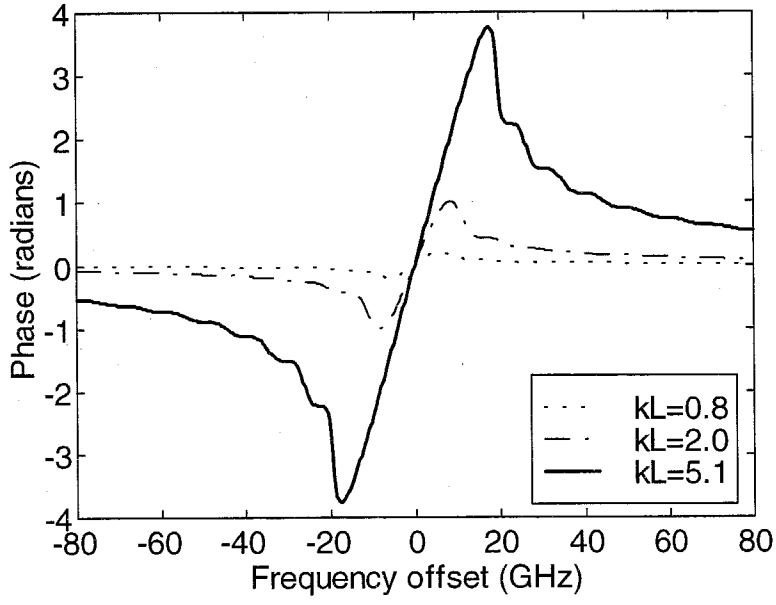

Figure 4.5. Transmission Phase vs. frequency offset for the same gratings.

By expanding the phase of the reflected field around the Bragg wavelength, the time delay of the reflected field is given by the delay

$$\tau = -\frac{d\phi}{d\omega} = \frac{\lambda_B^2}{2\pi c}\frac{d\phi}{d\lambda} \tag{4.17}$$

for our time convention [4–7]. The time delays for the modeled gratings are shown in Figure 4.6.

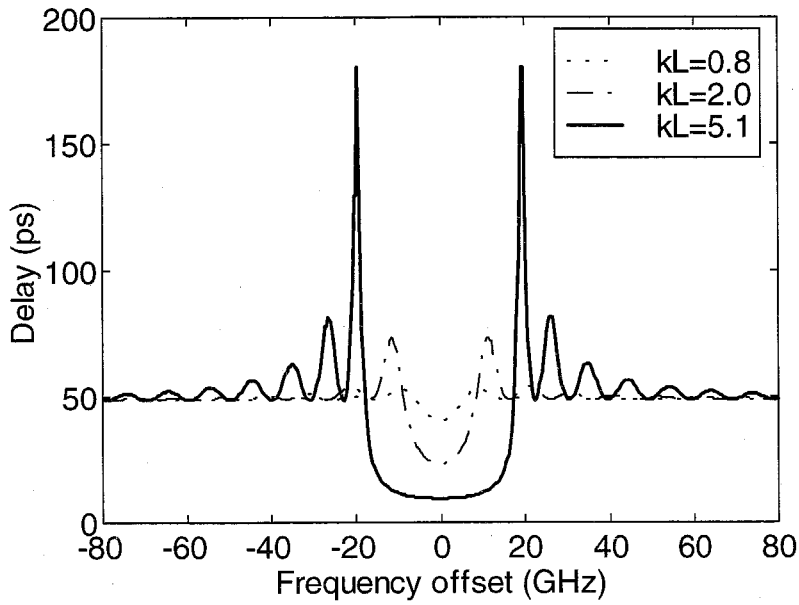

Figure 4.6. Time delay for reflected field from a uniform grating.

Note the background (i.e., far from the Bragg condition) delay is the same for all the grating strengths. This is because they are each 1 cm. A longer grating will have a longer delay by the same proportion. Since the interaction is weak for these wavelengths, it can be assumed that there are equal powers reflected from each fringe which are neither

constructive nor destructive with each other, resulting in an overall delay of a wave reflected at the midpoint of the grating.

4.3. Numerical Predictions

Solving the coupled mode equations (4.8) numerically allows us the freedom to simulate arbitrary apodizations and chirps. Apodization refers to a z-dependent Δn, typically stronger in the center of the grating and tapering off near the ends. Recall σ is the average background and $\frac{d\phi}{dz} = f(z)$ is the change in the grating pitch (chirp) along the grating. Effectively, chirp is introduced by giving α in (4.9) z-dependence. Figure 4.7 shows a Gaussian apodized grating obtained when the writing beam is Gaussian apodized.

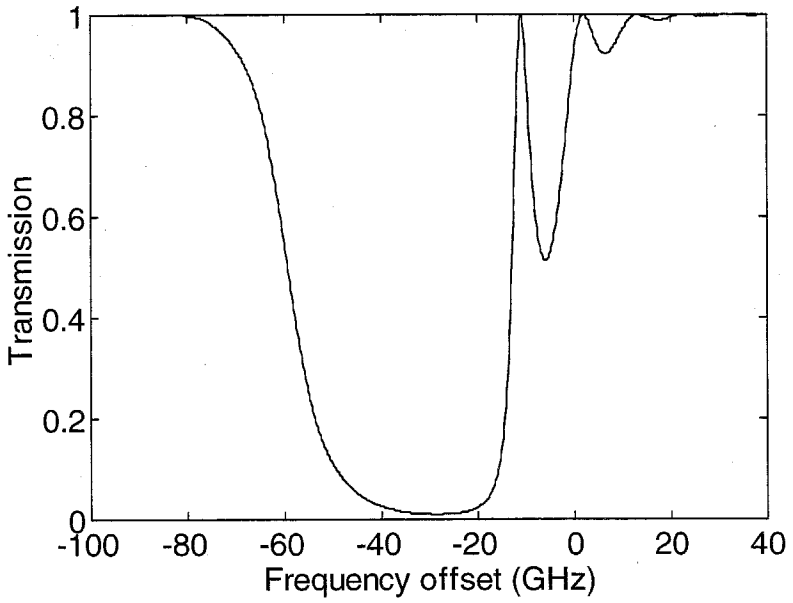

(a)

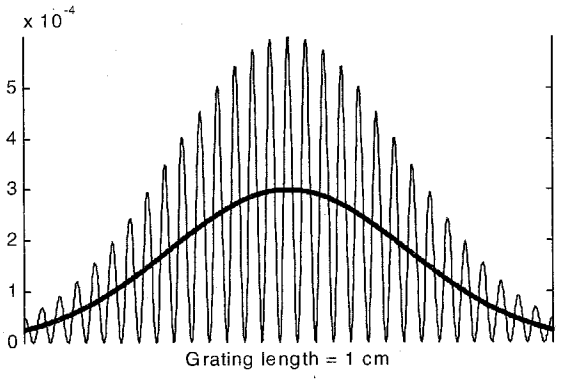

(b)

Figure 4.7. (a) Gaussian apodized grating transmission; (b) index profile.

The asymmetry in the side lobes can be eliminated by keeping the average constant and only apodizing the strength of the grating (Δn). Figure 4.8 shows the effect of this "pure" apodized grating.

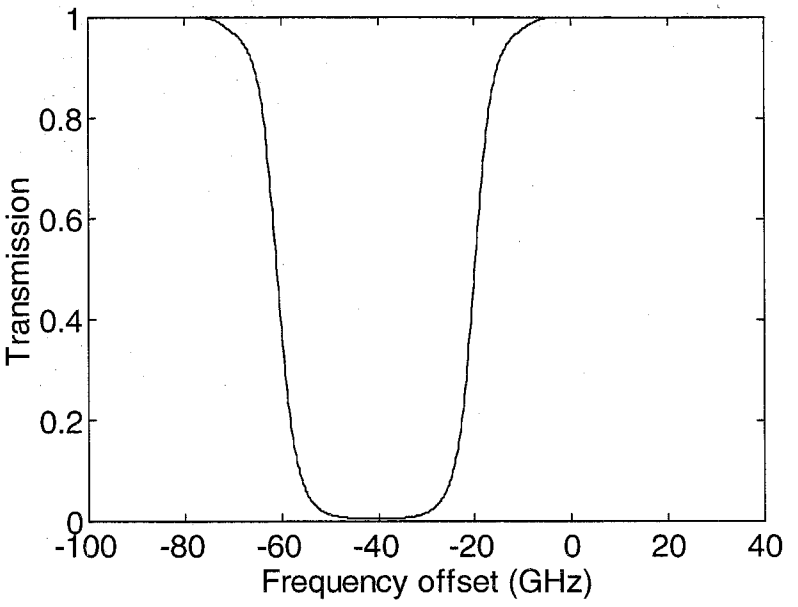

(a)

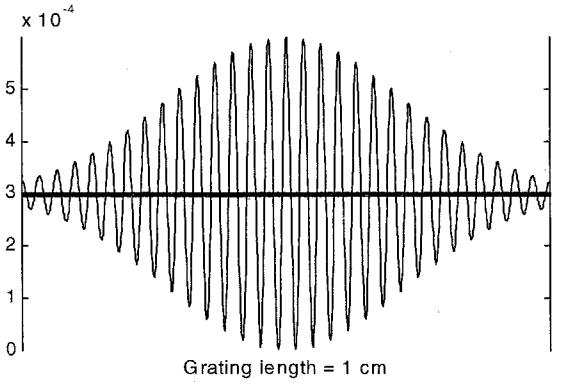

(b)

Figure 4.8. (a) "Pure" Gaussian apodized grating transmission; (b) index.

By apodizing the grating, the 50% reflection bandwidth will increase slightly compared to the uniform grating of total integrated coupling strength,

$$\kappa L = \int_0^L \kappa(z)dz\,, \tag{4.18}$$

but will have lower sidelobes.

Chirp is another useful control over the reflection properties of a grating. Chirp is characterized by a change in the local Bragg wavelength along the grating, which has the effect of increasing the bandwidth of the grating. A constant chirp can be modeled either as a linear increase in the background index or a squared term in the phase ϕ. In the coupled mode equations (4.8), substitute the following z-dependent phase shift of the grating:

$$-\frac{d\phi}{dz} = b\frac{z}{L_g} \tag{4.19}$$

where b is measured in units of μm^{-1}. The reflectivity results for three different values of linear chirp, b, are shown in Figure 4.9. By giving each grating the same average index of 0, the midpoints of each grating have the same local Bragg wavelength.

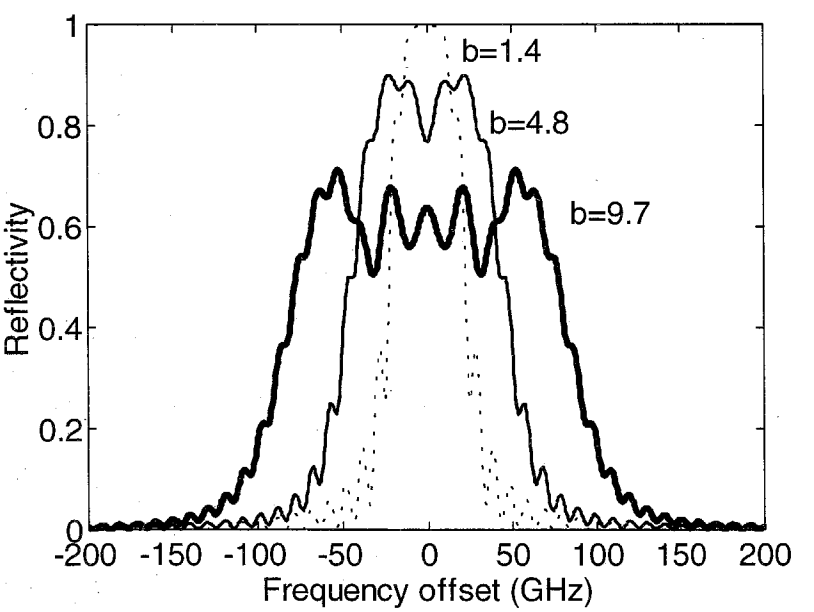

Figure 4.9. Reflectivity for three different values of linear chirp.

By combining apodization and chirp, it is possible to obtain a grating which has a wide, smooth-top reflection profile. Figure 4.10 shows the simulation results for a linearly chirped grating (b = 14 μm^{-1}) and a Gaussian apodization, the same as that used in Figure 4.8. The total integrated κL is 5.6.

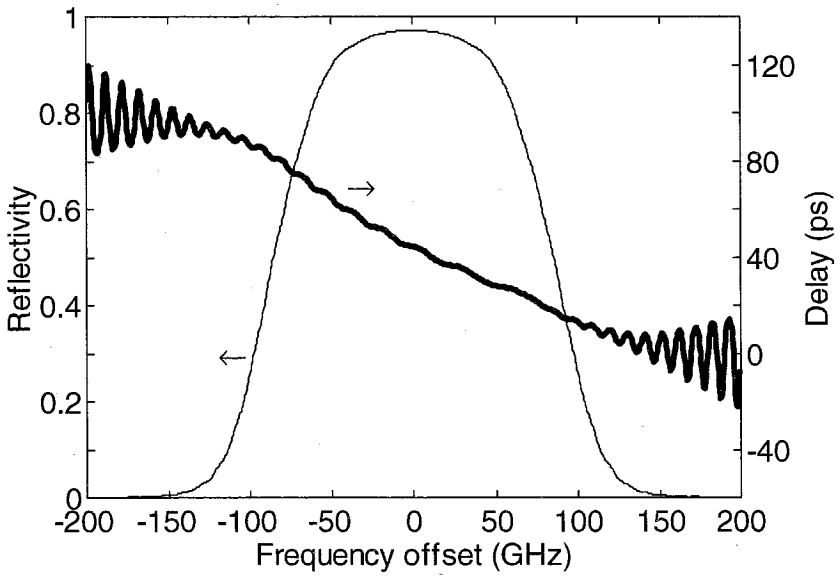

Figure 4.10. Reflection and Delay for an apodized, chirped grating.

4.4. Fabrication Method

4.4.1. UV Sensitivity

The first fiber Bragg gratings were reported in 1978 by Hill et al. [4–8], [4–9] when it was discovered that germanium-doped (Ge) fiber was sensitive to UV radiation. Once

uniform fiber Bragg gratings were demonstrated with consistent reproducibility, the focus of grating research branched out into engineering the gratings for certain applications.

The study of the chemical nature of the photosensitivity remains active. There are several explanations for the index change of germanium-doped fiber upon exposure to UV radiation, but no single explanation is universally accepted. Current belief is that impurities in the silica, such as Ge, have absorption sites that become altered by absorption of UV photons. Electrons are freed and recaptured in other locations in the amorphous silica, physically altering the material [4–10], [4–11], [4–12]. These absorption changes, called photobleaching, are manifestations of a change in the complex susceptibility, and it can be shown by the Kramers-Kronig relations that this can cause a change in the background index of refraction at wavelengths far away from the absorption, such as 1550 nm [4–13]. This case was observed when a KrF excimer laser operating at 248 nm was used to expose fluorine-doped glass. BGG31 glass, used for fabricating ion-exchanged waveguides, can also be used for making fiber Bragg gratings at Bragg wavelengths around 1540 nm [4–14]. Three-dimensionally written gratings are evidence that neither germanium nor hydrogen need be present to produce a reasonable index change with 248 nm irradiation. Index changes of $\sim 4 \times 10^{-5}$ were deduced. The effect of the excimer exposure on the transmission of the glass can be seen in Figure 4.11. Shown is the transmission as a function of wavelength with and without exposure (no grating) and compared to a standard Corning glass microscope slide. The microscope slide transmission curve was unaffected by the excimer laser. Photobleaching the BGG31

glass with 248 nm radiation changes the absorption spectrum near 350 nm and appears to add a new absorption band near 520 nm, with no noticeable differences above 650 nm.

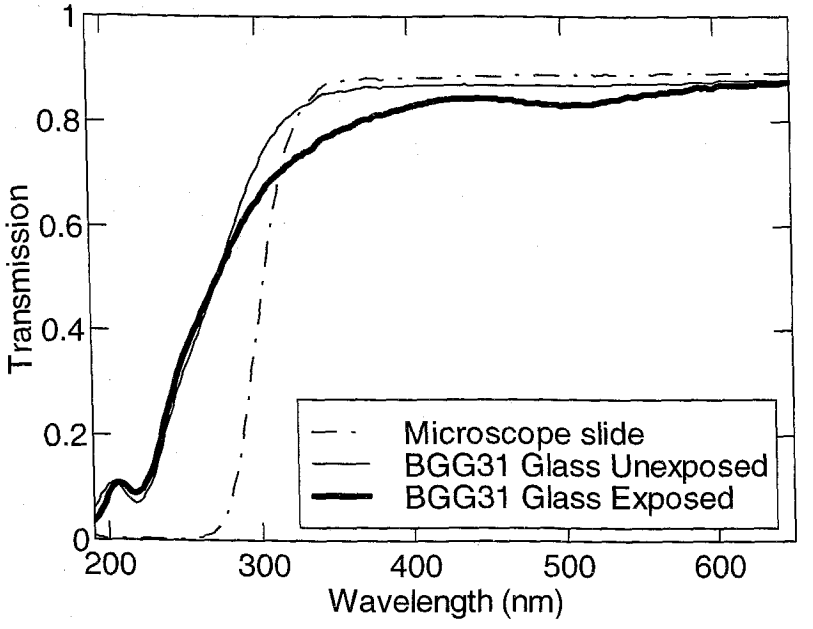

Figure 4.11. Absorption changes by UV exposure.

The microscope slide showed no evidence of index change, but BGG31 shows a new absorption site achieved, indicating an index change at 1540 nm.

Characterizations of gratings written into these ion-exchanged samples are discussed in Chapter 5. The next section describes the grating fabrication process and index profile characterization.

4.4.2. Grating Fabrication

For this thesis, a high power UV excimer laser operating at 248 nm was used to write gratings. The excimer laser achieves stimulated emission through the molecular transition of the unstable molecule KrF, excited by a pulsed 20 kV electronic discharge.

There are two main methods used to make gratings: interferometric and phase mask. In the interferometric approach, the writing beam is split and recombined to form an interference pattern at the fiber. The phase mask method requires a simpler setup and is less sensitive to mechanical vibrations. The exposure setup is shown in Figure 4.12.

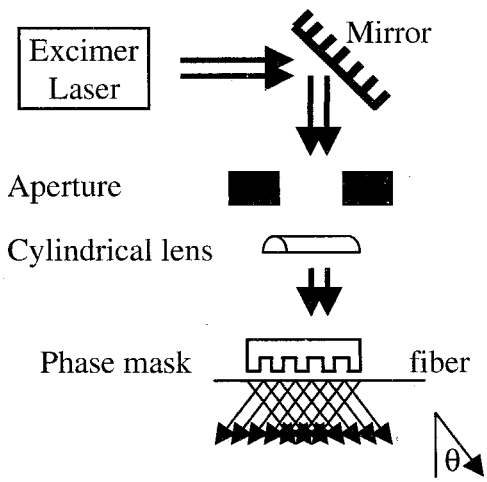

Figure 4.12. Experimental setup for grating exposure.

The 2 cm beam is reflected downward by a 45° dielectric mirror. The beam then passes through an aperture to define the length of the grating, then through a cylindrical mirror to focus the beam perpendicular to the fiber to concentrate more power at the fiber. Finally, the beam passes though the phase mask, which is in contact with the fiber.

The phase mask is designed to suppress the 0^{th} order of the beam and maximize the power in the +1 and -1 orders. This is controlled by the groove depth in the mask. The field generated by these two beams in the z-direction has the form:

$$E(z) = E_0\left(e^{i\frac{2\pi n}{\lambda} z \sin\theta} + e^{-i\frac{2\pi n}{\lambda} z \sin\theta} \right) \tag{4.20}$$

where λ = 248 nm, the diffraction from the grating and by Snell's Law: $\sin\theta = \frac{\lambda}{n\Lambda_m}$, n is the index of the fiber and Λ_m is the period of the mask. The resulting cosine intensity and similarly index change by UV exposure is

$$I(z) \propto \cos\left(\frac{4\pi z}{\Lambda_m}\right). \tag{4.21}$$

By comparing with (4.1), and $k_0 = \frac{2\pi}{\lambda_B}$,

$$\lambda_B = n\Lambda_m \tag{4.22}$$

Using this setup, the growth rate of the grating was monitored. Figure 4.13 shows the transmission dependence at the Bragg wavelength as a function of grating exposure time. The points are data and the line is a linear fit to the data.

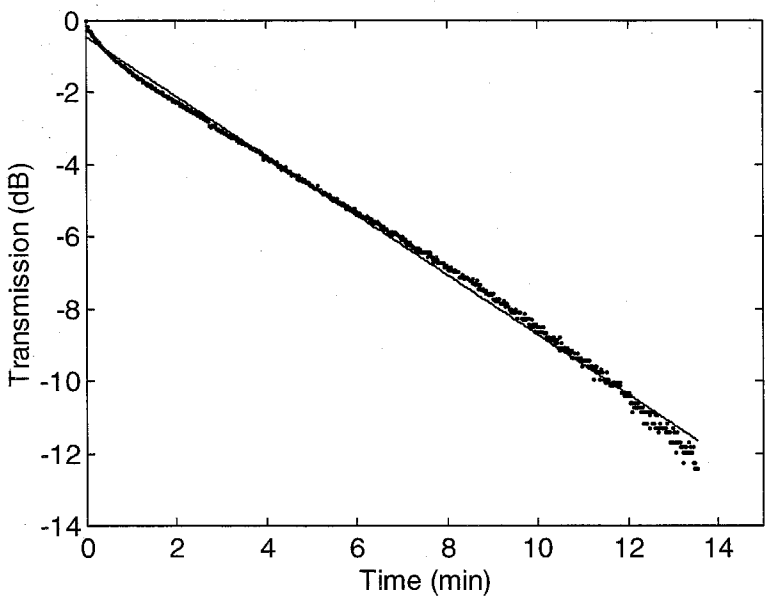

Figure 4.13. Grating strength as a function of exposure time.

Using the uniform grating equations (4.14), the time dependence of Δn was extracted and plotted in Figure 4.14. After an initial transient quick growth, Δn seems to grow linearly with exposure time.

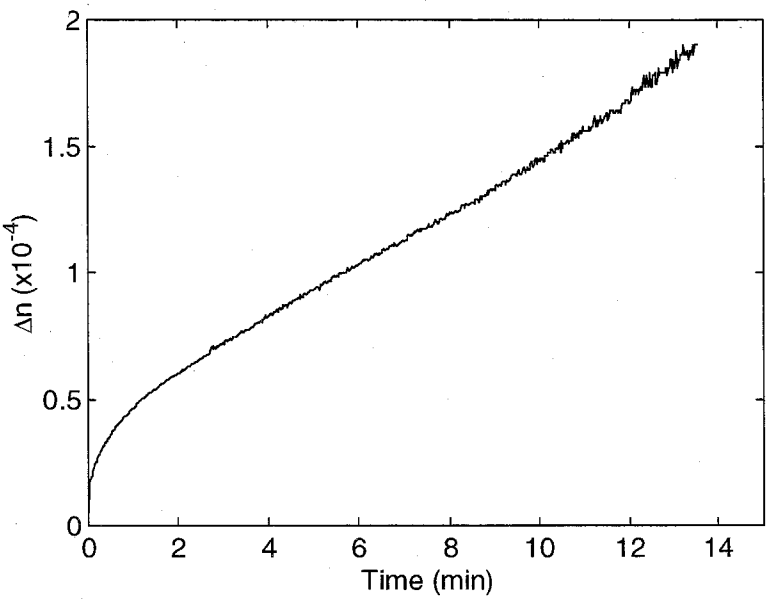

Figure 4.14. Δn dependence on exposure time.

Later work involved modifying the grating setup to write more uniform gratings. Instead of the entire 2 cm beam used for exposure, only 1 mm was used and scanned along the length of the grating, shown in Figure 4.15.

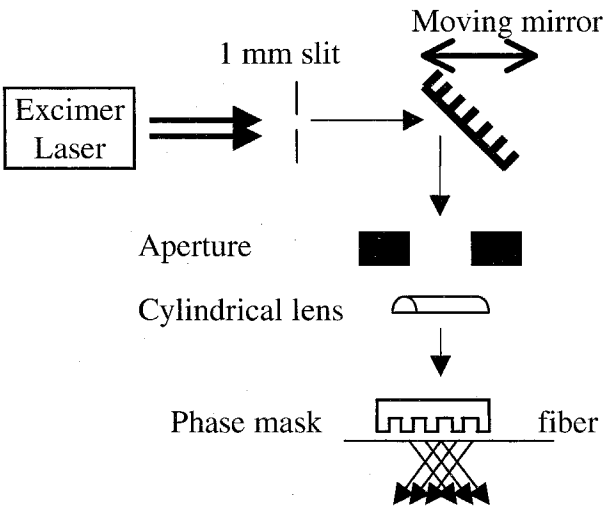

Figure 4.15. Improved setup for more uniform gratings.

By using the same beam strength for the entire grating, much more uniform exposures were realized. Also, monitoring the growth was easier because the fiber was heated less rapidly allowing characterizing and controlling parameters to be reliably changed between scans. Figure 4.16 shows the transmission results obtained by writing a very uniform grating. The dotted curve is the fit for this grating. Parameters obtained were Length = 5.025 mm, $\Delta n = 4.34 \times 10^{-4}$, $n_0 = 1.45$, $\sigma = 9.97 \times 10^{-5}$ (average index offset).

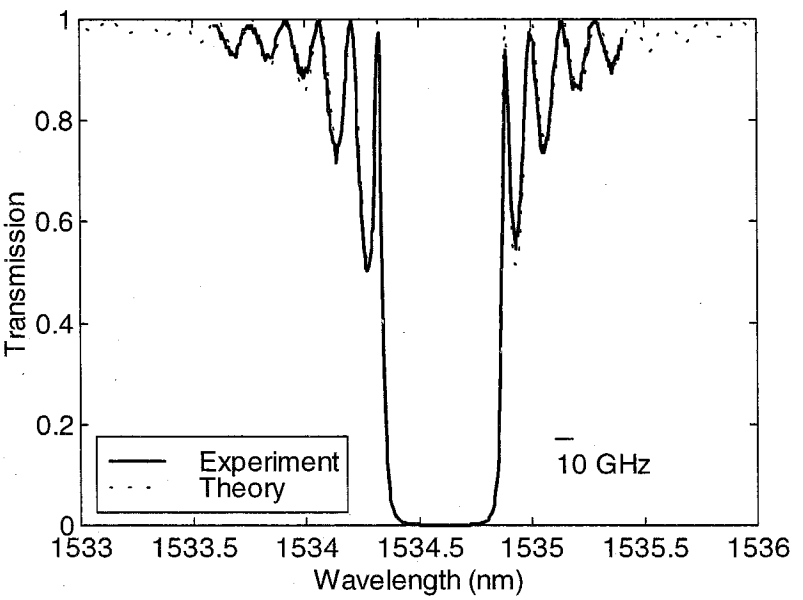

Figure 4.16. Experimentally written uniform grating with overlay theory curve.

4.5. Realization of Arbitrary Amplitude Profile (Apodization)

Beyond the theory of apodized gratings, there has been considerable work on the optimization of such gratings for optical communication bandwidth enhancement [4–7], [4–15], [4–16]. Several types of experimental methods are proposed for apodization. These methods include dithering of the phasemask, taking advantage of the coherence limitations of the writing laser, inserting an optical wedge in one of the two interference UV beams [4–17], and spatial intensity filters [4–18] which absorb radiation and are subject to damage over time. In the dither method, the writing beam is scanned along the fiber while dithering the phase mask relative to the fiber to control the fringe contrast. This way the total exposure time for each segment is constant while allowing a stronger index change near the center. Each of these methods introduces complications in the apparatus and limits repeatability.

Here a simple, inexpensive method is discussed for achieving arbitrary apodization for a fiber Bragg grating, which uses an amplitude mask to apodize the beam without absorption. This method will work well with most grating fabrication techniques, whether using interfering beams or a phasemask. Also, it does not matter whether the beam is scanned across the fiber or exposed all at once with this amplitude mask.

The amplitude mask uses dot density as a substitute for grayscale. Grayscale introduces a certain amount of absorption, and a high power excimer laser can be quite destructive on optics. By passing the beam through the binary amplitude mask, certain

parts are selectively deleted. Then the beam is focused in the direction perpendicular to the fiber so that across the fiber there is an averaging of the beam amplitude from the mask across the core of the fiber. Figure 4.17 shows the exposure setup. The first exposure is performed with the desired apodization profile mask with the phase mask in place. This exposure alone produces an apodized background index of refraction as well [4–7], thus another exposure is necessary with the reverse image with the amplitude mask and no phase mask, also shown in Figure 4.17.

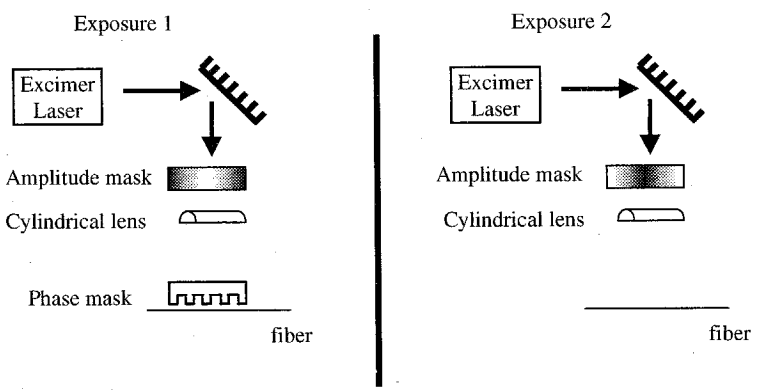

Figure 4.17. Experimental setup for the two-exposure method.

A magnified view of the mask for the first exposure is shown in Figure 4.18. For this demonstration, a Gaussian apodization profile was selected. The pattern was generated to have rows of uniform dot density in the y-direction, but each row would have a random starting position. This eliminated any preferential location on the mask. Any curve like the one show in Figure 4.18 could be made with this method by simply calculating a desired density of dots per row as a function of x and normalizing to the

maximum density. The masks were made by first evaporating aluminum on a substrate of fused silica. Aluminum was selected for its high reflectivity of 93% at our excimer wavelength of 248 nm. Next, the pattern was laser printed at a resolution of .5 mm/pixel and photo-reduced 10:1 for the exposure of a photoresist on the aluminum. The aluminum under the exposed resist was etched off, leaving a 2 cm pattern with a resolution of 50 μm/pixel.

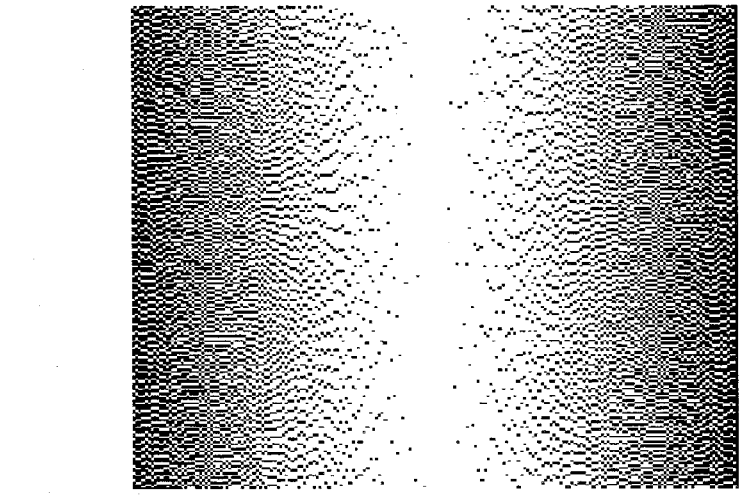

a)

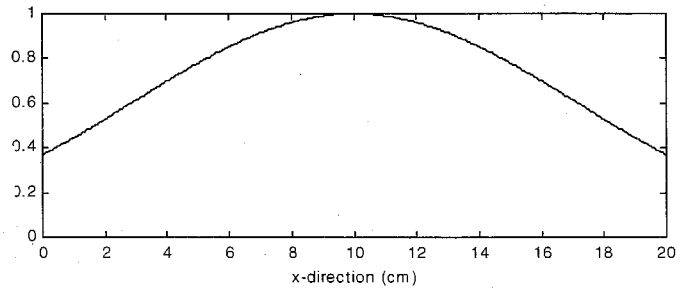

b)

Figure 4.18. Binary amplitude mask.

(a) Mask. (b) Average transmission along the mask.

The x-direction is horizontal in this figure.

The cylindrical lens reduced the pixels in the y-direction to 10 μm such that several pixels of information passed through the 125 μm cladding of the fiber, further focusing in the core, providing sufficient averaging of the y-direction of the beam. Figure 4.19 shows the beam intensity in the fiber grating direction after passing through each mask separately.

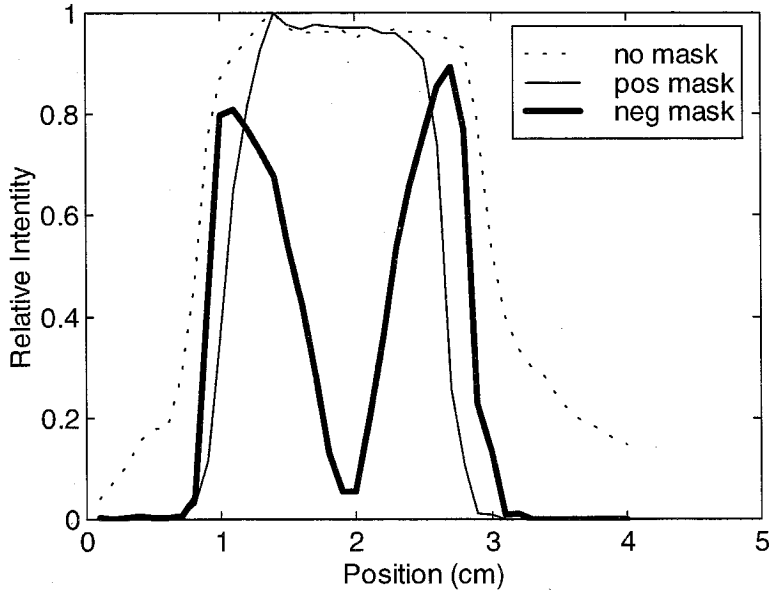

Figure 4.19. Intensity of original beam (no mask) and after passing through each of the binary masks.

The results of writing an apodized grating using this method are shown in Figure 4.20. The fiber used was hydrogen-loaded SMF28 Corning fiber. Exposure 1 was performed for 1 min with .75 J/cm^2 at 50 Hz. The large sidelobes on the short-wavelength

side of the main dip are characteristic of a Gaussian apodized grating discussed in Section 4.3. After the second exposure (same exposure parameters), the sidelobes were greatly reduced, and the Bragg wavelength increased, indicating a leveling of the background index. The departure from ideal for this strong grating (-30 dB transmission dip) is attributed to mask imperfections and slight alignment mismatch between first and second exposures, which was hard to correct in our setup because both masks were on the same substrate.

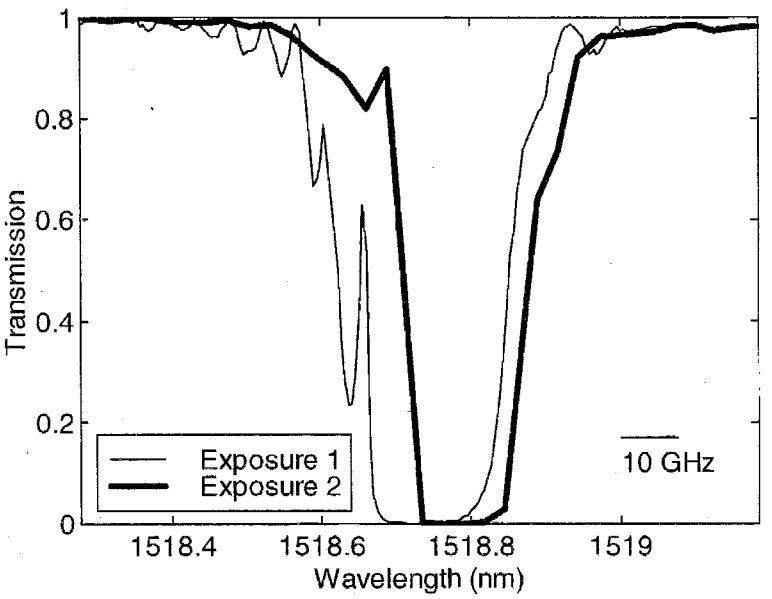

Figure 4.20. Grating transmission after each exposure.

This method can be further improved by enhancing the resolution of the mask, easily accomplished by today's lithography equipment. Also, improvements in uniformity of the writing beam can be made with the scanning beam writing method. In conclusion, this

method of writing apodized gratings can be a convenient and powerful way to meet the demand for apodized gratings, and provide flexibility in grating design.

References for Chapter 4

[4–1] C. R. Giles, "Lightwave Applications of Fiber Bragg Gratings," J. Light. Tech. 15, (8) pp. 1391-1404 (1997).

[4–2] Andreas Othonos, "Fiber Bragg Gratings," Rev. Sci. Instrum, 68, pp. 4309-4341 (1997).

[4–3] Daniel Pastor, José Capmany, Diego Ortega, Vicente Tatay, and Javier Martí, "Design of Apodized Linearly Chirped Fiber Gratings for Dispersion Compensation." J. Light. Tech. 14, (11) pp. 2581-2588 (1996).

[4–4] F. Bilodeau, D. C. Johnson, S. Theriault, B. Malo, J. Albert, and K. O. Hill, An All-Fiber Dense-Wavelength-Division Multiplexer/Demultiplexer Using Photoimprinted Bragg Gratings," Phot. Tech. Lett. 7, (4) pp. 388-390 (1995).

[4–5] A. S. Kewitsch, G. A. Rakuljic, P. A. Willems, and A. Yariv, "All-fiber zero-insertion-loss add-drop filter for wavelength-division multiplexing," Opt. Lett. 23, (2) pp. 106-108 (1998).

[4–6] J. T. Kringlebotn, J. L. Archambault, L. Reekie, and D. N. Payne, "Er^{3+}:Yb^{3+}-codoped fiber distributed-feedback laser." Opt. Lett. 19, (24) p. 2101-2103 (1994).

[4–7] Turan Erdogan, "Fiber grating spectra," J. Light. Tech. 15 p. 1227-1294 (1997).

[4–8] K. O. Hill, Y. Fujii, D. C. Johnson, and B. S. Kawasaki. Appl. Phys. Lett. 32, p. 647 (1978).

[4–9] B. S. Kawasaki, K. O. Hill, D. C. Johnson, and Y. Fujii. Opt. Lett. 3, p. 66 (1978).

[4–10] D. L. Williams, S. T. Davey, R. Kashyap, J. R. Armitage, and B. J. Ainslie, "Direct observation of UV induced bleaching of 40 nm absorption band in photosensitive germanosilicate glass fibre," Elect. Lett. 28, pp. 369-371 (1992).

[4–11] J. Nishii, "Permanent index changes in Ge-SiO2 glasses by excimer laser irradiation," Mat Sci Eng B-Solid. 54, 1 (June 12, 1998).

[4–12] Y. Miyake, H. Nishikawa, and E. Watanabe. Changes in the optical properties of Ge-doped silica glass during exposure to a KrF excimer laser J. Non-cryst. Solids. 222, 266-271 (1997).

[4–13] A. Yariv, *Optical Electronics in Modern Communications, Fifth Edition*, Appendix A. Oxford University Press, Inc. (1997).

[4–14] Dan Provenzano, W. K. Marshall, D. F. Geraghty, S. Honkanen, N. Peyghambarian, and Amnon Yariv, "Grating formation in BGG31 glass by UV exposure," Elect. Lett. 35 (16) 1332-1334 (1999).

[4–15] K. Hinton, "Dispersion compensation using apodized Bragg fiber gratings in transmission," J. Light. Tech. 16 p. 2336-2346 (1998).

[4–16] K. Ennser, M. N. Zervas, and R. I. Laming, "Optimization of apodized linearly chirped fiber gratings for optical communications," IEEE J Quant. Elec. 34: (5) p. 770-778 (1998).

[4–17] Hans-Georg Frohlich and Raman Kashyap, "Two methods of apodisation of fibre Bragg gratings," Opt. Comm. 157 p. 273-281 (1998).

[4–18] Harmeet Singh and Mark Zippin, "Apodized fiber Bragg gratings for DWDM applications using uniform phase mask," ECOC'98 Conf. Proc. p. 189-190 (1998).

Chapter 5 - Applications of Fiber Bragg Gratings

5.1. Introduction

Today's commercial optical communications uses for FBG's include bandwidth filtering, add/drop channel control for wavelength division multiplexing, and laser frequency stabilization. These powerful, all-fiber devices can now be the building blocks for the new devices proposed here to help drive the technology for this fast-paced growing industry. The rest of this chapter is devoted to projects developed with fiber Bragg gratings and telecommunications applications are discussed.

5.1.1. Temperature Dependence of Fiber Bragg Gratings

Due to their inherent sensitivity to temperature and stress, FBG's are used as sensors for these environmental factors. Typically for telecom applications, these sensitivities are minimized as much as possible. With temperature, the largest effect on the Bragg wavelength is the thermo-optic coefficient [5–1]

$$\frac{\Delta n}{\Delta T} = 7 \times 10^{-6}. \qquad (5.1)$$

The thermal expansion coefficient has a much smaller effect:

$$\frac{\Delta L}{L\Delta T} = 5\times10^{-7}. \tag{5.2}$$

The combined effect is a Bragg wavelength sensitivity of .01 nm/°C (1.2 GHz/°C) and the measurement is shown in Figure 5.1 with the linear fit.

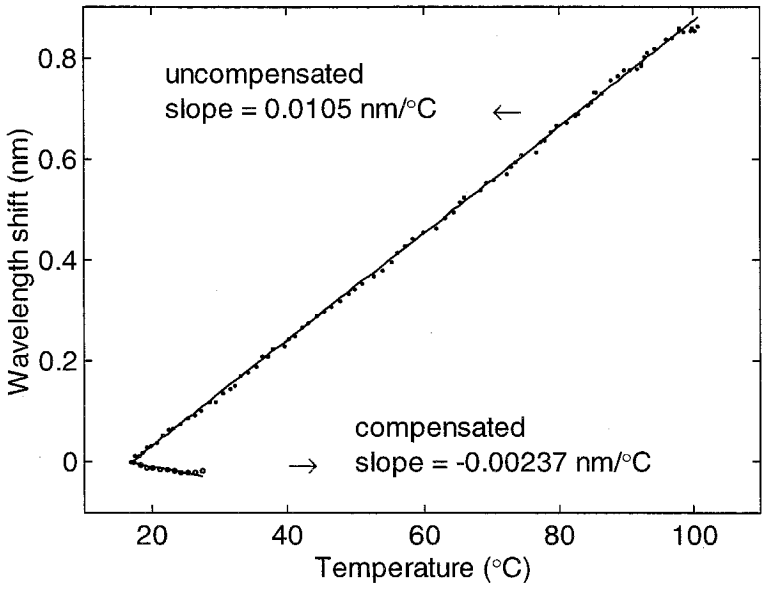

Figure 5.1. Temperature dependence of a fiber Bragg grating.

Passive compensation techniques have been able to reduce this shift down to .1 GHz/°C [5–1]. Also shown in the figure is the Bragg wavelength shift for a grating that was prestretched and glued to a sample of NEX-I material from Ohara Inc., a new glass ceramic, with a thermal expansion of -8×10^{-6}. It can be seen that over a small temperature range around room temperature, there is a slight overcompensation in the Bragg wavelength shift. Outside this range, data was not consistent, possibly due to temperature

gradients chirping the grating or the nonlinear effect of the thermal expansion expressing itself. However, for a device stabilized to near room temperature, this material is a quite promising method of reducing the temperature dependence of fiber Bragg gratings.

For some non-telecomm applications, this uncompensated linear dependence as well as stress dependence of the Bragg wavelength are exploited and used as temperature sensors.

5.2. Signal Modulation Enhancement

Propagation of a directly modulated semiconductor laser signal through dispersive optical fiber changes the modulation response of the laser-fiber system [5–2]. The change in the amplitude modulated (AM) signal results from a large residual frequency modulation (FM), attendant on the AM, being converted into AM and vice versa by dispersive propagation, as discussed in Chapter 3. Eggleton et al. [5–3] demonstrated dispersion compensation with an unchirped fiber Bragg grating in transmission. Here it is shown that a fiber grating can convert laser FM into AM in transmission to increase the magnitude of the AM signal. When combined with a dispersive fiber, the grating increases the signal, flattens the frequency response, and increases the system bandwidth, providing a frequency-domain demonstration of dispersion compensation in transmission through an unchirped grating. This work presents a frequency-domain analysis of the laser signal, the

dispersive fiber, and the fiber grating which accurately predicts the observed results [5–4].

The experiment consisted of using a network analyzer to directly modulate the current of a 1.54 μm commercial (ORTEL Corp.) distributed feedback semiconductor laser at frequencies up to 25 GHz, with the output sent through an optical isolator and coupled into a fiber pigtail, shown in Figure 5.2.

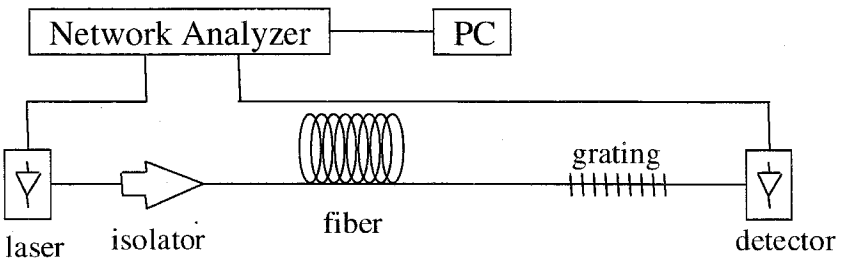

Figure 5.2. Experimental setup measuring system modulation response.

After propagation through various lengths of single-mode non-dispersion-shifted fiber and/or an unchirped fiber grating, the signal was detected with a high-speed photodiode and returned to the electronic network analyzer. By comparing the system response to that of the stand-alone laser, it was possible to determine the change in the response due solely to the fiber and/or the grating. Figure 5.3 shows the laser wavelength temperature-tuned and stabilized on the short-wavelength side of the grating reflection band, and below it is the calculated transmission phase.

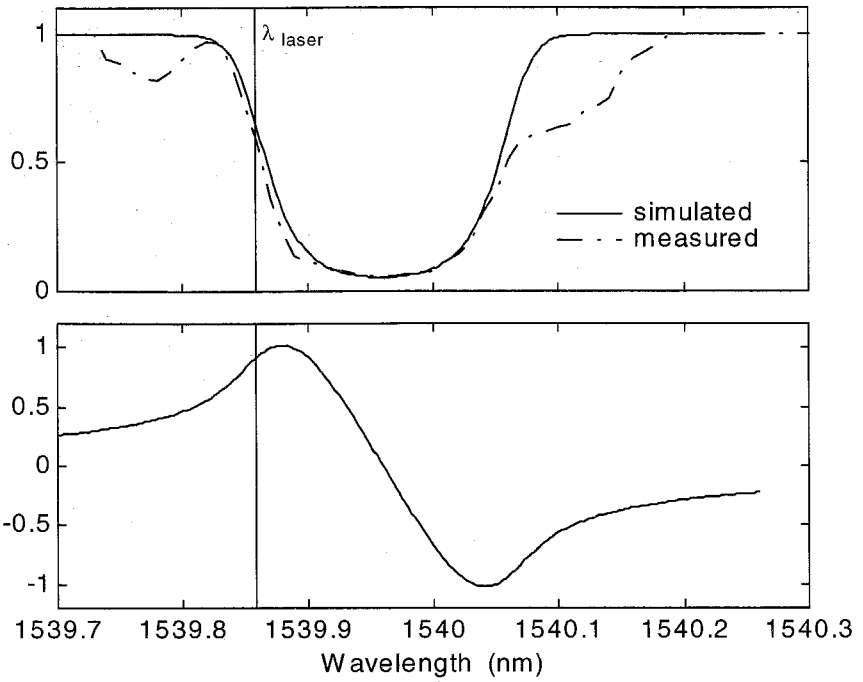

Figure 5.3. Laser tuning for the grating used in the modulation response experiments.

Since the phase of the optical field transmitted by the grating is not a quadratic function of the optical frequency over the bandwidth of the signal, we cannot model it with a single effective dispersion value [5–7]. Furthermore, the treatment of the grating as a frequency discriminator is only valid when the grating bandwidth is much larger than the optical bandwidth. The bandwidth of the grating, less than 2 Å full-width at half-maximum (FWHM), is smaller than the signal bandwidth at 25 GHz, thus requiring a more exact analysis.

We express the optical field envelope exiting the laser as

$$E_{in}(t) = E_0\sqrt{1+m\sin(\Omega t)}\exp\left[-i\beta\cos(\Omega t+\theta_{FM})\right] \tag{5.3}$$

where $m \cong .05$ is the AM modulation index, β is the phase modulation index, Ω is the modulation frequency, and θ_{FM} is the phase by which the laser FM leads the AM. As derived in Chapter 3, a directly modulated laser with a linewidth enhancement factor α, has

$$\beta = \frac{|\alpha|}{2}m\sqrt{1+\left(\kappa/\Omega\right)^2} \tag{5.4}$$

and

$$\theta_{FM} = \tan^{-1}\left(\Omega/\kappa\right) \tag{5.5}$$

Here $\kappa = \varepsilon P_0 / \tau_{ph}$ is the characteristic frequency separating the adiabatic and transient chirp regimes, where ε is the non-linear gain compression factor, P_0 is the steady-state photon density in the active region, and τ_{ph} is the photon lifetime [5–8]. κ and α were determined by fitting modulation response data for fiber propagation to the AM transfer function for dispersive fiber, following [5–9] [5–10]. We obtained $|\alpha| = 4.1$ and $\kappa / 2\pi =$ 8.5 GHz at the laser operating conditions used in the experiment. Knowing these, we used (5.3) to numerically calculate the Fourier transform $\tilde{E}_{in}(\omega)$. The output optical field from the fiber and grating combination is taken as

$$\tilde{E}_{out}(\omega) = \tilde{E}_{in}(\omega)\, t(\omega)\exp\left[-i\beta''(\omega-\omega_0)^2 L/2\right] \tag{5.6}$$

where $t(\omega)$ is the complex field transmission function of the grating, $\beta'' = \partial^2\beta/\partial\omega^2\Big|_{\omega_0}$ is the fiber dispersion parameter, ω_0 is the center optical frequency, and L is the fiber length.

The detected current $I_{out}(t)$ is obtained from $E_{out}(t)$, the inverse Fourier transform of (5.6). The AM system transfer function measured in the figures is the component of the ratio of the output to input signals at the modulation frequency,

$$H_{AM}(\Omega) = \left| \tilde{I}_{out}(\Omega) / \tilde{I}_{in}(\Omega) \right|^2 \tag{5.7}$$

A crucial step in the above calculation is the model of the fiber grating used to generate $t(\omega)$. One method is to numerically solve the coupled-mode differential equations [5–11] for a uniform grating pitch with a Gaussian apodized coupling strength profile chosen to produce the same maximum reflectivity (94.5%) and FWHM (1.9 Å) as the measured grating. The result is shown in the following figures (solid lines of Figure 5.4, Figure 5.5, and Figure 5.6). We see an increase in the AM signal due to the grating (Figure 5.4), with the same qualitative shape seen experimentally. For 25 or 50 km of dispersive fiber, we again see a prediction consistent with experiment, with a larger and flatter system response, and a higher frequency at which the first dip occurs.

An alternative model for the grating is to use the measured grating transmission spectrum, with the phase of the transmittance being inferred from its amplitude. Because $\ln(t(\omega))=\ln|t(\omega)| + i\,\phi_t(\omega)$ is square integrable, a Kramers-Kronig integral of the measured spectrum of $\ln(\sqrt{T})$ will give us ϕ_t at any optical frequency [5–12]. This numerical transform is consistent with coupled-mode solutions for uniform, chirped, or apodized gratings. The transmission spectrum of our grating was measured at 0.1 Å increments, showing an asymmetric spectrum with sidelobes on either side of the central peak. The corresponding phase spectrum was then generated numerically, and $t(\omega)$ values were

interpolated for sub-0.1-Angstrom values. The prediction of the system response resulting from this grating model (dashed lines in the figures) was more accurate than that of the coupled-mode equations.

The use of the complex grating transmission function is crucial in modeling optical signals with bandwidths comparable to or larger than that of the grating. In our calculations, modulation frequencies larger than 5 GHz could no longer be treated with the magnitude of $t(\omega)$ alone, which is equivalent to a simple frequency discriminator. Failure to include the phase of $t(\omega)$ results in over an order of magnitude error at high modulation frequencies. The dips in the system response caused by the fiber are due solely to the dispersion parameter β'' and are shifted to higher frequencies solely by the phase of the grating transmittance.

Transmission through the fiber grating alone increased the laser modulation response by between 3.5 dB and 7.5 dB at all frequencies from 0 to 25 GHz, shown in Figure 5.4.

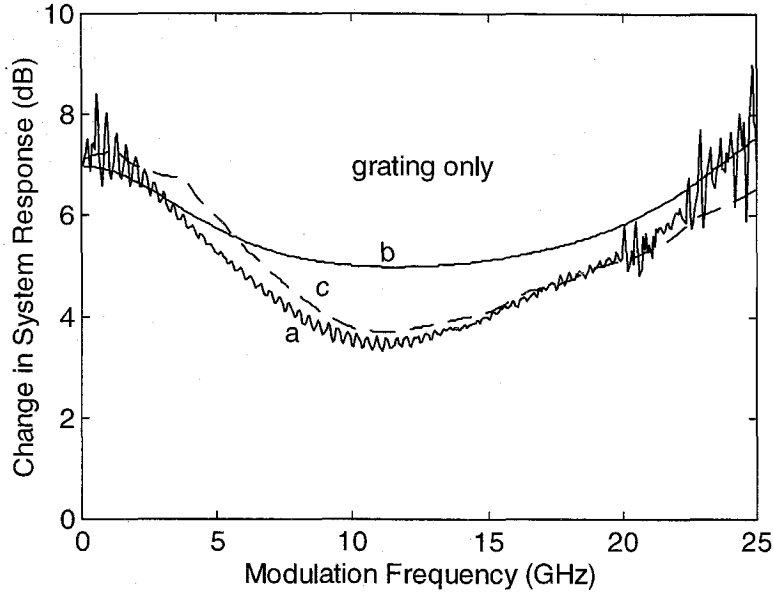

Figure 5.4. Change in system AM response due to the fiber grating. (a) Experimental data. (b) Numerical simulation using coupled-mode equations to model the grating. (c) Numerical simulation using the measured grating transmission spectrum, with the phase of the transmittance being calculated with a Kramers-Kronig integral.

The optical intensity transmission of the grating was 46% at this wavelength, so that the RF signal increase took place in spite of a drop of 54% in the average received optical power. When the laser output was sent through 25 km of fiber alone as shown in Figure 5.5a, the AM system response was increased at some frequencies, and decreased at others, a consequence of fiber dispersion, as anticipated by the exponential in (5.6).

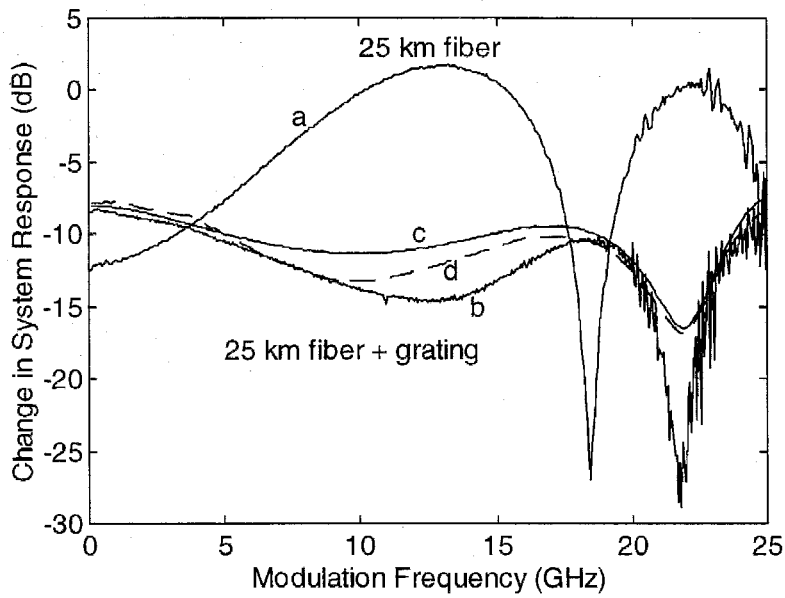

Figure 5.5. Change in system AM response with 25 km of dispersive fiber. (a) Experimental data for fiber only. (b) Experimental data for fiber and grating. (c) Numerical simulation with coupled-mode equations. (d) Numerical simulation with Kramers-Kronig integral.

The addition of the grating at the end of the fiber produced an increased signal at low frequencies and a markedly flatter response (Figure 5.5b). The system bandwidth was effectively increased too, as the first dip in the system response was pushed out from 18 GHz to near 22 GHz by the grating. Similar results also occurred with 50 km of fiber (Figure 5.6). The small amplitude oscillations in Figure 5.4a. were attributed to reflections between the fiber grating and the laser isolator. When the grating in Figure 5.5

and Figure 5.6b. was placed ahead of the fiber rather than at its end, the oscillations likewise appeared, but the response was otherwise unchanged.

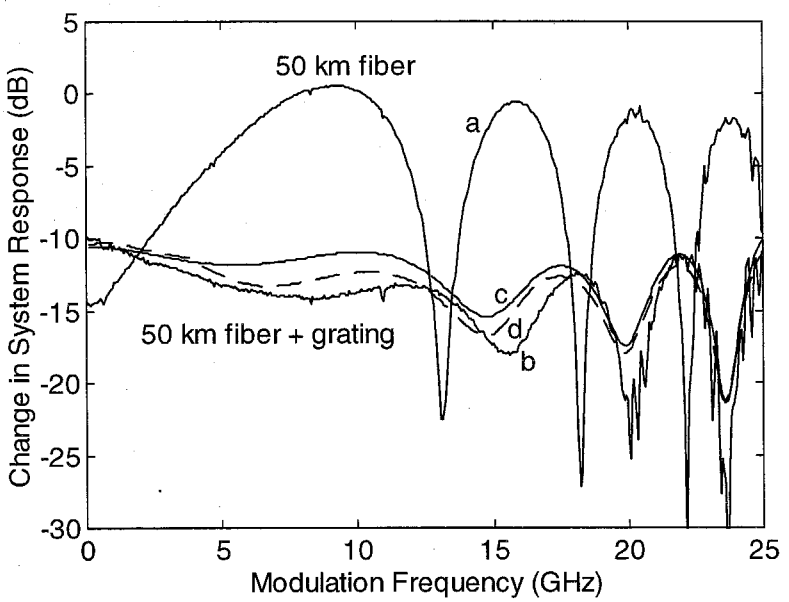

Figure 5.6. Change in system AM response with 50 km of dispersive fiber. (a) Experimental data with fiber only. (b) Experimental data with fiber and grating. (c) Numerical simulation with coupled-mode equations. (d) Numerical simulation with Kramers-Kronig integral.

Intuitively, the observed changes in the system response are the result of a combination of phenomena. The increase in the AM signal shown in Figure 5.4 can be understood by FM-to-AM conversion in the grating. In a directly modulated semiconductor laser, a frequency modulation (chirp) inevitably accompanies the amplitude modulation [5–5]. Any frequency discriminator, such as an optical filter or

resonant cavity, will result in an amplitude modulated signal correlated with the frequency modulation. Using the slope of the grating transmission versus wavelength, and the known magnitude of the frequency chirp, it is possible to predict an increase in the AM response of about 7 dB at low frequencies. Secondly, the dips in the AM transfer function of the fiber, measured in Figure 5.5 and Figure 5.6a, are due to fiber dispersion and occur at modulation frequencies that depend on the fiber dispersion-length product DL. The fact that the use of a grating pushes these dips to higher frequencies in Figure 5.5 and Figure 5.6b is an indication of partial dispersion compensation by the grating. Finally, the decrease in the magnitude of the dips is a result of the partial optical filtering by the grating of the longer-wavelength sideband [5–6], an effect which will also convert FM to AM and increase the AM response.

The AM system response was found to depend strongly on the detuning of the optical frequency from the grating center frequency. When the laser was temperature-tuned by only 10% of the grating FWHM, the change in the system response could be made to increase or decrease monotonically with modulation frequency or be negative. Likewise, the dips in the system response could be increased or decreased in magnitude and in the frequencies at which they occurred. In general, the system response changes were found experimentally and numerically to be larger for gratings with smaller bandwidths and larger reflectivities.

To be useful in optical communication systems, the laser wavelength must be carefully controlled, and optimized with the grating for a given length of fiber. The advantage of this system is that unchirped gratings are less expensive than chirped

gratings, and the transmission geometry avoids the need for optical circulators. Also, the signal increase in Figure 5.4 was accompanied by a decrease in the average optical power. Since shot noise is proportional to the average detector photocurrent, which was reduced by a factor of 0.46 due to the grating, the shot noise power decreased while the signal power increased. However, this does not mean that the system signal-to-noise ratio (SNR) will increase, though, because the same mechanism that converts FM into AM will also convert laser frequency noise into excess amplitude noise [5–13]. The next section analyzes the effects of transmission gratings on laser RIN.

5.3. Noise Reduction

Frequency dependence of both the transmitted amplitude (frequency discrimination) and the phase (dispersion) for fiber Bragg gratings leads to FM-to-AM conversion [5–4]. The phenomenon is similar in dispersive fiber, in which FM-to-AM conversion which mixes frequency and intensity noise, and can increase or decrease the relative intensity noise (RIN) of the laser depending on the fiber length and the laser dynamic parameters [5–13]. The effect relies on intrinsic correlations between intensity noise and frequency noise, which have been exploited to reduce laser RIN using a Michelson interferometer [5–14], [5–15].

Here we investigate the effect of transmission through a fiber grating on the relative intensity noise of semiconductor laser light. A model of the grating explains

observed increases in intensity noise of up to 30 dB at low frequencies. There also exist conditions under which a grating can reduce intensity noise, and we demonstrate 2 dB of RIN reduction at frequencies up to 15 GHz. A numerical calculation incorporating the phase of the grating transmittance correctly predicts these results.

The experimental measurements were performed by biasing a 1.54 μm commercial (ORTEL Corp.) distributed feedback (DFB) laser with a low-noise constant-current controller. The laser output was sent into a fiber pigtail and through an optical isolator (> 60 dB), through a variable optical attenuator and into a high-speed photodiode. The detected photocurrent was electronically amplified and fed to an electronic spectrum analyzer. From the experimental plots of noise power versus photocurrent we extracted the thermal noise (constant part), shot noise (linear part), and laser noise (quadratic part) at each electronic frequency. We then replaced the attenuator with a fiber grating (Figure 5.7) and compared the RIN with and without the fiber grating to determine its effect. The laser wavelength was temperature-tuned and stabilized at different parts of the grating transmission spectrum (Figure 5.8).

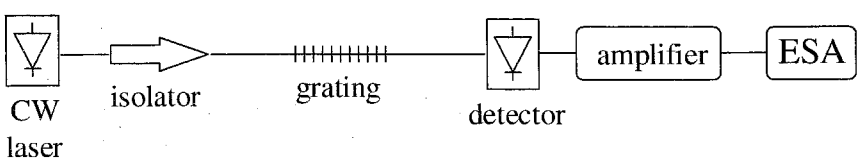

Figure 5.7. Experimental setup to measure laser RIN.

ESA: Electronic Spectrum Analyzer.

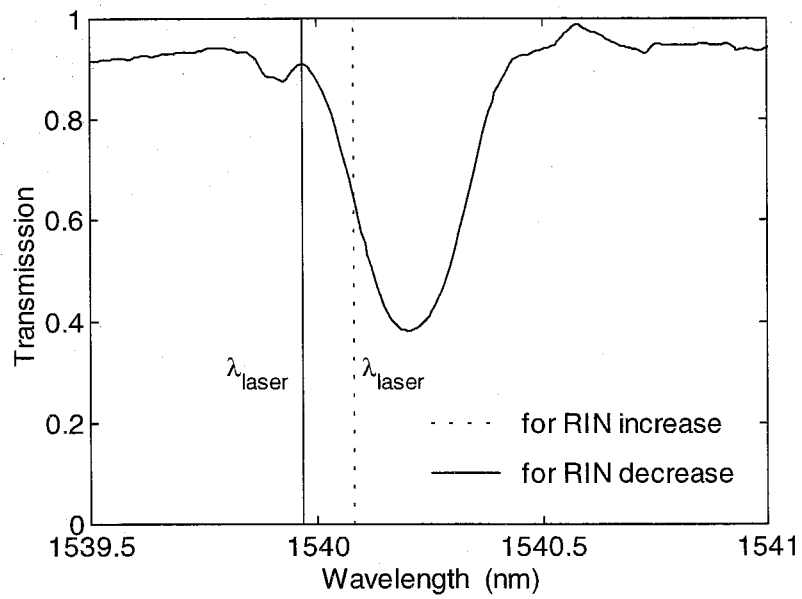

Figure 5.8. Transmission spectrum of grating used for RIN measurements with the two different laser tunings.

Figure 5.9 shows the change in RIN caused by a grating with the laser wavelength tuned to the steep linear part of the transmission spectrum on the low-wavelength edge of the reflection band (Figure 5.8). The dramatic increase in noise, over 20 dB at low frequencies, is due to the frequency discrimination of the grating, which converts laser frequency fluctuations into transmitted intensity fluctuations. If a constant optical power P_{inc} is incident on the grating with an instantaneous frequency deviation $\Delta\omega(t) = \omega(t) - \omega_0$, the frequency-dependent transmission produces a transmitted optical power deviation of

$$\Delta P_{trans}(t) = P_{inc}\, T'\, \Delta\omega(t) \qquad (5.8)$$

where $T' = dT / d\omega|_{\omega_0}$ is the slope of the grating transmission versus frequency at the center wavelength ω_0. This model of the grating as a (phaseless) linear frequency discriminator is sufficient for explaining Figure 5.9 and much of the observed results, by using (5.8) and specifying the nature of the frequency fluctuations.

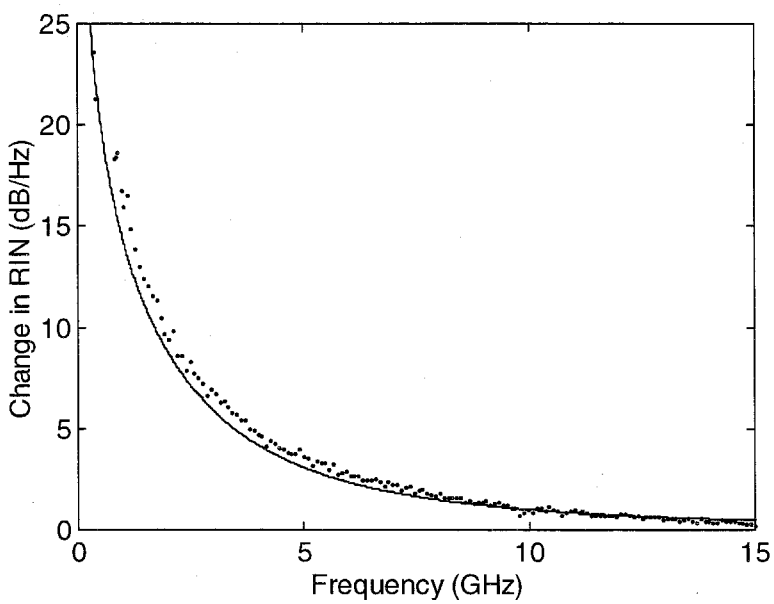

Figure 5.9. Change in RIN due to fiber grating.

with the laser tuned to the steep linear region on the low-wavelength side of the grating transmission spectrum. The points are experimental data and the line is equation (5.12).

The dominant source of laser noise is spontaneous emission into the laser mode and its spectral density can be derived from the rate equations. We represent the component of the spontaneous emission field that is in phase with the laser field by a

Langevin force $F_{\|}(t)$, which perturbs the laser intensity; and the other quadrature of the spontaneous emission field by a Langevin force $F_{\perp}(t)$, which perturbs the laser phase. The in-phase or parallel component $F_{\|}(t)$ produces an output power fluctuation $\Delta P_{\|}(t)$ with spectral density $S^{\|}_{\Delta P}(\Omega)$, and a frequency fluctuation $\Delta\omega_{\|}(t)$ with spectral density [5–13], as derived in Chapter 3,

$$S^{\|}_{\Delta\omega}(\Omega) = \left(\frac{\alpha\Omega_0{}^2}{2P_0\Omega}\right)^2 \left[\frac{(\tau_{ph}\Omega)^2 + 1}{(1/\tau\Omega)^2 + 1}\right] S^{\|}_{\Delta P}(\Omega) \tag{5.9}$$

Here α is the linewidth enhancement factor, Ω_0 is the laser resonant frequency, τ_{ph} is the photon lifetime, τ is the carrier lifetime, and P_0 is the optical output power. The intensity and frequency fluctuations produced by $F_{\|}(t)$ are correlated, and $\Delta\omega_{\|}(t)$ lags $\Delta P_{\|}(t)$ by a phase

$$\theta^{\|} = \frac{\pi}{2} + \tan^{-1}\left(\frac{(1/\tau\Omega) + \tau_{ph}\Omega}{1 - (\tau_{ph}/\tau)}\right) \tag{5.10}$$

For the laser conditions used, the laser parameters were determined by a fit to the RIN spectrum (without a grating) and to the change in RIN after a fiber of known dispersion, as in [5–13], giving $1/2\pi\tau = .39$ GHz and $1/2\pi\tau_{ph} = 31$ GHz. For frequencies in the range $1/\tau << \Omega << 1/\tau_{ph}$, as in this experiment, the quantity in brackets in (5.9) is nearly 1 and $\theta^{\|}$ is nearly $\pi/2$. Thus the intensity and frequency fluctuations produced by $F_{\|}(t)$ are 90° out of phase, and we can simply add the intensity noise power created by the grating from $S^{\|}_{\Delta\omega}(\Omega)$ to the initial intensity noise power $S^{\|}_{\Delta P}(\Omega)$ caused by $F_{\|}(t)$ directly.

The spontaneous emission term $F_{\perp}(t)$ produces no initial intensity fluctuations, but does create frequency fluctuations that are uncorrelated with $F_{\parallel}(t)$ and have a spectral density $S_{\Delta\omega}^{\perp}(\Omega) = 2K\omega_{ST}$, where ω_{ST} is the Schawlow-Townes linewidth and K is the Petermann enhancement factor for DFB lasers [5–17]. This also gets converted by the grating into an intensity noise power that adds with $S_{\Delta P}^{\parallel}(\Omega)$.

Putting $S_{\Delta\omega}^{\perp}(\Omega)$ and $S_{\Delta\omega}^{\parallel}(\Omega)$ into (5.8) we get the intensity noise spectral density after the grating,

$$S_{\Delta P}^{grating}(\Omega) = S_{\Delta P}^{initial}(\Omega)\left[T^2 + \left(\frac{T'\alpha\Omega_0{}^2}{2\Omega}\right)^2\right] + \left(P_0 T'\right)^2 2K\omega_{ST} \qquad (5.11)$$

The last term above is independent of frequency and represents a new noise floor created by the grating from $S_{\Delta\omega}^{\perp}(\Omega)$. It is usually smaller than either the initial intensity noise (attenuated by T^2) or that created by the grating from $S_{\Delta\omega}^{\parallel}(\Omega)$. Approximating it out, we arrive at a simple expression for the change in RIN due to the grating:

$$\Delta RIN(\Omega) = 10\log_{10}\left\{1 + \left(\frac{T'\alpha\Omega_0{}^2}{2T\Omega}\right)^2\right\} \qquad (5.12)$$

Figure 5.9 shows a plot of this expression (solid line), using the independently measured values of the grating transmission T and slope T' and the laser parameters Ω_0 and α, showing very good agreement with the experimental data.

Equation (5.12) predicts that RIN will always increase with a grating, due to the phase $\theta^{\parallel} \approx \pi/2$ between the correlated frequency and intensity noise. This is not always

the case. For frequencies that are low ($\Omega << 1/\tau$) or high ($\Omega >> 1/\tau_{ph}$) the frequency fluctuations $S^{\parallel}_{\Delta\omega}(\Omega)$ are independent of frequency and π out of phase with the intensity fluctuations. Thus a grating for which T increases linearly with ω (e.g., on the short-wavelength side of the reflection band) will compensate an increased intensity with a decreased transmission. The intensity noise from $F_{\parallel}(t)$ is eliminated completely when the grating slope is $T'/T = 2/(|\alpha|\Omega_0^2\tau)$ at low frequencies or $T'/T = 2/(|\alpha|\Omega_0^2\tau_{ph})$ at high frequencies.

In addition there are other sources of noise that can be eliminated with a linear frequency discriminator. Carrier fluctuations not involving spontaneous emission into the lasing mode, including those from pump current noise, produce frequency fluctuations that are in phase with the intensity fluctuations when $\Omega << \varepsilon P_0/\tau_{ph}$ (in the adiabatic chirp regime, typically up to several GHz), where ε is the nonlinear gain compression factor. The intensity noise from this source will be removed completely when the grating slope is $T'/T = -2\tau_{ph}/|\alpha|\varepsilon P_0$. For $\Omega >> \varepsilon P_0/\tau_{ph}$, the transient chirp regime, the intensity and frequency fluctuations are $\pi/2$ out of phase and a frequency discriminator can only increase the intensity noise from this source. We have also neglected mode partition noise, which is important at low frequencies and is affected differently by dispersive optical elements [5–18].

The discussion thus far has neglected the phase $\phi_t(\omega)$ of the complex grating transmittance $t(\omega)$, which is a good approximation when the transmittance is linear over the bandwidth of interest. In all other cases we must include the effect of grating

dispersion on the RIN. The phenomenon is the same in principle as in dispersive fiber, in which AM and FM noise are inter-converted by a mixing angle $\theta(\Omega) = \beta'' L\Omega^2/2$, where $\beta'' = \partial^2\beta / \partial\omega^2\big|_{\omega_0}$ is the fiber dispersion parameter and L the fiber length. For the case of a grating, the mixing angle is

$$\theta(\Omega) = \left[\phi_t(\omega_0 + \Omega) + \phi_t(\omega_0 - \Omega) - 2\phi_t(\omega_0)\right] / 2 \qquad (5.13)$$

An expression similar to (5.11) can be derived to include $\theta(\Omega)$, but an analytic treatment is intractable for gratings with narrow spectral features, and a numerical Fourier-domain calculation is preferable. The intensity noise after the grating is calculated from $\tilde{E}_{out}(\omega) = \tilde{E}_{in}(\omega)t(\omega)$, with $\tilde{E}_{in}(\omega)$ obtained from the Fourier-transformed rate equations containing $F_{\parallel}(t)$ and $F_{\perp}(t)$ as sources. Measuring the magnitude of the transmittance spectrum $|t(\omega)| = \sqrt{T(\omega)}$ allows us to infer the phase $\phi_t(\omega)$ numerically via a Kramers-Kronig integral [5–4]. This numerical calculation allows us to treat more narrow spectral features of a grating.

The grating phase plays a major role in changing the RIN and can reduce the RIN when T' is small. Figure 5.10 shows a RIN reduction of 2 dB obtained with the same grating as in Figure 5.7. The laser was tuned to the low-wavelength side of the spectrum near the weak sidelobe. The solid line of Figure 5.10 is the full numerical calculation, and if we exclude the grating phase the predicted RIN is several dB above the experimental value. The low-Ω prediction is somewhat artificial, given the limited resolution of $t(\omega)$,

and the variations in the data below 3 GHz might result from a fine structure in the grating spectrum that we cannot resolve.

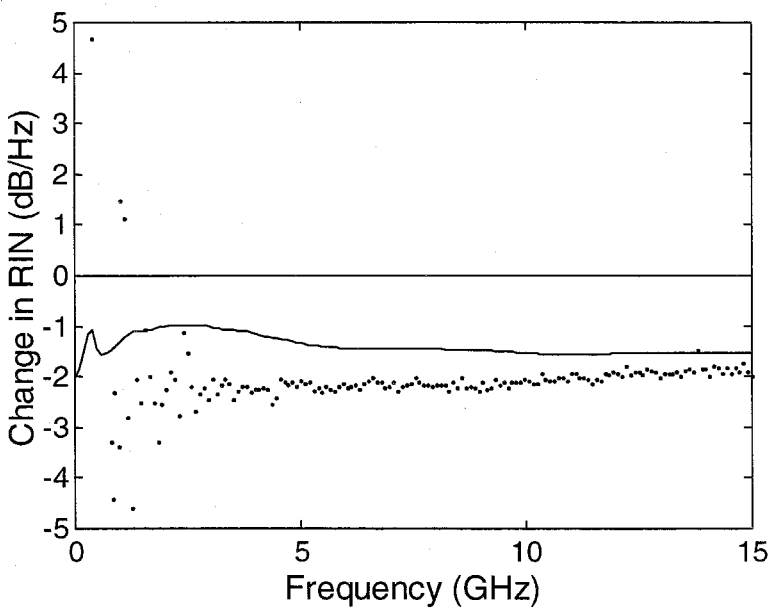

Figure 5.10. Change in RIN due to fiber grating showing a decrease in the noise. The points are experimental data and the solid line is the numerical calculation using the measured grating spectrum.

As an example of RIN dependence on laser tuning, Figure 5.11 shows RIN changes from a grating at three different wavelengths, each among the weak reflection sidelobes on the long-wavelength side of the grating spectrum. The RIN increases at low frequencies but deviated from the $1/\Omega^2$ dependence of (5.12) and decreases at some frequencies (Figure 5.11, circles). The numerical calculation (solid line) reflects these

effects qualitatively but is limited by the resolution of the optical spectrum analyzer (10 GHz), which essentially smoothes the transmission function used in the calculation and fails to predict the more frequency-sensitive features of $\Delta RIN(\Omega)$.

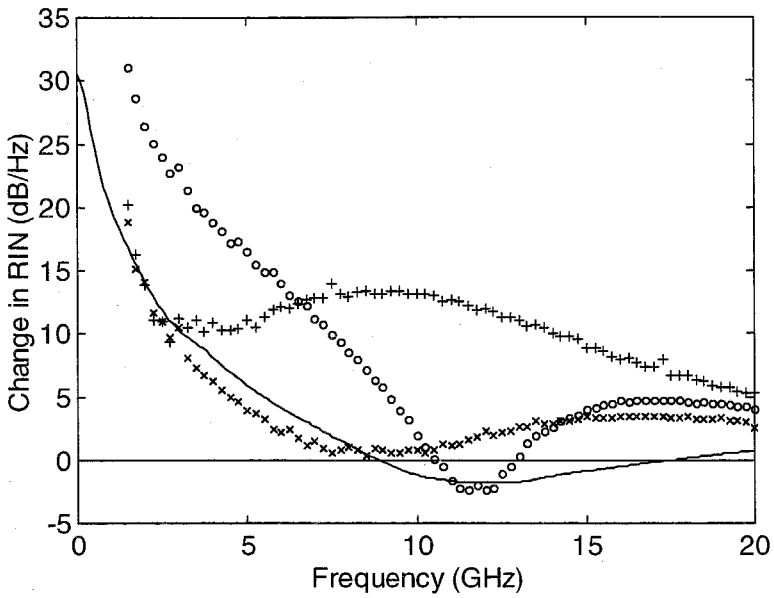

Figure 5.11. Change in RIN due to fiber grating.

The laser tuned to three different wavelengths among the weak sidelobes of the reflection spectrum. The symbols are experimental data and the solid line is a typical numerical calculation using the measured grating spectrum.

To be useful for RIN reduction at low frequencies, a grating should be apodized carefully to produce a smooth grating spectrum. The numerical calculation indicates that this laser is capable of more than 5 dB of RIN reduction with an appropriate grating.

Reductions of 7 dB have been achieved with a Michelson interferometer at low frequencies [5–14], and there is no physical reason why this result could not be duplicated with a fiber grating. Practically, a 5 dB higher signal-to-noise ratio is maintained in the fiber where both signal and noise suffer a loss of .2 dB/km. A 5 dB lower noise will reach the shot noise floor first at which point SNR degrades; however, there is still 10 km further until the SNR is matched.

5.4. Two Phase Mask Method for Fabrication of Chirped Gratings

The development of fiber Bragg gratings has enabled fabrication of a variety of different Bragg grating devices that were not possible previously, such as dispersion compensators and band-rejection filters. In some of these applications, a specific variation of the index of refraction along the structure is required, which has prompted investigation into new techniques for flexibility in the fabrication of the gratings. The most preferred method of fabrication uses a phase mask due to the easier alignment, reduced excimer stability and coherence requirements, and better reproducibility. The main disadvantage is the need to have a separate phase mask for each Bragg wavelength, chirp or apodization.

A long-period (LP) phase mask was developed to control the local angle of incidence of the UV beam incident on the short-period (SP) phase mask [5–19]. The rapid variation of the index of refraction in the fiber core is determined by the SP phase mask, whereas the apodization and chirp can be modified by changing the groove width and/or

depth and by varying the period along the long-period mask. This is an inexpensive way to add flexibility to the fabrication of fiber gratings, since the mask can be fabricated by UV lithography instead of e-beam lithography that is needed to obtain μm features. With only one SP phase mask, which are expensive and involve complicated fabrication procedures, various index of refraction profiles can be obtained by using different LP phase masks, which are easier to fabricate. In addition, it offers the advantages of phase mask fabrication techniques such as good reproducibility and parallel manufacturing of devices. The concept is illustrated in Figure 5.12.

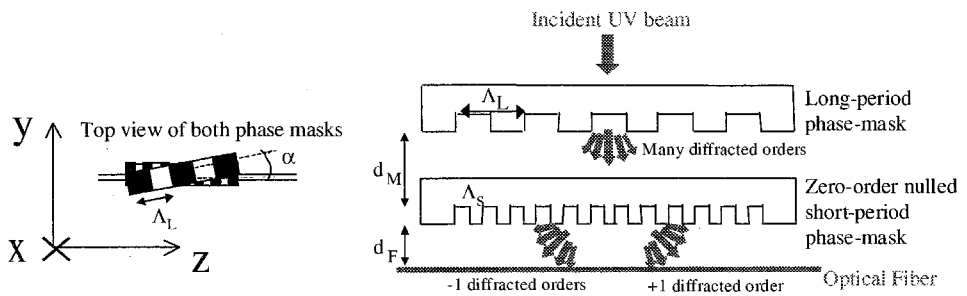

Figure 5.12. Two phase mask method for producing chirped gratings.

The incident UV beam is diffracted into several low spatial-frequency orders by the long period, Λ_L, phase mask. Each of these is diffracted into +1 and –1 high spatial-frequency orders by the short-period, Λ_S, phase mask. The distance between the phase masks is d_1, and the distance between the SP phase mask and the fiber core is d_2. The LP phase mask, rotated by α in the y-z plane, diffracts the UV beam according to

$$\Lambda_L \sin\theta_{Ln} = n\lambda_{UV} = n\frac{2\pi}{k_{UV}} \tag{5.14}$$

where θ_{Ln} is the angle of n^{th} order beam measured against the vertical (x-axis). The field leaving the first (LP) phase mask is

$$E_{LP}(x,y,z)=\sum_{n}\exp\left[-ik_{UV}\left(\sin\theta_{Ln}\left(z\cos\alpha+y\sin\alpha\right)+d_1\cos\theta_{Ln}\right)\right] \tag{5.15}$$

and after the second (SP) mask, a new angle $\theta_{Sn}^{\pm}$ emerges for the two diffracted orders following

$$k_{UV}\sin\theta_{Sn}^{\pm}=n\frac{2\pi}{\Lambda_L}\pm\frac{2\pi}{\Lambda_S} \tag{5.16}$$

The field now arriving at the fiber core is

$$E(x,y,z)=E_{LP}(x,y,z)\times\ldots \left[\exp\left(-ik_{UV}\left(\frac{2\pi}{\Lambda_S}z+\cos\theta_{Sn}^{+}d_2\right)\right)+\exp\left(-ik_{UV}\left(-\frac{2\pi}{\Lambda_S}z+\cos\theta_{Sn}^{-}d_2\right)\right)\right] \tag{5.17}$$

Under these conditions, the change in refractive index induced in the fiber core is given by

$$\Delta n(y,z)\propto\left|E(y,z)\right|^2 \tag{5.18}$$

$$\Delta n(y,z)= \Delta\tilde{n}\sum_{n,m}e^{-im\frac{2\pi}{\Lambda_L}(z\cos\alpha+y\sin\alpha)}e^{im(m+2n)\varphi_L}E_{n+m}E_n^{*}\left(\cos(m\varphi_S)+\cos\left(2\frac{2\pi}{\Lambda_S}z-(m+2n)\varphi_S\right)\right) \tag{5.19}$$

where $\Delta\tilde{n}$ is the amplitude of the change that would be induced by the UV beam in the absence of the LP phase mask, and the angles

$$\varphi_L \cong \frac{\pi\lambda_{UV}d_1}{n_{UV}\Lambda_L^2} \text{ and } \varphi_S \cong \frac{2\pi\lambda_{UV}d_2}{n_{UV}\Lambda_L\Lambda_S}\Bigg/\left(1-\left(\frac{\lambda_{UV}}{n_{UV}\Lambda_S}\right)^2\right)^{1/2} \tag{5.20}$$

with λ_{UV} the exposing wavelength and n_{UV} the refractive index of fused silica at λ_{UV}, arise from phase differences of the different diffraction orders as they propagate along the x-direction. The approximation for φ_F and φ_M is valid for $\Lambda_L >> \Lambda_S$.

In the two phase mask fabrication technique, a grating tilt is induced when the phase mask and fiber are not aligned, which results in coupling of modes of different symmetry. This can be disadvantageous in some applications, and in general cannot be used to tune the Bragg wavelength. Equation (5.19) shows that if the fiber radius is much smaller than Λ_L, as will be usually the case, the variation of Δn across the fiber (y-axis) when $\alpha \neq 0$ is negligible. Thus, freely rotating the LP mask to obtain a change in the effective long-period Λ_L gives additional flexibility to the fabrication.

Many grating apodization techniques also induce a variation in the background refractive index, which produces undesirable self-chirping. From (5.19) it can be seen that the amount of self-chirping can be controlled by the angle φ_S, i.e., the distance between SP phase mask and fiber.

Substituting a quasi-periodic binary amplitude mask for the LP phase mask would induce a change in refractive index similar to that in (5.19), but with φ_L and φ_S zero, i.e., independent of propagation distance along the x-axis. Thus, the background refractive index has the same variation as the grating apodization. Moreover, the values that the coefficients E_n can take are restricted to $E_{-n} = E_n^*$ and $E_0 > 0$, the mask induces loss in

the beam, and the only design parameter is the duty cycle, posing possible limitations in the grating design.

Considered next is the case when Λ_L varies along the mask in the z-axis and the average long-period, $\overline{\Lambda}_L$, is short enough that multiple resonance peaks occur spaced in wavelength by much more than the spectral width of the peaks. In this case, each resonance at wavelength λ_m, with

$$\frac{\overline{n}}{\lambda_m} = \frac{1}{\Lambda_S} + m\frac{1}{2\overline{\Lambda}_L} \tag{5.21}$$

and $\overline{n}$ the modal index, can be treated as an individual grating with coupling coefficient, κ_m, given by

$$\kappa_m = \tilde{\kappa}\sum_n e^{i(m+2n)(m\varphi_m+\varphi_f)} E_{n+m}E_n^* \, e^{-im\frac{2\pi}{\overline{\Lambda}_L^2}\Delta\Lambda_L(z)z} \tag{5.22}$$

where $\tilde{\kappa}$ is the coupling coefficient that would be obtained in the absence of the LP mask, $\Lambda_L(z) = \overline{\Lambda}_L + \Delta\Lambda_L(z)$ and we assumed $\overline{\Lambda}_L >> \Delta\Lambda_L(z)$. When $\Delta\Lambda_L(z)$ varies linearly along the LP mask, a linear chirp is obtained. Figure 5.13 shows the simulation for a uniform SP and a chirped LP phase mask with a period varying linearly from 380-420 μm over 2 cm.

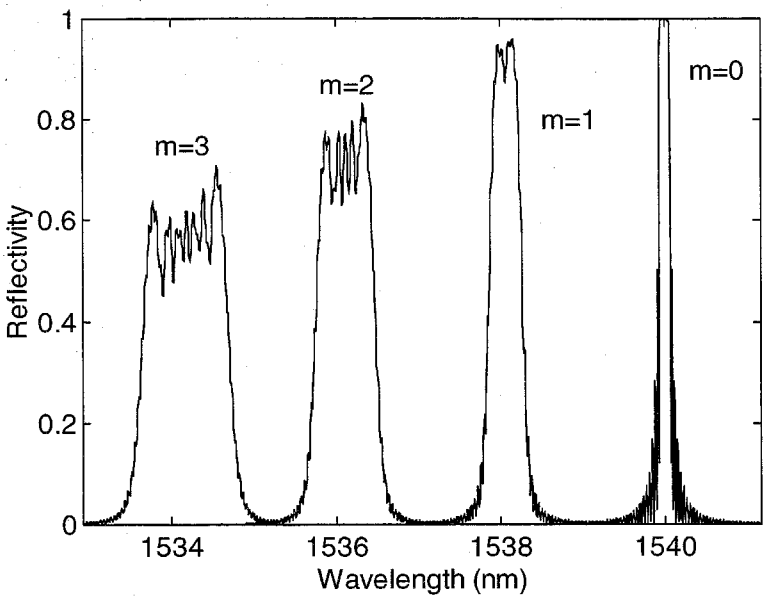

Figure 5.13. Double phase mask simulation for with chirped LP mask.

Several LP phase masks were made using simple contact UV lithography. The pattern was transferred into a quartz substrate using C_2F_6 reactive ion etching. Because of the large feature size, no high resolution lithography techniques were necessary, making these masks relatively cheap and simple to fabricate.

Figure 5.14 shows the reflection spectrum for two fiber gratings made in hydrogen-loaded SMF-28 fiber with a zero-nulled uniform SP mask Λ_s=1049.05 nm and uniform LP masks with period Λ_L=200 μm (solid) and Λ_L=400 μm (dashed), respectively. The gratings were 2 cm long. The depth of the grooves was not carefully controlled and was measured to be 600 nm and 450 nm, respectively. This gave rise to multiple peaks separated by 4 nm and 2 nm, respectively, as predicted by the model above.

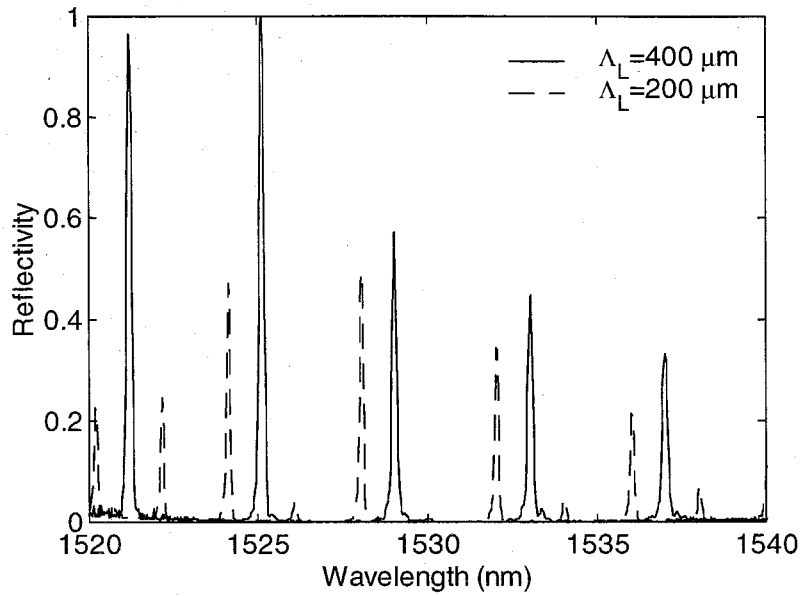

Figure 5.14. Reflection spectrum for fiber gratings fabricated with double-phase mask technique with uniform SP mask Λ_s=1049.05nm and uniform LP mask Λ_L=200 μm (solid) and Λ_L=400 μm (dashed).

Figure 5.15 shows the reflection spectrum for gratings made with a chirped LP phase mask with period linearly varying from 380 μm to 420 μm and groove depth 450 nm. Two gratings were written with tilt angles α=0° (solid) and α=22° (dashed), corresponding to resonance peak spacing 2 nm and 1.8 nm, respectively, as predicted by our model. The long-period variation corresponds to a strong chirp with Bragg wavelength deviation of m times 0.2 nm around the m^{th} resonance peak. The increasing width of the resonance peaks can indeed be observed as they separate from the main Bragg peak at ~1521.2 nm.

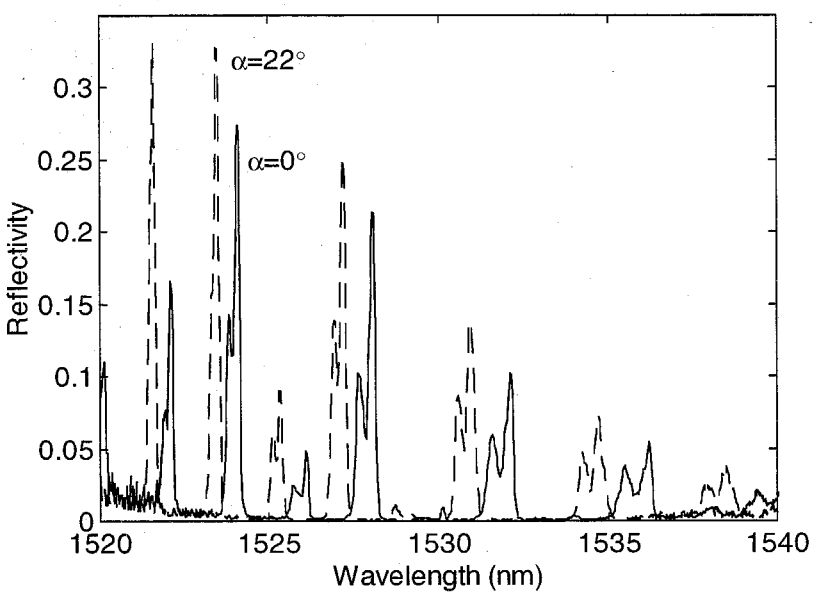

Figure 5.15. Reflection spectrum for fiber gratings fabricated with double-phase mask technique with uniform SP mask Λ_s=1049.05 nm and linearly varying LP mask Λ_L from 380 μm to 420 μm for tilt angles α=0° (solid) and α=22° (dashed).

Figure 5.16 shows the measured reflectivity of the m=1 chirped grating and its measured group delay. The chirp was found to be -350 ps/nm.

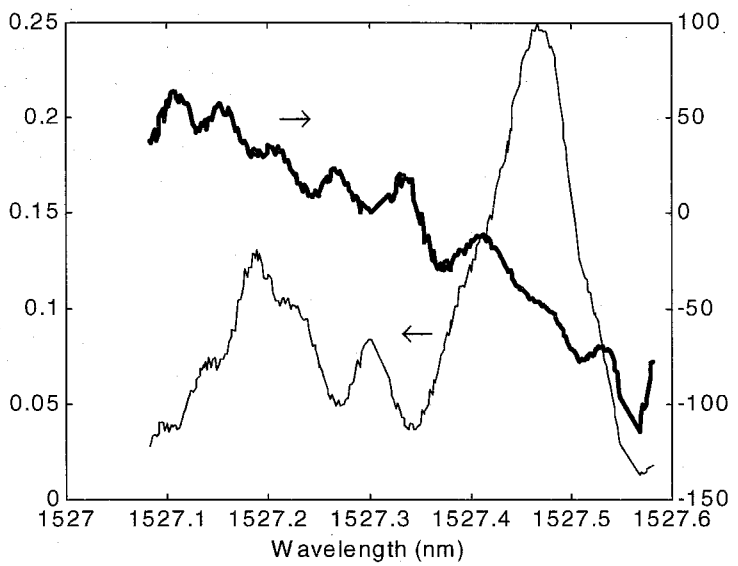

Figure 5.16. Reflectivity and group delay for one of the chirped gratings.

5.5. Gratings Fabricated in Ion-exchanged Waveguides

The UV photosensitivity in Ge-doped silica is understood today with the absorption-band bleaching model, combined with use of Kramers-Kronig relations to obtain the refractive index change [5–20]. Such photobleaching has also been performed in a K^+-exchanged waveguide with the 351 nm line from an Ar^+ laser [5–21]. In this section, we report writing a diffraction grating in a 2 mm thick glass sample used for making ion-exchanged waveguides by exposure to light from a 248 nm KrF excimer laser, without germanium doping or hydrogen loading. The composition of BGG31 glass by atomic percent is 58.3% Oxygen, 17.6% Silicon, 7.1% Aluminum, 6.8% Sodium, 6% Boron, 4.2% Fluorine, 0.06% Arsenic, and <0.01% Potassium. The three-dimensionally written

gratings are evidence that neither germanium nor hydrogen need be present to produce a reasonable index change with 248 nm irradiation. The effect of the excimer exposure on the transmission of the glass was shown in Figure 4.11.

For the grating inscription, the BGG31 glass sample was placed directly under a phase mask with a pitch of 1049.28 nm. The phase mask was designed to suppress the 0th order diffracted beam at 248 nm. For the best results, the glass was placed in direct contact with the phase mask and exposed for 10 minutes with 168 mJ/pulse at 50 Hz. Other trials were performed with gaps of 125 μm and 250 μm between the phase mask and the sample, but in each case the diffraction spots from the Ar^+ laser were reduced in intensity. This is consistent with the reports [5–22] [5–23] that it is not the temporal coherence that limits fringe visibility with mask/glass (or fiber) separation, but the spatial coherence. The reason being that with increased propagation past the phase mask, light overlaps from more points that passed through the mask.

The various diffraction orders from the phase mask interfere and produce index variation gratings in the material each written at a different angle ϕ. Figure 5.17 shows the experimental setup for the exposure and the diffracted orders of the phase mask.

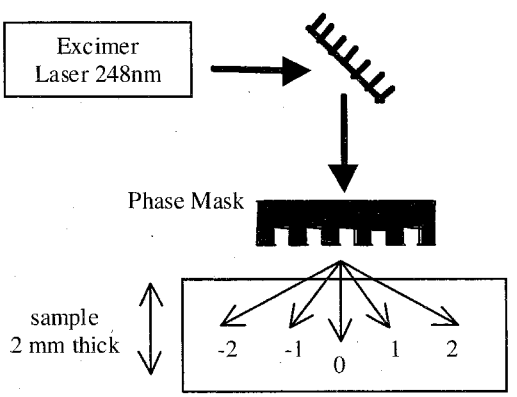

Figure 5.17. The experimental setup for writing gratings. $0, \pm 1, \pm 2$ orders were found and produced all combinations of holographic gratings.

The resultant field intensity at the surface of the sample for five diffracted beams is

$$I(x) = \left| E_0 + E_1 e^{ikx \sin\theta_1} + E_{-1} e^{-ikx \sin\theta_{-1}} + E_2 e^{ikx \sin\theta_2} + E_{-2} e^{-ikx \sin\theta_{-2}} \right|^2 \qquad (5.23)$$

$$\text{where} \quad \sin\theta_m = \frac{m\lambda}{\Lambda_{mask}} \qquad (5.24)$$

where k is the propagation constant, λ = 248 nm, Λ_{mask} is the mask period = 1049.28 nm, and *m* is the diffracted order. Figure 5.18 shows an example of a grating produced with the -2, +1 orders and subsequent characterization.

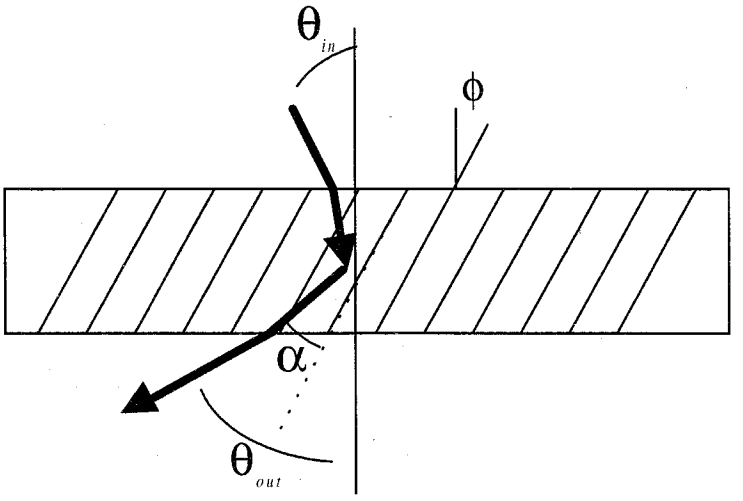

Figure 5.18. Bragg diffraction from one of the induced volume gratings. The probing was performed with the 476 nm line from an Ar^+ laser. The parallel lines show the induced index-variation volume hologram.

The angle ϕ for a given grating is determined as the bisector of the angle between the propagation directions of any two orders, denoted m_1 and m_2. The ± 1 orders will produce gratings with $\phi = 0$ as will the ± 2 orders. α is the Bragg angle, measured as the angle of the incident or reflected ray with the tangent to the grating lines.

This section discusses the characterization of the written gratings. Probing these gratings was accomplished using the 476 nm line from an Ar^+ laser operating at about 50 mW. Evidence for a volume grating was that a very precise incident angle (θ_{in}) was needed to observe Bragg diffraction (Figure 5.18). If only a surface grating had been produced by the excimer laser, then Bragg diffraction would occur at a continuum of angles. The Bragg condition for these photowritten gratings is

$$2\left[\frac{\Lambda_{mask}}{m_1 - m_2}\cos\phi\right]\sin\alpha = m\lambda \qquad (5.25)$$

where the term in brackets is the actual period of the desired grating, derived from the intensity distribution of (5.23) and tilt angle ϕ. m_1 and m_2 refer to the orders diffracted from the phase mask which produce the grating, m is the diffraction order, and λ is 476 nm. θ_{in} and θ_{out} can be obtained from α in (5.25) and accounting for the background material index.

Figure 5.19 shows the predicted and observed Bragg diffraction spots. All are first order diffraction spots, except for the two depicted as stars.

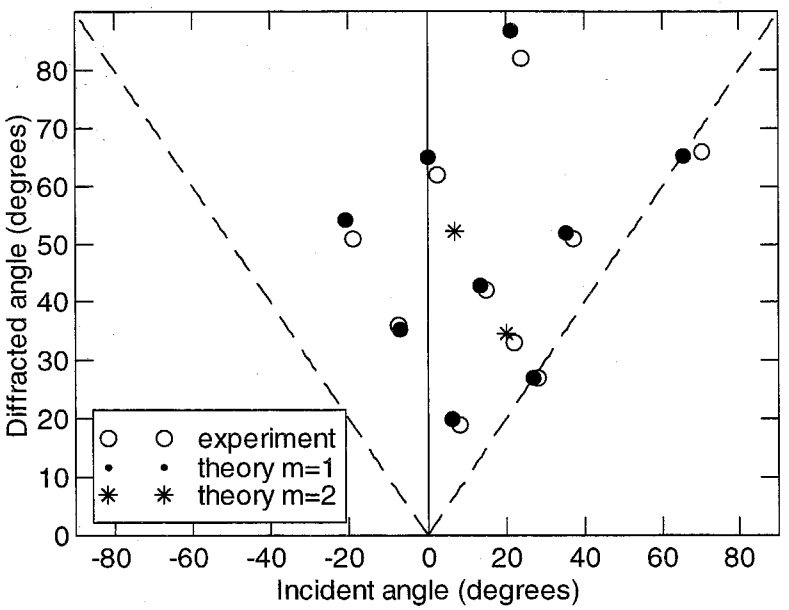

Figure 5.19. Predicted and observed diffracted spots.

This is the minimum number of non-redundant spots. By convention, a diffracted ray on the opposite side of the surface normal is defined as a positive incident angle.

The stars are second order diffraction spots from a particular grating much weaker in intensity, of which only one was observed. The dashed line on the right represents equal incident and diffracted angles. The two points which lie on this line are from the m_1, $m_2 = \pm 1$ and m_1, $m_2 = \pm 2$ gratings. The intensities of these spots were recorded and used to determine the relative power in the diffracted orders of the phase mask. Using the ratios of spot intensities, it was determined that the phase mask diffracted 94% of the 248 nm

excimer laser into the ± 1 orders, 5% into the ± 2 orders and <0.5% into the 0th order, as designed. Evidence of the ± 3rd order was detected but not directly quantified.

Using the intensity data, it was possible to estimate Δn for the strongest grating written in the glass ($m_1 = 1$ and $m_2 = -1$). It was necessary to know the penetration depth of the grating, for that determines the interaction length, and hence the peak reflectivity, for the grating. According to both A. Othonos and P. E. Dyer [5–22] [5–23], KrF excimer lasers have the spatial coherence to provide high fringe contrast out to only a few hundred microns past the phase mask. We performed exposures with mask/glass separation of 125 and 250 μm, each with increasingly faint gratings produced, so at best, it was interpolated that the penetration depth is between 500 μm and 1 mm which produces a coherent interference between two diffracted orders. However, by separating the mask and glass, the rigidity of the setup was compromised and mechanical vibrations could have been the largest factor in reducing the grating strength. Nonetheless, the deeper the grating written into the glass, the longer the grating interaction with the argon beam. Shown in Figure 5.20 is the peak reflectivity for a grating with two different depths. The left curve assumes a penetration depth of 1 mm, and the right curve assumes a penetration depth of .5 mm. Peak reflectivity for a uniform grating is given by [5–24]

$$R(\Delta n) = \tanh^2\left(\frac{\pi \Delta n L}{\lambda_{Bragg}}\right) \tag{5.26}$$

Note that even if the penetration depth is .5 mm, the effective grating length (L) that the argon beam interacts with when incident at 27° is .17 mm. For 1 mm penetration, L = .34

mm. The horizontal line is the measured reflectivity for the 1st order of the strongest written grating. Δn is expected to lie on this line. In all cases the background refractive index of the glass was taken as 1.4.

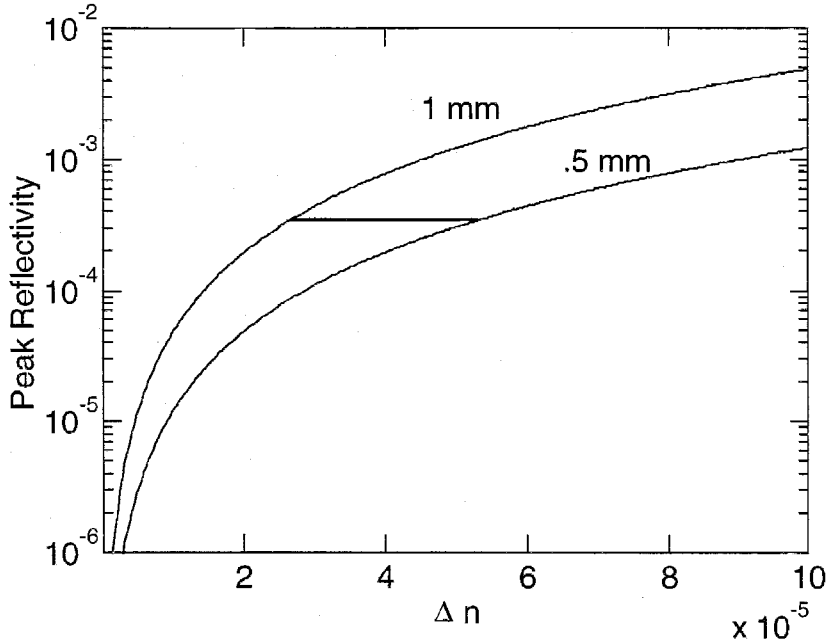

Figure 5.20. Computed index change (Δn) for the grating written from the ± 1 phase mask orders. The curves are expected peak reflectivity for the labeled grating length. The horizontal line is the measured reflectivity.

In conclusion, we have demonstrated volume gratings written in BGG31 glass with an excimer laser at 248 nm. The glass has neither germanium nor hydrogen to enhance the photosensitivity of the glass. The index change inferred was $(3.9 \pm 1.3) \times 10^{-5}$, a reasonable value for this composition of glass. Tests of the transmission properties of

these gratings with light coupled into the channel waveguides have been performed [5–25], [5–26] and better than 90% transmission dips at the Bragg wavelength of 1.53 μm have been obtained.

References for Chapter 5

[5–1] G. W. Yoffe, Peter A. Krug, F. Ouellette, and D. A. Thorncraft, "Passive temperature-compensating package for optical fiber gratings," Appl. Opt. 34 (30) p. 6859-6861 (1995).

[5–2] B. Wedding, "Analysis of fiber transfer-function and determination of receiver frequency-response for dispersion supported transmission," Electron. Lett. 30, p. 58-59 (1994).

[5–3] B. J. Eggleton, T. Stephens, P.A. Krug, G. Dhosi, Z. Brodzeli, and F. Ouellette, "Dispersion compensation using a fibre grating in transmission," Electron. Lett. 32, p. 1610-1611 (1996).

[5–4] M. McAdams, E. Peral, D. Provenzano, W. K. Marshall, and A. Yariv, "Improved laser modulation response by frequency modulation to amplitude conversion in transmission through a fiber grating," Appl. Phys. Lett. 71, (18) p. 879-881 (1997).

[5–5] C. Harder, K. Vahala, and A. Yariv, "Measurement of the linewidth enhancement factor-alpha of semiconductor lasers," Appl. Phys. Lett. 42, p. 328-330 (1983).

[5–6] J. Park, W. V. Sorin, and K. Y. Lau, "Elimination of the fibre chromatic dispersion penalty on 1550nm millimetre-wave optical transmission," Elect. Lett. 33, p. 512-513 (1997).

[5–7] F. Ouellette, "Limits of chirped pulse-compression with an unchirped Bragg grating filter," Appl. Opt. 29, p. 4826-4829 (1990).

[5–8] T. L. Koch and R. A. Linke, "Effect of nonlinear gain reduction on semiconductor-laser wavelength chirping," Appl. Phys. Lett. 48, p. 613-615 (1986).

[5–9] A. Røyset, L. Bjerkan, D. Myhre, and L. Hafskjær, "Use of dispersive optical-fiber for characterization of chirp in semiconductor lasers," Elect. Lett. 30, p. 710-712 (1994).

[5–10] R. C. Srinivasan and J. C. Cartledge, "On using fiber transfer-functions to characterize laser chirp and fiber dispersion," Phot. Tech. Lett. 7, p. 1327-1329 (1995).

[5–11] Amnon Yariv, *Optical Electronics in Modern Communications*, 5th ed., 509 (Oxford University Press, 1997).

[5–12] George Arfken, *Mathematical Method for Physicists*, 3rd ed., 426 (Academic Press, 1985).

[5–13] W. K. Marshall, J. Paslaski, and A. Yariv, "Reduction of relative intensity noise of the output field of semiconductor lasers due to propagation in dispersive optical fiber," Appl. Phys. Lett. 68, p. 2496-2498 (1996).

[5–14] K. J. Vahala and M. A. Newkirk, "Intensity noise-reduction in semiconductor-lasers by amplitude-phase decorrelation," Appl. Phys. Lett. 57, p. 974-976 (1990).

[5–15] M. A. Newkirk and K. J. Vahala, "Amplitude phase decorrelation - a method for reducing intensity noise in semiconductor-lasers," J. Quantum Electron. 27, p. 13-22 (1991).

[5–16] M. McAdams, D. Provenzano, E. Peral, W. K. Marshall, and A. Yariv, "Effect of transmission through fiber gratings on semiconductor laser intensity noise," Appl. Phys. Lett. 71, (23) p. 3341-3343 (1997).

[5–17] J. Wang, N. Schunk, and K. Petermann, "Linewidth enhancement for DFB lasers due to longitudinal-field dependence in the laser cavity," Electron. Lett. 23, p. 715-717 (1987).

[5–18] X. L. Lu, C. B. Su, and R. B. Lauer, "Increase in laser RIN due to asymmetric nonlinear gain, fiber dispersion, and modulation," Phot. Tech. Lett. 4, p. 774-777 (1992).

[5–19] Eva Peral, Reginald Lee, Dan Provenzano, and Amnon Yariv, "Double phase mask fabrication of fiber Bragg gratings," Conference Proceedings, Fiber Bragg Gratings (Sept. 1999).

[5–20] Victor Mizrahi, Sophie LaRochelle, and George I. Stegeman, "Physics of photosensitive-grating formation in optical fibers," Phys. Rev. A 43, p. 433-438 (1991).

[5–21] J. E. Roman and K. A. Winick, "Photowritten gratings on ion-exchange slab waveguides," Opt. Lett 18, p. 808-810 (1993).

[5–22] Andreas Othonos and Xavier Lee, "Novel and Improved Methods of Writing Bragg Gratings with Phase Masks," IEEE Phot. Tech. Lett. 7, 1183-1185 (1995).

[5–23] P.E. Dyer, R.J. Farley, and R. Giedl, "Analysis of grating formation with excimer laser irradiated phase masks," Opt. Comm. 115, p. 327-334 (1995).

[5–24] Andreas Othonos, "Fiber Bragg Gratings," Rev. Sci. Instrum. 68, p. 4309-4341 (1997).

[5–25] D. F. Geraghty, Dan Provenzano, S. Honkanen, W. K. Marshall, Amnon Yariv, and N.Peyghambarian, "Gratings photowritten in ion-exchanged glass channel waveguides," Elect. Lett. 35 (7) p. 585-587 (Apr. 1999).

[5–26] D. F. Geraghty, Dan Provenzano, M. Morrell, J. Ingenhoff, S. Honkanen, Amnon Yariv, and N.Peyghambarian, "Polarization independent Bragg gratings in ion-exchanged glass channel waveguides," Elect. Lett. 36 (6) p. 531-532 (Mar. 2000).

Page 132 is a blank page.

Chapter 6 - Single Mode Fiber Ring Lasers

6.1. Introduction

The explosive growth of the telecommunications industry has fueled an ever-increasing demand for bandwidth. Dense Wavelength Division Multiplexing (DWDM) has emerged as a crucial enabling technology. With stricter demands on source lasers, the shortcomings of traditional DFB semiconductor lasers (SCL) are beginning to surface. First, DFB lasers age in time and the wavelength drifts over the course of a few years of use. Frequency lockers are required to stabilize these lasers within the specifications of each particular communications channel. Also, DFB lasers are typically less than a millimeter in length, which gives rise to a linewidth of about 1 MHz, due mostly to phase noise. This large phase noise is converted into amplitude noise by the dispersion in the fiber (Chapter 3) limiting the performance of the system. Sidemode partition noise has a similar effect as the total noise is increased by fiber propagation. Finally, the fabrication and the assembly of the semiconductor lasers are both labor and capital intensive. The technology for our single mode fiber ring laser (FRL) has an advantage in each one of these areas.

In the past 10 years Erbium Doped Fiber Amplifiers (EDFA) have also facilitated long fiber links by amplifying lightwave signals directly without the need for optical-to-electrical conversion midstream. This technology, combined with fiber Bragg gratings, has opened a new field of fiber lasers at 1550 nm. There is now vigorous research conducted on quarter-wave shifted DFB fiber lasers. While they are quite promising as communications sources, our ring laser has a larger gain section and is thus capable of more output power, better sidemode suppression and even smaller linewidth. The challenges have been to filter out only a single mode for lasing in the ring. This is accomplished with a now proprietary configuration of fiber Bragg gratings.

This chapter first discusses the spectrum of gain for erbium, the advantages of the larger cavity and ring geometry, and output optimization. Then the properties of the laser are presented: optical spectrum, LI curve, linewidth, power and wavelength stability, temperature sensitivity, and Relative Intensity Noise (RIN). Finally, the fiber laser's role in optical communications is discussed.

6.2. Erbium Gain

The rare earth element erbium has the benefit of an atomic transition ($^4I_{15/2}$ and $^4I_{13/2}$ levels) at 1540 nm (wavelength of lowest loss in silica) and is doped into the fiber with some 30 to 50 nm gain bandwidth depending the additions of other dopants. There is another transition at 980 nm which has a fast decay to the excited 1540 nm levels. Many

degenerate sublevels for each state are lifted by the erbium presence in amorphous silica. This causes homogenous broadening effects to be measured due to thermalization. Figure 6.1 shows a gain measurement with and without a probe laser present. The presence of the probe reducing the gain over 40 nm indicated significant homogenous broadening. Low temperature measurements reveal the true inhomogeneous nature of the transition and make it possible to study the fine structure of the transition [6–1].

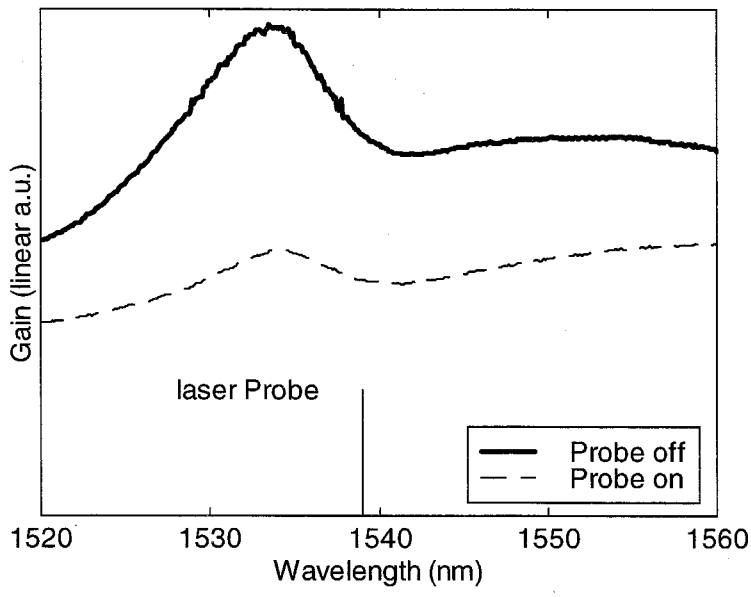

Figure 6.1. Erbium gain bandwidth.

To analyze the gain properties of an erbium-doped optical fiber, we solve the rate equations for the photon density and excited state population. We treat a population density (ρ) of erbium as a three level system, with fractional population densities $N_1(z,t)$, $N_2(z,t)$, and $N_3(z,t)$. A 980 nm pump excites atoms from N_1 to N_3. In this model, we

neglect amplified spontaneous emission (reasonable for amplifiers of under 20 dB) and assume the decay from N_3 to the 1540 nm excited level is fast enough to treat $N_3 = 0$ [6–2]. Thus,

$$N_1+N_2 = 1. \tag{6.1}$$

Both the pump beam and the signal beam are treated as equals in the rate equations, with their respective cross-sections (σ_i), absorption and emission coefficients (σ_i^e and σ_i^a), and mode confinement factors (Γ_i) over cross-sectional area "A." The subscript, "i," references "p" for pump and "s" for signal. For the case of copropagating pump and signal beams, the rate equations are

$$\begin{aligned} \frac{\partial N_2}{\partial t} &= -\frac{N_2}{\tau} - \frac{1}{\rho A}\sum_i \frac{\partial P_i}{\partial z} \\ \frac{\partial P_i}{\partial z} &= \rho\Gamma_i\left(\sigma_i^e N_2 - \sigma_i^a N_1\right)P_i \\ &\text{where } i = p,s \end{aligned} \tag{6.2}$$

where τ is the spontaneous emission lifetime. P_i refers to photon number per second (Power/photon energy). Note that, in the second equation, there is no pump emission from N_2, thus, $\sigma_p^e = 0$. To obtain steady state power equations, set $\frac{\partial N_2}{\partial t} = 0$ and use (6.1) to eliminate N_2 from the equations above with

$$\begin{aligned} N_2 &= \frac{1}{\sigma_i}\left(\frac{1}{\rho\Gamma_i P_i}\frac{\partial P_i}{\partial z} + \sigma_i^a\right). \\ &\text{where } \sigma_i = \sigma_i^e + \sigma_i^a \end{aligned} \tag{6.3}$$

Substituting into the rate equation for the population, we obtain the photons/sec evolution along the fiber. For the signal photons,

$$\frac{\partial P_s}{\partial z} = -\left(\alpha_s + \frac{1}{P_s^{sat}}\sum_i \frac{\partial P_i}{\partial z}\right)P_s$$

where

$$\alpha_s \equiv \rho\Gamma_s\sigma_s^a \qquad (6.4)$$

$$P_s^{sat} \equiv \frac{A}{\tau\Gamma_s\left(\sigma_s^a + \sigma_s^e\right)}$$

Upon integration over length L, the power out of the amplifier is

$$P_s^{out} = P_s^{in}\exp\left[-\alpha_s L - \frac{1}{P_s^{sat}}\left(P^{out} + P^{in}\right)\right] \qquad (6.5)$$

where P^{out} and P^{in} are the sums of the pump and signal photons.

Figure 6.2 shows the data and curve fits for a two-section of sample of erbium. The first section is 12 cm of ~5000 ppm Er^{3+} dopant, followed by a 5 cm codoped section of similar Er^{3+} concentration with Yb^{3+} in order to increase the pump absorption [6–3]. The figure shows signal gain (P_s^{out}/P_s^{in}) vs. P_s^{in}. Each curve is for a different pump power ranging from 0 mW to 90 mW. The fitted parameters are small signal gain constant (αL) and saturation power (P_s^{sat}) for each section and were found to be: $\alpha L(1)$= 1.01, $P_s^{sat}(1)=2.4\times10^{-4}$ mW, and $\alpha L(2)$= .094, $P_s^{sat}(2)$=0.65 mW. The biggest difference between the two fiber types is the codoped fiber has a 3 order of magnitude larger saturation power. This configuration has the advantage that after a few centimeters of Er gain, there is a final few centimeters which absorb more pump and maintain gain without saturating as drastically for a higher ring laser output power.

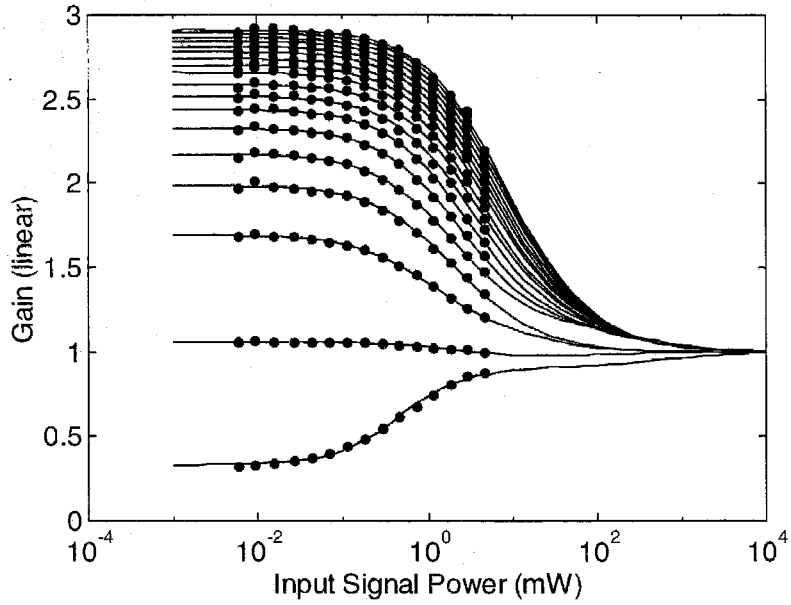

Figure 6.2. Experimental gain data (points) with fitted theoretical curves.

6.3. Ring Laser Geometry

Fiber ring lasers are attraction due to their simple geometry and ease of assembly. No end mirrors are needed, only some form of coupler to introduce pump light and couple output power. However, because of other necessary components such as isolators, polarization controllers, and spectral filters, the cavity ends up being fairly long and multimode lasing oscillation is hard to avoid. Figure 6.3a. shows a typical linear fiber lasing cavity with Bragg reflectors as end mirrors and (b) shows the effect that other resonant modes have on the gain saturation. Because other potential (lasing) standing modes physically have

different overlap in the gain region, the lasing mode fails to saturate the entire gain leaving room for sidemodes to experience less saturated gain and are not well suppressed.

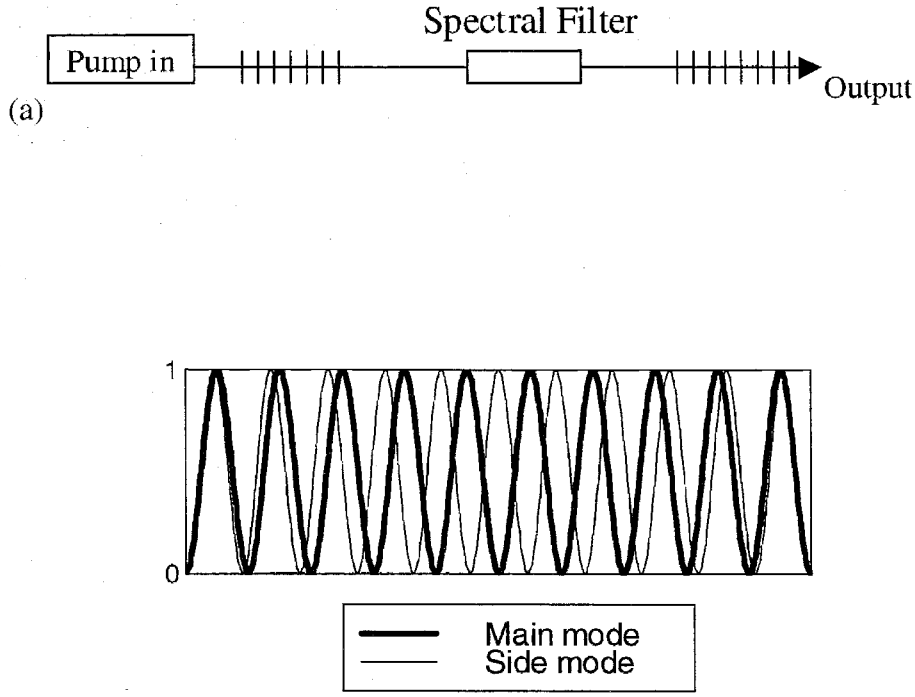

Figure 6.3. Linear long cavity fiber laser.

(a) Geometry of laser, and (b) schematic of resonant standing mode overlap.

Small cavity linear distributed feedback fiber lasers eliminate this disadvantage because only one mode satisfies the resonant condition. These lasers are being developed and commercialized [6–3], but do not have the output power and efficiency superiority, at least in principle, as a larger cavity laser.

The ring geometry of Figure 6.4 is a better use of the gain section allowing the traveling wave to completely saturate the gain material and overlap all resonant modes.

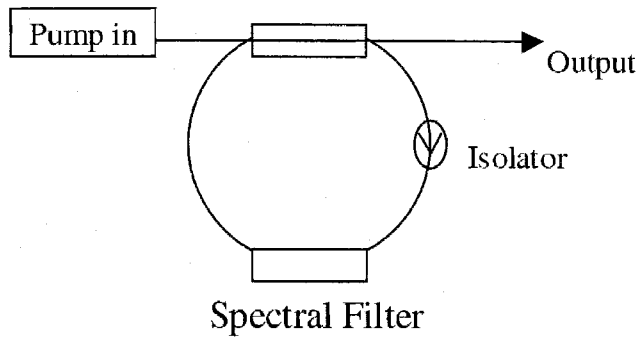

Figure 6.4. Ring laser geometry.

Spectral filtering is much easier because back reflections from the filter are eliminated by the isolator, unlike in a linear laser where they can create another cavity. The overall effect is superior side mode suppression: > 60 dB, assuming all but the main mode can be spectrally filtered.

Progress in the research of single mode fiber ring lasers has been achieved by Vahala et al. [6–4],[6–5],[6–6]. Vahala's ring laser featured two fiber coupled Fabry-Perot filters, one broadband filter (26.1 GHz) and one narrowband filter (1.39 GHz). These filters working in concert allowed only one ring mode to lase. However, with the polarization controllers and isolators needed, the ring cavity was ~15 m long, which set the ring cavity mode spacing at $\Delta\nu = \frac{c}{nL} = 14\,\mathrm{MHz}$, and a single mode stability was only achieved for "several minutes" at a time.

Another recent contribution in the field of single mode fiber ring lasers was provided by H. Inaba et al. [6–7]. Mode selection was achieved using a circulator and reflection grating. They claim that a grating as narrow at 5 GHz was needed to achieve single mode operation. Their 10 meter ring had a mode spacing of 20 MHz, putting many modes within the grating bandwidth. However, the homogenous broadening effect in the erbium saturated the gain within this bandwidth to allow only one mode to oscillate without mode hopping for 5-20 minutes. Multimode oscillation was observed with a grating of 30 GHz FWHM.

We were able to achieve robust single mode operation with mode spacing on the order of a few hundred MHz with a combination of gratings to define precisely the lasing mode and polarization. The mode spacing was extended as a result of significantly reducing the ring cavity length by eliminating polarization controllers, circulators, multiple isolators, bulky FP-coupled resonators, and by using short, highly Er^{3+} doped gain fiber. Single mode operation of a few days was observed with no mode hopping demonstrating that the ring laser we developed is a promising 1540 nm fiber laser source for the telecommunications industry. Improved temperature stabilization would be able to extend the single mode operation indefinitely. A pending patent contains this newly developed single mode filtering technology.

6.4. Output Optimization

Optimizing the output coupling of the ring laser involves analyzing the gain and intrinsic loss parameters. A simple analytical model for output coupling can be derived from the theory of gain saturation (Section 6.2). Approximating out the propagation effects, for only a few dB of gain, the equation for gain saturation, clamped at threshold is

$$\gamma_t = \frac{\gamma_0}{1+\frac{P_c}{P_{sat}}} \tag{6.6}$$

where P_c is the power in the cavity, P_{sat} is the intrinsic saturation power, and γ_0 is the parameter in the small signal gain,

$$G = e^{\gamma_0 L}. \tag{6.7}$$

The internal loss is

$$L_i = 1 - e^{-\alpha L} \tag{6.8}$$

and the lasing condition is

$$(1-T)e^{\gamma_t L}e^{-\alpha L} = 1 \tag{6.9}$$

where γ_t is the gain clamped at threshold. When combined with (6.6-6.8), the output power is

$$P_{out} = P_c T = P_{sat}\left[\frac{\ln G}{\ln\left(\frac{1}{1-T}\cdot\frac{1}{1-L_i}\right)} - 1\right]T \tag{6.10}$$

where the output coupling fraction, T, is taken as the independent parameter.

Figure 6.5 shows the optimization for three completely different laser types for different internal losses. A helium-neon laser typically has extremely low internal loss and small gain. Admittedly, there is Doppler-broadened inhomogeneous gain, but like this model shows, optimum output coupling is only a few percent. In this regime of $L_i<<1$ and $T<<1$, a reasonable approximation to (6.10) can be made using $e^{\gamma_t L} \approx 1-\gamma_t L$ to arrive at

$$P_{out} \cong P_{sat}\left[\frac{\gamma_t}{T+L_i}-1\right]T. \qquad (6.11)$$

A 1540 nm semiconductor laser typically has a huge gain per pass, but the internal losses are larger as well, pushing optimum output coupling to 30-50%. The fiber ring laser losses are intermediate between the other two types of lasers, averaging around 1dB (~20%) or less.

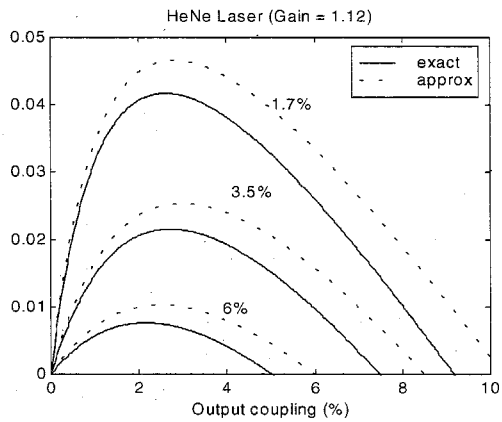

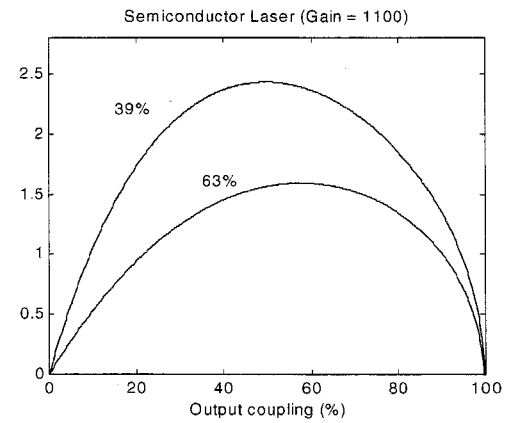

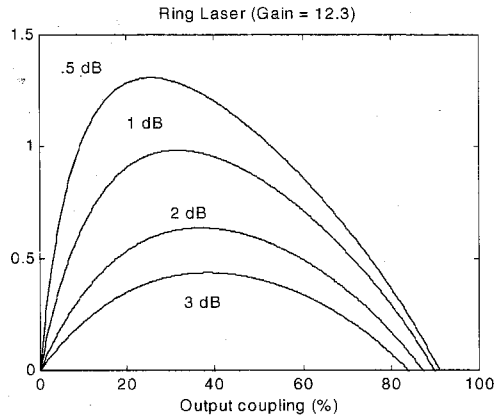

Figure 6.5. Output optimizations for three different laser types.

Parameters from a characterized section of 26 cm of erbium doped fiber was used to model the output properties of a ring laser with a projected loss of .6 dB. Shown in Figure 6.6a is the projected output vs. output coupling for various pump powers as high as 119 mW. Figure 6.6b is the modeled LI curve at 20% output coupling.

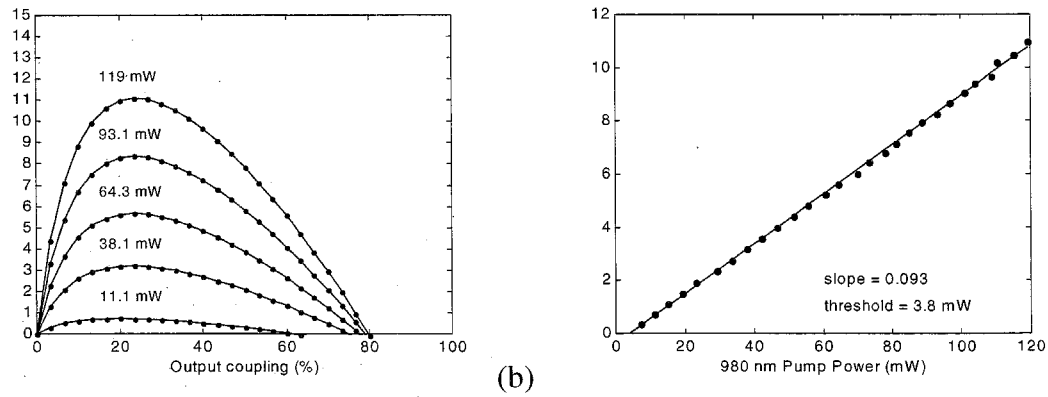

(a) (b)

Figure 6.6. Modeled output power based on gain parameter measurements.

(a) Power output for different levels of 980 nm pump power, (b) Power output vs. 980 nm pump power.

6.5. Ring Laser Characteristics

6.5.1. Optical Spectrum

Figure 6.7 compares the optical spectrum of the fiber ring laser with that of a high quality semiconductor laser. The side mode suppression ratio (SMSR) of the fiber ring laser of 70 dB is more than three orders of magnitude better than that of the semiconductor laser. (Good DFB lasers are usually specified at >35 dB SMSR.)

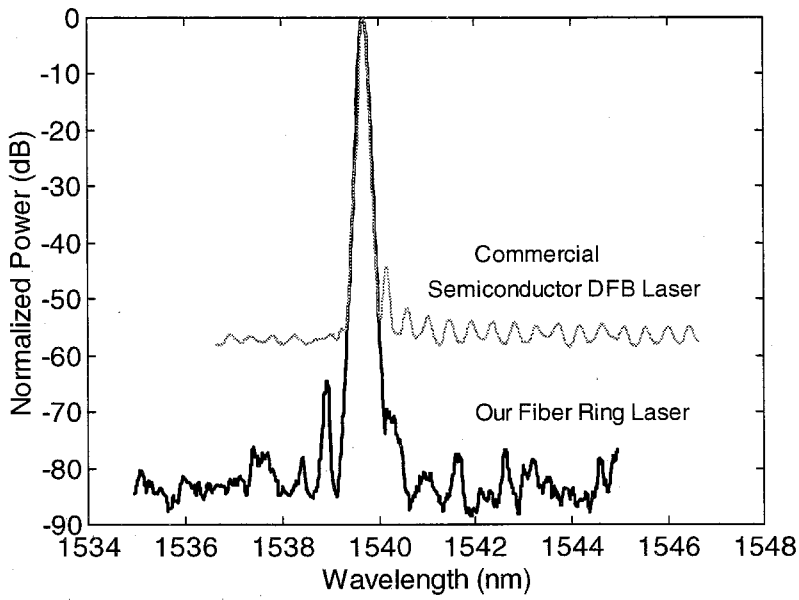

Figure 6.7. Optical Spectra of FRL and SCL.

The high SMSR is mainly due to the ring architecture and the outstanding mode selection of the ring laser. In the figure, each spectrum is normalized to its peak power at 0dB. The

resolution bandwidth for the optical spectrum analyzer is .08 nm which effectively broadens the lasing peak and sidemodes seen in the plots. The side mode on the low wavelength side of the ring laser spectrum can be completely suppressed in future generations of the laser.

In an SCL under multi-mode operation, each individual mode can have large intensity noise (mode partition noise). However, because of anti-correlation between the modes, the extra noise does not show up in the total intensity noise. Therefore, in an SCL with weak side modes, even at 35 dB weaker than the main mode, the main mode AM noise is over an order of magnitude higher than the shot noise. This excess noise manifests during propagation in a dispersive fiber (Chapter 3), due to the loss of the anti-correlation with the side modes and also after filtering the main mode in a WDM system with a drop filter.

6.5.2. Power and Wavelength Stability

In order to avoid crosstalk between the channels a DWDM system requires a multiple number of transmitters that operate at known fixed light frequencies (ITU grid) with a tolerance of a few gigahertz. The frequency stability of the SCL is adversely affected by temperature (12 GHz/^{0}C) and bias current (1 GHz/mA). The SCL laser operating conditions have to be set precisely in order to match the ITU grid frequency. Due to the aging of the thermistor and also a drift in the operating conditions of the SCL laser in time, a long-term frequency mismatch can develop. This can only be solved with the

integration of a frequency locker into the laser package or by using an external frequency locker.

The fiber ring laser has a built-in frequency locking mechanism with better than 0.1 GHz/^{0}C frequency stability, which is more than an order of magnitude better than that of the SCL. The fiber laser frequency is also much less sensitive to pump power than the semiconductor laser (injection current). The ring laser stays virtually at the ITU frequency starting from threshold. This also eliminates the need for an ultra-low noise and precision current source for each channel.

An unpackaged fiber laser was monitored for 10 hours operating very close to the ITU frequency 195300 GHz and within the ±5GHz allowed by the Bellcore standard (Figure 6.8). When properly packaged and temperature controlled, this laser should not mode hope at all. In the case of such rare event, however, the laser frequency will deviate from the ITU frequency by less than 0.4 GHz.

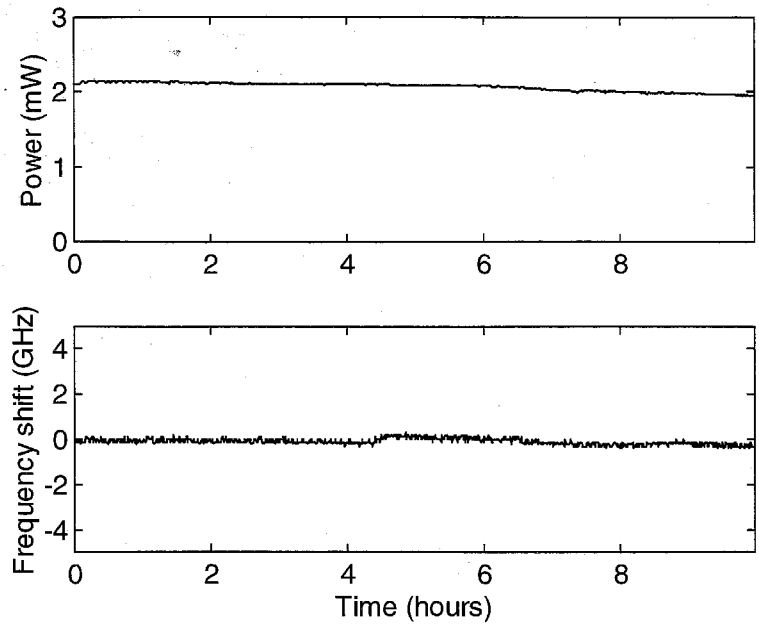

Figure 6.8. Fiber ring laser power and frequency stability.

6.5.3. Temperature Dependence

By cycling the temperature of the substrate containing the fiber ring laser and monitoring the lasing frequency, it was possible to probe the temperature dependence of the laser. Shown in Figure 6.9 are several sets of data as the laser was cycled between 19° and 26°C. This plot clearly shows repeatable single mode operation of this laser between 23° and 26°C. A temperature dependence of -3 GHz/°C was found, which is larger than the intrinsic fiber Bragg grating dependence of -1 GHz/°C. This was determined to be due to the thermal expansion of the substrate on which the grating was glued and can be compensated by a suitable material choice, e.g., the glass ceramic of Section 5.1.1.

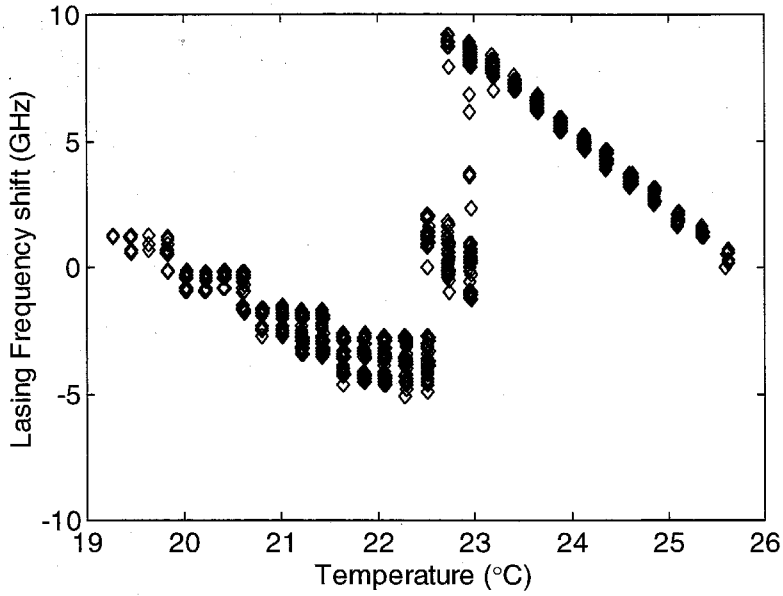

Figure 6.9. Lasing frequency vs. temperature.

6.5.4. RIN and Fiber Propagation

In Chapter 3, an expression for the Relative Intensity Noise (RIN) was derived and the noise was measured in a DFB semiconductor laser. The fiber ring laser has a shot noise limited AM noise performance. In principle, the SCL AM noise should also be close to the shot noise at high pump rates. However, due to the presence of side modes the Relative Intensity Noise (RIN) exceeds the shot noise limit unless the SMSR is better than 40-50 dB. Figure 6.10 shows the RIN for a DFB semiconductor and fiber ring laser. Output power for the SCL was about 20 mW and that of the fiber ring laser was about 2.5 mW.

Larger photocurrent brings larger noise, making it possible to measure lower values of RIN. The fiber laser relaxation resonance is well below 1 GHz, explaining the flat RIN spectrum on the scale shown.

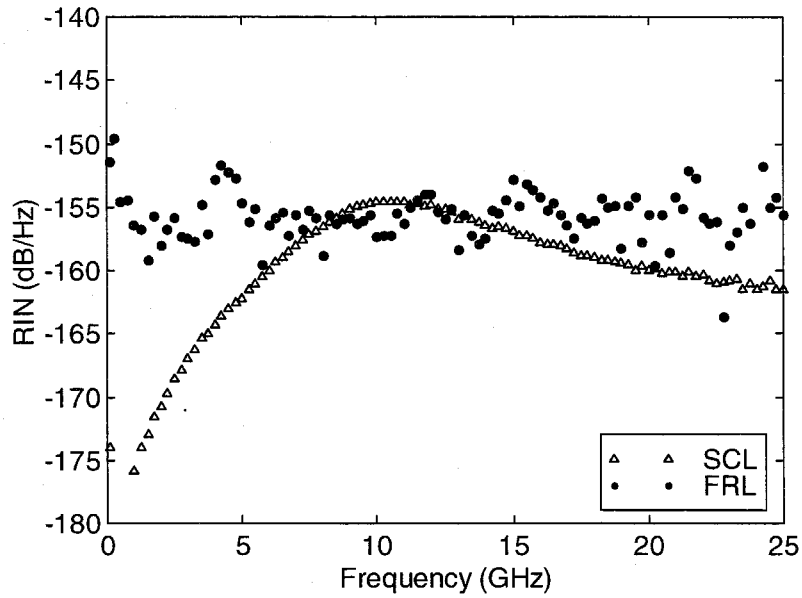

Figure 6.10. The RIN of a SCL and fiber laser.

Even with a typical 35 dB SMSR ratio and after propagation the AM noise performance of a SCL will deteriorate even further due to the loss of the nearly perfect anti-correlation between the main mode noise and the side mode noise. This can be especially important for analog low frequency modulation in cable TV systems.

The AM noise of the SCL also suffers from FM to AM noise conversion after propagation which is virtually absent in the fiber laser. The SCL RIN at low frequency is increased dramatically after propagating in a long fiber cable (25 km) at high input

powers due to Stimulated Brillouin Scattering SBS (Figure 6.11), also evidenced by the spike at 11 GHz, and also sidemode decorrelation. SBS will also limit the transmitted power of the fiber ring laser, but the noise generated will be negligible due to the very low FM noise of the ring laser (next section). This can allow higher power transmission over longer distances of optical fiber. The high frequency dip of the SCL is due to the interplay of the AM-to-FM noise conversion. At those frequencies, the large FM noise is converted to AM noise and destructively interferes with the original AM noise, hence lowering the RIN.

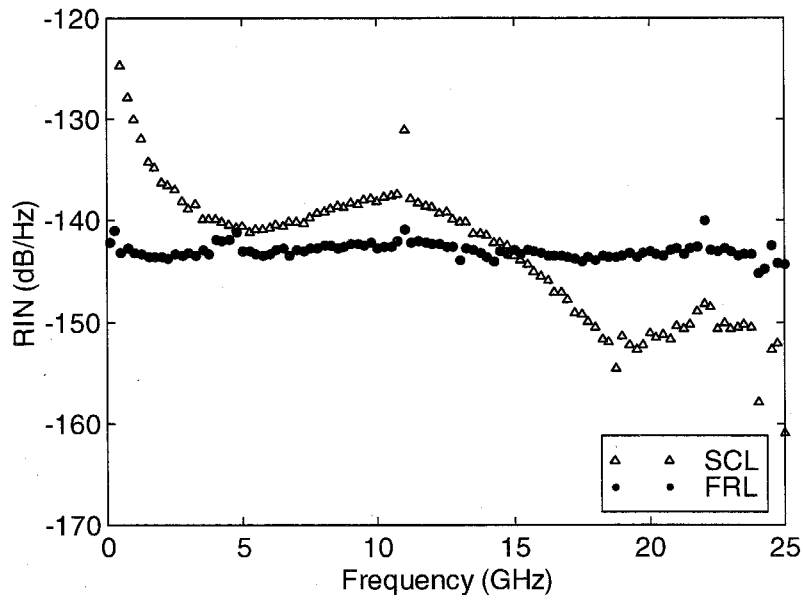

Figure 6.11. RIN of SCL and FRL after 25 km and filtered by a 2 nm FP filter.

6.5.5. FM Noise

Laser linewidth is an important characteristic in high speed communications when considering propagation in dispersive optical fiber. FM-to-AM conversion corrupts optical signals with a large FM noise component.

The FM noise spectrum for a laser is described by random phase fluctuations that broaden the spectral line.

$$E(t) = E_0 e^{i[\omega t + \phi(t)]} \tag{6.12}$$

Well derived are the contributions to laser linewidth [6–8]. The field power spectrum is given by [6–9] as

$$S_E(\omega) = \int_{-\infty}^{\infty} \exp\left[-\frac{1}{\pi}\int_{-\infty}^{\infty} \sin^2\left(\frac{\Omega\tau}{2}\right) S_{\dot{\phi}}(\Omega)\frac{d\Omega}{\Omega^2}\right] e^{i(\omega-\omega_m)\tau} d\tau \tag{6.13}$$

where ω_m is the lasing frequency and the two-sided noise frequency is

$$S_{\dot{\phi}}(\Omega) = S_0 + \frac{S_1}{\Omega} \tag{6.14}$$

which is measured in $(rad/s)^2/Hz$. Spontaneous emission into the lasing mode adds a white noise contribution, S_0, to the phase noise, and 1/f noise adds the term $\frac{S_1}{\Omega}$. Equation (6.14) allows the two contributions to factor in the exponential of (6.13), and the field spectrum can be treated as a convolution of the two noise contributions, treated in depth by Mercer [6–10]. The white noise contribution to the linewidth results in a Lorentzian power spectrum of frequency fluctuations, and Mercer shows that the 1/f contribution can

be approximated near the peak of the spectrum by a gaussian curve. The convolution is known as the Voigt profile, equal to the real part of the error function:

$$V(f) = \int_{-\infty}^{\infty} \frac{1}{(f'-f)^2 - \Delta f_L^2} e^{\frac{2f^2}{\Delta f_G}} df' \qquad (6.15)$$

Optimized computational approximation methods exist [6–11] and were implemented; however, numerically evaluating the integral to extract the useful linewidths, Δf_L and Δf_G worked equally well for our application.

The linewidth of the ring laser was measured by the delayed self-heterodyne scheme shown in Figure 6.12, so called because the laser light modulated, split into two paths, one delayed longer than the coherence length, and recombined at a detector.

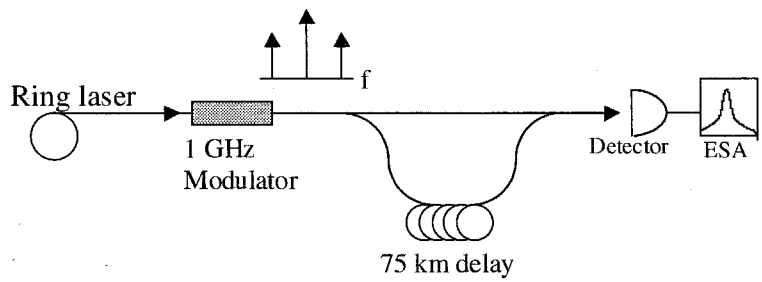

Figure 6.12. Experimental set up for the self-heterodyne linewidth measurement.

The spectrum at the modulation frequency is a self-convolution of the lineshape of the laser. An amplitude modulator was used to provide the modulation signal, 1 GHz, chosen to move the center frequency out of any radio frequency interference. A 75 km spool of fiber was needed to get the resolution of the measured lineshape into the sub-kHz regime.

The measured spectrum is shown in Figure 6.13. The very narrow spike at the center of the peak is the coherent beating of the 1 GHz signal with sidebands of the carrier along a single path of fiber. The fitted parameters for the laser are

$$\begin{aligned} &\text{Lorenztian FWHM } \Delta\nu_L = 2\,\text{kHz} \\ &\text{Gaussian FWHM } \Delta\nu_G = 80\,\text{kHz} \end{aligned} \tag{6.16}$$

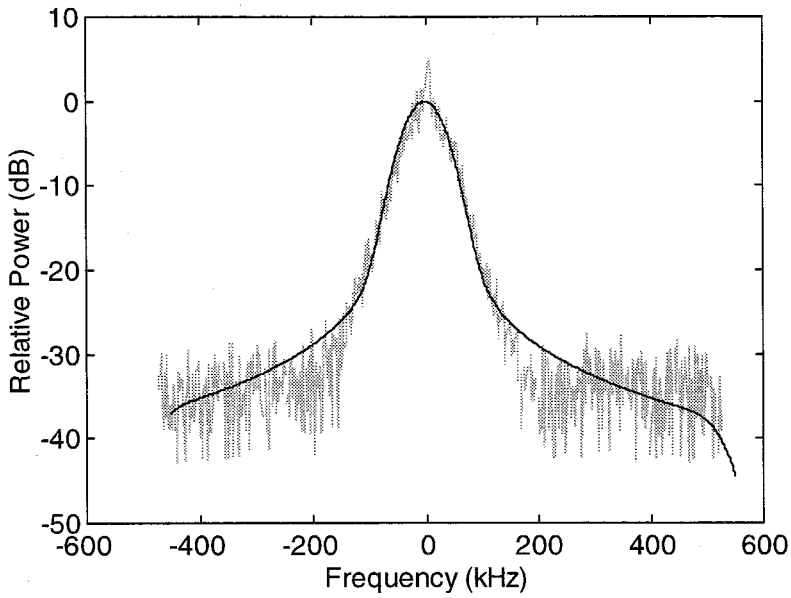

Figure 6.13. Delayed self-heterodyne measurement of laser linewidth. Gray trace is measured data; black trace is a fitted Voigt curve.

It is possible to measure such a narrow linewidth with 75 km of delay because there is very little laser RIN (Relative Intensity Noise) to be converted to FM noise by dispersion in the fiber. The typical semiconductor linewidth is on the order of a few MHz. It is much larger than the ring laser due to the small cavity size and amplitude-to-phase

coupling (the α parameter). Note the three orders of magnitude difference in measured linewidths for the two types of lasers (Figure 6.14).

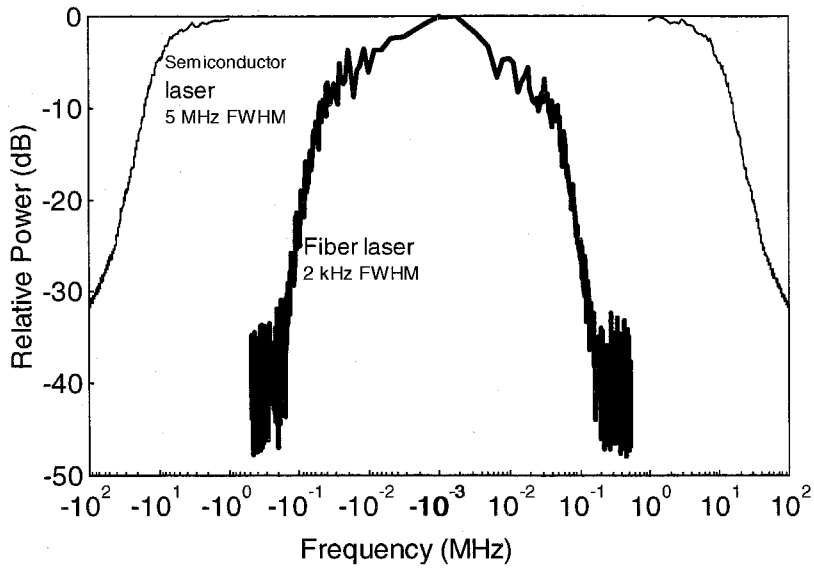

Figure 6.14. A comparison between a SCL and the fiber laser FM noise.

High FM noise can be a significant problem during propagation in a dispersive fiber due to FM-to-AM noise conversion. It can also contribute to the noise in a DWDM network due to the dispersion caused by the tail of many drop filters. The amplitude-to-phase noise coupling of an SCL can be exploited to partially offset this problem. However, it requires a careful design of the laser as well as the network parameters such as filter dispersion and fiber length. The low noise of the fiber ring laser poses none of these problems.

6.6. Bit Error Rate (BER) Measurement

This demonstration is a measure of the true data-sending performance of an optical communication system. A pseudorandom bit stream was transferred onto an optical network, propagated in 50 kilometers of optical fiber, and then detected and checked for errors. The requirements for most communications systems is an error rate less than 10^{-10}, or 1 error in 10^{10} bits. In order to accurately measure these rates, it takes hours to perform this experiment. System performance can still be measured accurately by using a variable attenuator before the detector and measuring the BER as a function of received optical power.

Figure 6.15 shows the experimental setup and equipment used. A source laser is set to output a constant wavelength and power. A fiber isolator is used to keep any reflected signals from being fed back into the laser which would cause instabilities. A pseudorandom digital bit stream is generated and fed to an electro-optic modulator (EOM) which transfers the electronic digital signal to the optical fiber. The optical signal is then amplified with an erbium-doped fiber amplifier (EDFA), propagated in a spool of 50 km of single mode fiber, reamplified, filtered, and passed through a variable attenuator, controlled by the user. A 90/10 splitter is used to tap off some light and the average received power is monitored with an optical spectrum analyzer (OSA). The high-speed detector converts the optical signal into an electronic signal and sends it back to the Signal Generator and Error Analyzer where it is compared with the original signal.

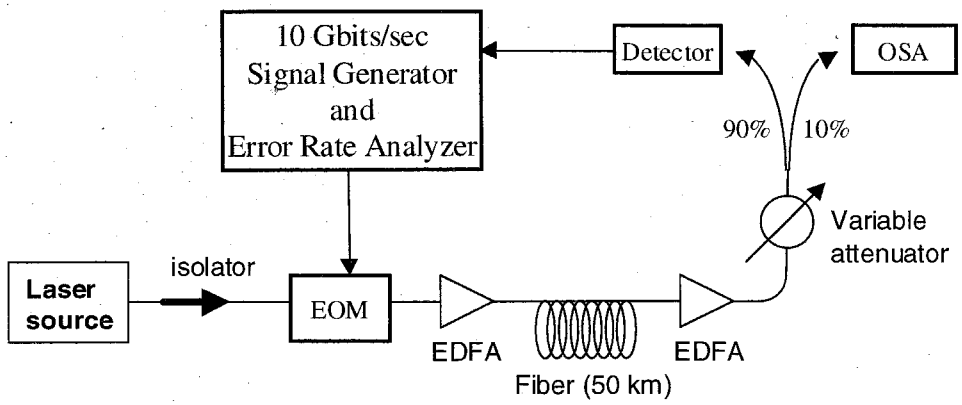

Figure 6.15. The Bit error rate measurement apparatus.

Two types of data are obtained with a BER measurement. One is an eye diagram plot, which shows points taken from a sampled version of the data. This plot graphically displays the 0's and 1's from the data and shows how efficiently the system can convert between them. Nice, wide open "eyes" where no dots appear in the eye opening show good signal recovery, but no accurate quantitative data is obtained. Figure 6.16 shows a very good " open eye" diagram of the ring laser.

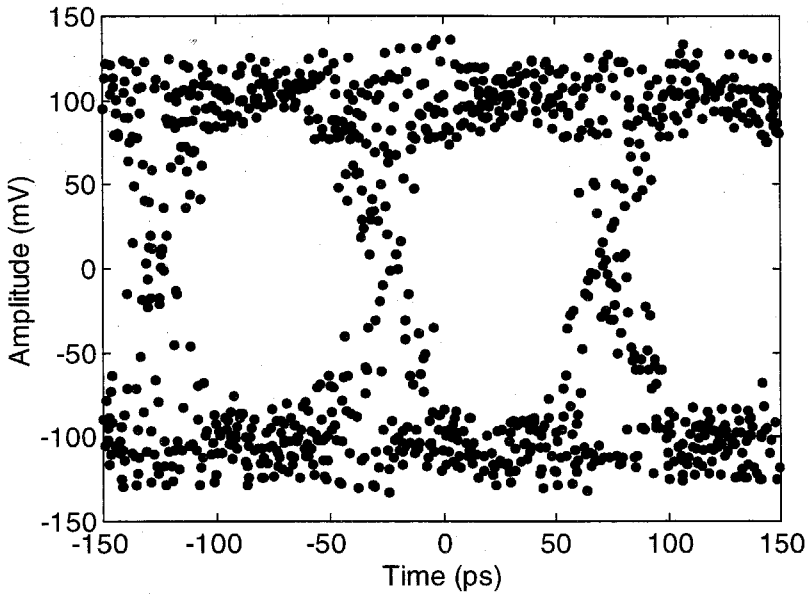

Figure 6.16. The "Eye" diagram of the ring laser.

In the second type of data, BER vs. received power, the received optical power is plotted in dBm, and the BER is plotted showing the exponent of the BER on a logarithmic scale. On this plot, a straight line is fit to the data and the power necessary to receive lower error rates can be inferred from the fitted line. Figure 6.17 shows the BER data for the fiber ring laser under various conditions.

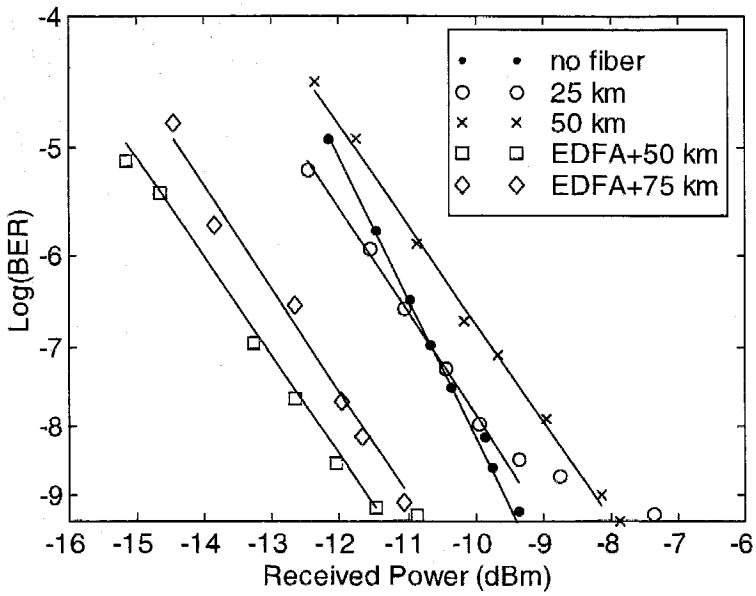

Figure 6.17. BER data for the fiber ring laser for different fiber lengths.

In comparing the two laser types, the BER plot of the semiconductor laser (SCL) and the fiber ring laser (FRL) after 50 km of fiber propagation, the SCL needs nearly 3 dB more power to achieve the same error rate (Figure 6.18). This is referred to as a "power penalty" of 3 dB, made possible by the fundamental advantages in noise characteristics of the FRL. This communication performance advantage of the FRL can be translated into longer distances between amplifiers in a long-haul network. For every 50 km that a SCL signal is propagated, a FRL signal can be sent 70 km and still have the same system performance.

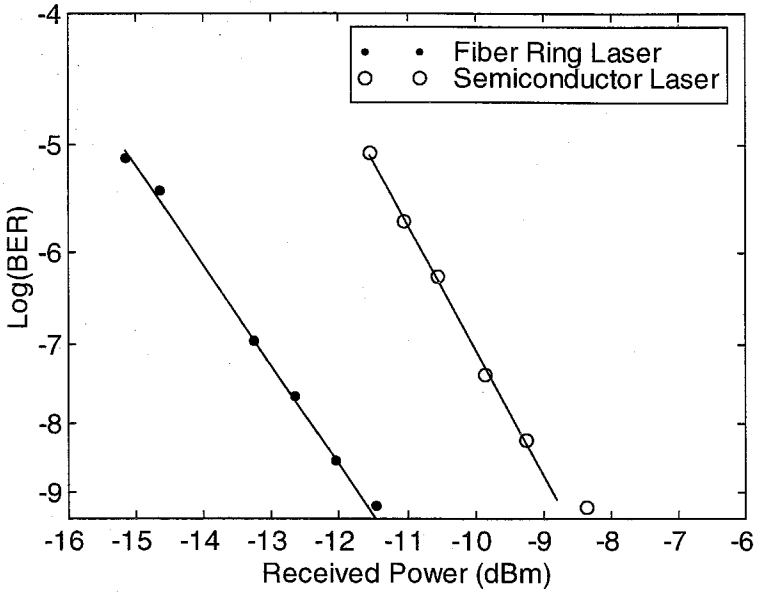

Figure 6.18. BER after 50 km of fiber for the FRL and SCL.

For fiber lengths a few 10's of kilometers, the measurement below 10^{-10} was difficult due to random delay fluctuations in the fiber spool. Without separate clock recovery, it is impossible to keep the receiver data aligned with the original data for more than a few seconds.

6.7. Fiber Lasers in Communication Systems

The fiber ring lasers developed here are an extremely practical application of fiber Bragg gratings and erbium doped fiber. For such a relatively large-cavity single mode laser,

these fiber ring lasers have several advantages over semiconductor lasers for long-haul DWDM systems.

The most important advantage of the SCL is its ability for internal modulation. However, the highest practical modulation frequency is limited by the relaxation resonance frequency to less than 20 GHz. Moreover, the associated frequency chirp calls for external modulation in many applications. In 10 Gbits/s systems, if frequency chirp is an important factor and an external modulator is needed, the ring laser can be a cost-effective solution. This is also true for analog modulation for cable if better linearity and lower noise are required. In 40 Gbits/s systems, external modulation is a necessity, putting the fiber ring laser on equal footing with the SCL. Once the full number of ITU channels are utilized, 40 GBits/s modulation will become more prevalent in future networks, since the only venue for increasing the network capacity will be using higher modulation speed.

Fiber ring lasers are made of passive components. They are therefore more reliable and not prone to catastrophic failure or change in its operating conditions. Moreover, only one semiconductor laser is needed to pump possibly eight ring lasers, and the requirements on pump laser light are much less than on communication wavelengths, making them much cheaper to fabricate than 1540 nm SCL lasers. Thus, current, temperature, and external locking electronics associated with each SCL based DWDM channel are eliminated.

The following table summarizes the properties of the fiber ring laser and a typical 1540 nm communication grade semiconductor laser.

Semiconductor DFB Laser	**Fiber Ring Laser**
• 40 dB side mode suppression.	• >70 dB side mode suppression.
• Shot noise limited AM noise (contingent on correlated mode partition noise).	• Shot noise limited AM noise.
• 5 MHz linewidth.	• 2 kHz linewidth.
• 12 GHz/°C Frequency stability.	• 0.02 GHz/ °C Frequency stability.
• 1 GHz/mA frequency stability.	• Frequency nearly independent of power.
• Not immune to EM noise.	• Immune to EM noise (diode pumped).
• Very sensitive active device.	• Highly reliable passive components.
• Power supply for each laser.	• 1 Power supply for 8 lasers.
• Can be internally modulated up to 10 Gbits/s.	• Needs an external modulator.

Figure 6.19. Table comparing semiconductor lasers to fiber ring lasers.

In conclusion, the FRL represents some technological advances in terms of stable, single mode operation for a 1 meter cavity. The FRL's technical performance, in conjunction with low cost and ease of production, could make it an important contender in the DWDM transmitter market.

References for Chapter 6

[6–1] Desurvire, *Erbium Doped Fiber Amplifiers.*

[6–2] A. A. M. Saleh, R. M. Jopson, J. D. Evankow, and J. Aspell, "Modeling of gain in Erbium-doped fiber amplifiers," IEEE Phot. Tech. Lett., 2 (10), pp. 714-716 (1990).

[6–3] W. H. Loh, B. N. Samson, L. Dong, G. J. Cowle, and K. Hsu, "High performance single frequency fiber grating-based erbium:Ytterbium-codoped fiber lasers," J. Lightwave Tech. 16, (1), pp. 114-118 (1998).

[6–4] Namkyoo Park, Jay W. Dawson, and Kerry J. Vahala, "All fiber, low threshold, widely tunable single-frequency, erbium-doped fiber ring laser with a tandem fiber Fabry-Perot filter," Appl. Phys. Lett, 59, (19), pp. 2369-2371 (1991).

[6–5] Steve Sanders, Namkyoo Park, Jay W. Dawson, and Kerry J. Vahala, "Reduction of the intensity noise from an erbium-doped fiber laser to the standard quantum limit by intracavity spectral filtering," Appl. Phys. Lett, 61, (16), pp. 1889-1891 (1992).

[6–6] Namkyoo Park, Jay W. Dawson, and Kerry J. Vahala, "Frequency locking of an erbium-doped fiber ring laser to an external fiber Fabry-Perot resonator," Optics. Lett, 18, (11), pp. 879-881 (1993).

[6–7] Hajime Inaba and Yoshiaki Akimoto, "A single-frequency and single-polarization fiber ring laser using a 5-GHz fiber Bragg grating," Elect. and Comm. in Japan, Part 2, 82 (5), pp. 21-29 (1999).

[6–8] Charles H. Henry, "Phase noise in semiconductor lasers," J. Lightwave Tech. 4, (3), pp. 298-311 (1986).

[6–9] H. E. Rowe, *Signals and Noise in Communication Systems,* D. van Nostrand, Princeton, 1965.

[6–10] Linden B. Mercer, "1/f frequency noise effects on self-heterodyne linewidth measurements," J. Lightwave Tech. 9 (4), pp. 485-493 (1991).

[6–11] J. Humlicek, "Optimized computation of the Voigt and complex probability functions," J. Quant. Spectrosc. Radiat. Transfer, 27 (4), pp. 437-444 (1982).